MAGNETIC DIPOLE MOMENT OF THE SHORT-LIVED RADIOISOTOPE ^{55}Ni MEASURED BY BETA-NMR SPECTROSCOPY

By

Jill Susan Berryman

A DISSERTATION

Submitted to
Michigan State University
in partial fulfillment of the requirements
for the degree of

DOCTOR OF PHILOSOPHY

Chemistry

2009

ABSTRACT

MAGNETIC DIPOLE MOMENT OF THE SHORT-LIVED RADIOISOTOPE ^{55}Ni MEASURED BY BETA-NMR SPECTROSCOPY

By

Jill Susan Berryman

The double shell closure at $N = Z = 28$ in ^{56}Ni has been investigated through the measurement of the magnetic moment of a nucleus one neutron removed from this core. Nuclear moments are fundamental, measurable properties that provide information on the structure of nuclei. The magnetic moments of doubly closed nuclei $\pm$ 1 nucleon are of particular importance, since the properties of each of these nuclei are determined by the orbit occupied by that last nucleon. Any deviation from theory indicates the presence of higher order effects such as configuration mixing, meson exchange currents, isobar excitation, and/or even a breakdown of the shell closure.

The ^{56}Ni core has been shown to be soft, attributed to the strong proton-neutron interaction, in comparison to the ^{48}Ca core. The small magnetic dipole moment of ^{57}Cu, with $T_z = -1/2$ and residing one proton outside ^{56}Ni, suggests the double shell closure at proton and neutron numbers 28 is broken. However, the experimental ground state magnetic moments of the $T_z = +1/2$ nuclides ^{57}Ni and ^{55}Co agree well with shell model predictions, albeit with a "soft" ^{56}Ni core. The ground state magnetic moment of ^{55}Ni, also with $T_z = -1/2$ but with one neutron removed from the ^{56}Ni core can provide critical insight on the nature of the ^{56}Ni core, and can be a basis to understand how the structure of doubly-magic nuclei may change away from stability.

The nuclear magnetic moment of the ground state of ^{55}Ni ($I^\pi = 3/2^-, T_{1/2} = 204$ ms) has been deduced in this work to be $|\mu(^{55}\text{Ni})| = (0.976 \pm 0.026)\ \mu_N$ using the β-NMR technique. A polarized beam of ^{55}Ni was produced by fragmentation of a

^{58}Ni primary beam at energy 160 MeV/nucleon in a Be target. The A1900 and RF Fragment separators were used to eliminate all other beam contaminants. Results of a shell model calculation using the GXPF1 interaction in the full *fp* shell model space was found to reproduce the experimental value and support a softness of the ^{56}Ni core.

Together with the known magnetic moment of the mirror partner ^{55}Co, the isoscalar spin expectation value $\langle \sum \sigma_z \rangle = 0.91 \pm 0.07$ shows a similar trend to that established in the *sd* shell. Effective g factors for the $A = 28$ system obtained from a fit to isoscalar magnetic moments, isovector moments, and M1 decay matrix elements were applied to matrix elements for $A = 55$ calculated with the GXPF1 interaction to obtain $\langle \sum \sigma_z \rangle$ for $A = 55$. The results of the calculation show the best agreement with the experimental value for both μ and $\langle \sum \sigma_z \rangle$ and imply that a universal operator can be applied to both the *sd* and *fp* shells.

for eric

ACKNOWLEDGMENTS

First and foremost, I would like to thank my advisor, Paul Mantica, for all he has done for me on this long trek known as graduate school. Paul, your wisdom amazes me and I would not be in this position without your guidance. Thank you for always keeping the big picture in mind and reminding me to do the same. Thank you for making me a better scientific writer and speaker. Thanks for giving me the opportunity to travel all over the world. Thank you for the group bonding time over lunches, dinners, parties at your house, and picnics at your cottage (thanks to Stacy for those as well!). I will never forget some of your favorite phrases including: "Graduate school is a stepping stone, not a career," and "You have to love what you do," (in response to my persistent question on how to be successful).

Another person that deserves recognition is physicist Kei Minamisono. Kei knows just about everything there is to know about β-NMR and was always willing to answer questions, lend a hand in the lab, and discuss my work. Thank you, Kei! I would like to thank the rest of the beta group members that overlapped with me: Andrew, Josh, and Heather. Andrew, we did not overlap for long, but I will never forget your kind and helpful emails before I even arrived at MSU, and your encouraging words during my first year as a graduate student. Josh, for all four of my years here I looked up to you for help on everything from my first committee meeting to my second year oral exam to writing this dissertation. Thanks for doing everything first and then being willing to tell me what to do and what not to do! Heather, thanks for being a great friend, travel buddy, and someone that I could always bounce an idea off. You always helped me look to the positive side of things!

I would like to thank my committee members including David Morrissey, Michael Thoennessen, and Remco Zegers. Thank you for your guidance and for making me a better scientist. Thanks to collaborator Warren Rogers who proposed the ^{55}Ni

experiment the first time around and for his help during the experiment. Thank you Alex Brown and Ian Towner for your helpful theory discussions after the measurement was complete. Thanks to Andrew Stuchbery for insight on the polarization simulation, especially the gamma-ray deorientation calculations. I would also like to acknowledge Michigan State University, the Department of Chemistry, NSCL, and the National Science Foundation Graduate Research Fellowship program for financial support.

There are many people at NSCL that made my thesis experiment a success. I have greatly appreciated the friendly attitude of all the staff. Everyone is more than willing to talk with you, answer questions, and help in any way they can. Al Zeller was always willing to answer my magnet questions. Thanks to John Yurkon for his discussions on magnetic shielding and for letting me borrow all kinds of mu metal. Thanks to Craig Snow for helping me with the mechanical design of my equipment. Thanks to Jim Wagner for making sure I had everything I needed in the S2 vault, including the new platform! Brad Powell, thanks for putting in the water lines for our dipole magnet, in both the South High Bay and then the S2 vault. A lot of credit goes to the operations department for making sure my experiment ran smoothly. Special thanks to the A1900 group, including Tom Ginter, Thomas Baumann, and Marc Hausmann. I know that my experiment required A LOT of settings and I thank you for your patience and hard work! Thanks to those special operators who gave me great beam and ordered Big Ten Burrito during the midnight shifts: Carl Cormany and Dave Schaub. Daniel Bazin deserves many thanks for his willingness to tune the Radiofrequency Fragment Separator anytime day or night, and the great job that he did! Thanks to Geoff Grinyer for helping with the experiment and for the helpful discussions afterward.

I have grown close to a number of people here that I will dearly miss. Thanks for the great times on DALMAC, guys and gal (Jon Babbage, Thomas Baumann, Jon Bonofiglio, Renan Fontus, Cindy Fontus, Doug Miller, Dave Miller, Dave Sanderson, Mathias Steiner, Chisom Wilson, John Yurkon, Andrew Ratkiewicz, and Phil Voss).

What a great ride with a great group of people! Jon Bonofiglio, thanks for getting up at 5:30 AM for spinning class two days a week and for swimming on Fridays! Thanks to my other spinning friends who I have grown close to during the wee hours of the morning: Tom Mitchell (the greatest spinning instructor ever), Sarah AcMoody, and Robin Usborne. Phil Voss, I must thank you for organizing Happy Hour every Friday, and for being a great softball coach! Thanks to Rhiannon Meharchand, Krista Cruse, Michelle Mosby, and Heather Crawford for the girly outings and for throwing me my only wedding shower!

Special thanks to my family, including ALL the Pinters and Berrymans. My mom and dad have always been the most supportive parents a girl could have. Without you, I would not have been able to do a lot of things. Dad, thanks for making me work hard my whole life at the greenhouse. Hard work comes naturally now because of you. Thanks for teaching me I could do anything the boys could do (and more), including fix heaters, put in sprinkler systems, drive tractors and dump trucks, pour cement, and haul flats. Mom, thanks for instilling the importance of education into all your kids. I will never forget how you made us do those math workbooks in the summer which I hated, but now I guess I thank you for it. Thanks for never restricting and always encouraging my reading list, no matter how strange the topic of the book. The overwhelming support that you have both always given means more than you know.

Four years ago if someone had told me that I would get married during graduate school, I would have thought they were nuts. Marriage was not in the plans during graduate school or ever! Now, I cannot imagine life without him. Eric, I never could have gotten through these four years without your constant love and support. I never thought I would find someone that completes me the way you do. As I write this we have been together for 3.75 years, married for eight months, and I am giddy over the fact that we get to spend the rest of our lives together. I love you more and more everyday.

Contents

List of Tables

List of Figures

Chapter 1

Introduction

The nuclear magnetic dipole moment (μ) is a fundamental property of the nucleus that can provide detailed information on nuclear structure. Every nucleus with an odd number of protons and/or neutrons, by virtue of spin, has a magnetic dipole moment. The magnetic dipole moment arises from the electromagnetic interaction, which is well understood. The magnetic dipole operator $\vec{\mu}$ is a one-body operator and the magnetic dipole moment is the expectation value of μ_z. Experimental magnetic moments can be directly compared to predictions of nuclear models, and provide a stringent test of these models. Deviation of experimental values from model predictions might indicate the presence of configuration mixing among other orbits, or the need for different or better parametrized residual interactions. The sensitivity of μ to the orbital and spin components of the nuclear wavefunction yields key information on shell evolution and shell closures (magicity).

In the extreme single-particle model, the properties of a nucleus with one proton (or neutron) outside a closed shell are determined solely by the properties of the orbit occupied by the last odd nucleon. Thus, the magnetic dipole moments of nuclei near closed shells are particularly important. The simple structure can give critical insight into the shell structure, and provide a better understanding of how shell closures may change for nuclei away from the valley of stability.

The magnetic dipole moment, in addition to the other multipole moments, can be calculated with an expansion of the electromagnetic Hamiltonian. The electromagnetic interaction is well understood and an analytical form of the Hamiltonian exists. The more poorly understood strong nuclear interaction can be probed via the electromagnetic interaction by studying the multipole moments. Such analysis has the advantage that electromagnetic fields can be thought of as arising from the motion of the nucleons under the influence of the strong force, and this measurement does not distort the object of interest.

1.1 Electromagnetic Interaction

The external effects of any distribution of charges and currents (e.g., a nucleus) vary with distance in a characteristic fashion. An electromagnetic multipole moment associated with each characteristic spatial dependence is assigned to the charge and current distribution. For example, the $1/r^2$ electric field arises from the net charge, which is assigned as the zeroth or monopole moment. The $1/r^3$ electric field arises from the first or dipole moment, the $1/r^4$ electric field arises from the second or quadrupole moment, and so forth. The magnetic multipole moments behave similarly. The electric and magnetic multipole moments can be calculated in the nuclear regime by treating the multipole moments in operator form and calculating their expectation values for various nuclear states. These predictions can then be directly compared with the experimental values measured in the laboratory.

1.1.1 Electric multipole expansion

A systematic expansion for the electric potential of an arbitrary localized charge distribution, ρ, has been developed by Griffiths [1]. Figure 1.1 defines the appropriate geometric variables. The potential at point P, some distance $\vec{r}$ from the origin, from some object with a charge density distribution $\rho(\vec{r}')$ that is distance $\vec{r}'$ from the

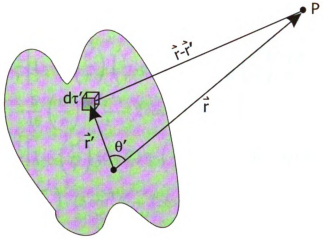

Figure 1.1: Definition of geometric variables used in electric multipole expansion.

origin, is given by the expression

$$V(\vec{r}) = \frac{1}{4\pi\epsilon_0} \int \frac{1}{\vec{r} - \vec{r}'} \rho(\vec{r}') d\tau'. \tag{1.1}$$

Using the law of cosines,

$$(\vec{r} - \vec{r}')^2 = r^2 + (r')^2 - 2rr' \cos\theta = r^2 \left[1 + \left(\frac{r'}{r} \right)^2 - 2 \left(\frac{r'}{r} \right) \cos\theta' \right], \tag{1.2}$$

or

$$\vec{r} - \vec{r}' = r\sqrt{1+\epsilon} \tag{1.3}$$

where

$$\epsilon \equiv \left(\frac{r'}{r} \right) \left(\frac{r'}{r} - 2\cos\theta' \right). \tag{1.4}$$

Note that ϵ is much less than 1 for points well outside the charge distribution, and the reciprocal of Eq. 1.3 can be written as a binomial expansion:

$$\frac{1}{\vec{r} - \vec{r}'} = \frac{1}{r}(1+\epsilon)^{-1/2} = \frac{1}{r} \left(1 - \frac{1}{2}\epsilon + \frac{3}{8}\epsilon^2 - \frac{5}{16}\epsilon^3 + \cdots \right), \tag{1.5}$$

or, in terms of r, r', and θ':

$$\begin{aligned}\frac{1}{\vec{r}-\vec{r}'} &= \frac{1}{r}\left[1-\frac{1}{2}\left(\frac{r'}{r}\right)\left(\frac{r'}{r}-2\cos\theta'\right)+\frac{3}{8}\left(\frac{r'}{r}\right)^2\left(\frac{r'}{r}-2\cos\theta'\right)^2\right. \\ &\quad \left.-\frac{5}{16}\left(\frac{r'}{r}\right)^3\left(\frac{r'}{r}-2\cos\theta'\right)^3+\cdots\right] \\ &= \frac{1}{r}\left[1+\left(\frac{r'}{r}\right)(\cos\theta')+\left(\frac{r'}{r}\right)^2(3\cos^2\theta'-1)/2\right. \\ &\quad \left.+\left(\frac{r'}{r}\right)^3(5\cos^3\theta'-3\cos\theta')/2+\cdots\right]. \end{aligned} \tag{1.6}$$

After like powers of (r'/r) are collected in Eq. 1.6, the resulting coefficients can be seen to be the Legendre polynomials, $P_n(\cos\theta)$. Thus Eq. 1.6 can be written as:

$$\frac{1}{\vec{r}-\vec{r}'}=\frac{1}{r}\sum_{n=0}^{\infty}\left(\frac{r'}{r}\right)^n P_n(\cos\theta'), \tag{1.7}$$

where θ' is the angle between $\vec{r}$ and $\vec{r}'$. Substituting back into Eq. 1.1,

$$V(\vec{r})=\frac{1}{4\pi\epsilon_0}\sum_{n=0}^{\infty}\frac{1}{r^{(n+1)}}\int(r')^n P_n(\cos\theta')\rho(\vec{r}')d\tau', \tag{1.8}$$

or, more explicitly,

$$\begin{aligned}V(\vec{r}) &= \frac{1}{4\pi\epsilon_0}\left[\frac{1}{r}\int\rho(\vec{r}')d\tau'+\frac{1}{r^2}\int r'\cos\theta'\rho(\vec{r}')d\tau'\right. \\ &\quad \left.+\frac{1}{r^3}\int(r')^2\left(\frac{3}{2}\cos^2\theta'-\frac{1}{2}\right)\rho(\vec{r}')d\tau'+\cdots\right]. \end{aligned} \tag{1.9}$$

Eq. 1.9 gives the multipole expansion of V in powers of $1/r$. The first term is the monopole contribution that goes like $1/r$; the second is the dipole that goes like $1/r^2$; the third is the quadrupole; the fourth is the octopole; and so on.

From Eq. 1.9, the monopole term can be written as

$$V_{mon}(\vec{r}) = \frac{1}{4\pi\epsilon_0}\frac{Q}{r}, \tag{1.10}$$

where $Q = \int \rho d\tau$ is the total charge of the configuration.

The dipole term from the expansion is

$$V_{dip}(\vec{r}) = \frac{1}{4\pi\epsilon_0}\frac{1}{r^2}\int r' \cos\theta' \rho(\vec{r}')d\tau'. \tag{1.11}$$

Since θ' is the angle between $\vec{r}'$ and $\vec{r}$, and

$$r' \cos\theta' = \hat{\vec{r}} \cdot \vec{r}', \tag{1.12}$$

so that the dipole potential can be re-written as

$$V_{dip}(\vec{r}) = \frac{1}{4\pi\epsilon_0}\frac{1}{r^2}\hat{\vec{r}} \cdot \int \vec{r}' \rho(\vec{r}')d\tau'. \tag{1.13}$$

The integral in Eq. 1.13 does not depend on $\vec{r}$ and is the dipole moment of the distribution,

$$\vec{p} \equiv \int \vec{r}' \rho(\vec{r}')d\tau'. \tag{1.14}$$

The dipole contribution to the potential then simplifies to

$$V_{dip}(\vec{r}) = \frac{1}{4\pi\epsilon_0}\frac{\vec{p} \cdot \hat{\vec{r}}}{r^2}. \tag{1.15}$$

Similarly, the quadrupole term in the multipole expansion can be written as

$$V_{quad}(\vec{r}) = \frac{1}{4\pi\epsilon_0}\frac{1}{2r^3}\sum_{i,j=1}^{3} \hat{r}_i \hat{r}_j Q_{ij}, \tag{1.16}$$

where

$$Q_{ij} \equiv \int [3r'_i r'_j - (r')^2 \delta_{ij}] \rho(\vec{r}') d\tau'. \tag{1.17}$$

δ_{ij} is the Kronecker delta, and Q_{ij} is the intrinsic quadrupole moment of the charge distribution.

One restriction on the multipole moments of nuclei comes from the symmetry of the nucleus, which is in turn directly related to the parity of the nuclear state. Each electromagnetic multipole moment has a parity, determined by the behavior of the multipole operator when $\vec{r}$ is inverted to $-\vec{r}$. The parity of electric moments is $(-1)^L$, where L is the order of the moment ($L = 0$ for monopole, $L = 1$ for dipole, $L = 2$ for quadrupole, etc.). If the multipole operator has odd parity, then the integrand in the expectation value is an odd function of the coordinates and must vanish identically. Thus, all odd-parity static multipole moments must vanish - electric dipole, electric octupole, etc.

The nuclear monopole electric moment is the net nuclear charge Ze, where e is the elementary charge. The nuclear electric dipole moment (EDM) is expected to vanish, as stated above. However, since a nonvanishing electric dipole moment would violate both parity and time-reversal symmetry, various searches for a non-zero EDM are underway. The neutron is a good candidate for this study since it is electrically neutral. The current best upper limit for the neutron EDM is 2.9×10^{-26} e-cm [2], consistent with zero. On the other hand, the result does not rule out the possibility of a small symmetry-violating contribution as expected in the Standard Model.

The nuclear electric quadrupole moment provides a measure of the "shape" of the nucleus. The existence of a nonvanishing electric quadrupole moment implies that the charge distribution of the state is not spherical and the nucleus is axially deformed. Usually nuclei near closed shells are spherical in shape and have small quadrupole moments. In contrast, nuclei in the middle of a major shell are often deformed and their quadrupole moments have large absolute values.

The next higher order non-vanishing electric multipole is hexadecapole (which was not derived above). In general, if an electric hexadecapole moment is present, an electric quadrupole moment will be present as well. Thus, it is not easy to separate contributions from the quadrupole moment from those due to the hexadecapole moment in the observed results. Furthermore, non-spherical nuclei tend to be dominated by the lowest order deformation, that is, the quadrupole. Thus, of the electric multipole moments, the one that is most accessible to evaluate nuclear structure is the quadrupole moment, which provides direct information on the charge distribution inside the nucleus.

1.1.2 Magnetic multipole expansion

A formula for the magnetic vector potential from a localized current distribution, $\vec{J}$, can be obtained along the same lines as the electric potential for a localized charge distribution. Figure 1.2 defines the appropriate geometric variables. The vector po-

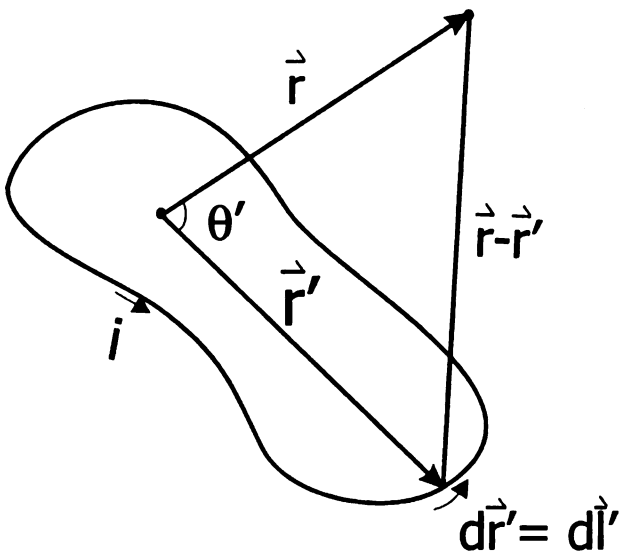

Figure 1.2: Definition of geometric variables used in magnetic vector multipole expansion.

tential, $\vec{A}(\vec{r})$, at $\vec{r}$ arising from a current, i, that is distance $\vec{r}'$ from the origin, is given

by the expression

$$\vec{A}(\vec{r}) = \frac{\mu_0}{4\pi} \int \frac{\vec{J}(\vec{r}')}{\vec{r} - \vec{r}'} d\tau'. \tag{1.18}$$

The integral of the current density, $\vec{J}(\vec{r}')$, over the volume, $d\tau'$, for line and surface currents, is equivalent to

$$\vec{A}(\vec{r}) = \frac{\mu_0}{4\pi} \int \frac{\vec{i}}{\vec{r} - \vec{r}'} dl' = \frac{\mu_0 i}{4\pi} \int \frac{1}{\vec{r} - \vec{r}'} d\vec{l}' \tag{1.19}$$

The vector potential of a current loop can then be written as

$$\vec{A}(\vec{r}) = \frac{\mu_0 i}{4\pi} \oint \frac{1}{\vec{r} - \vec{r}'} d\vec{l}' = \frac{\mu_0 i}{4\pi} \sum_{n=0}^{\infty} \frac{1}{r^{n+1}} \oint (r')^n P_n(\cos\theta') d\vec{l}', \tag{1.20}$$

or, more explicitly:

$$\begin{aligned} \vec{A}(\vec{r}) \;=\; & \frac{\mu_0 i}{4\pi} \left[\frac{1}{r} \oint d\vec{l}' + \frac{1}{r^2} \oint r' \cos\theta' d\vec{l}' \right. \\ & \left. + \frac{1}{r^3} \oint (r')^2 \left(\frac{3}{2} \cos^2\theta' - \frac{1}{2} \right) d\vec{l}' + \cdots \right]. \end{aligned} \tag{1.21}$$

The first term in Eq. 1.21 is the monopole term, the second the dipole term, the third the quadrupole term, and so on.

The magnetic monopole term is always zero, because the integral is the total vector displacement around a closed loop:

$$\oint d\vec{l}' = 0. \tag{1.22}$$

The dipole term is written as

$$\vec{A_{dip}}(\vec{r}) = \frac{\mu_0 i}{4\pi r^2} \oint r' \cos\theta' d\vec{l}' = \frac{\mu_0 i}{4\pi r^2} \oint (\hat{\vec{r}} \cdot \vec{r}') d\vec{l}'. \tag{1.23}$$

The integral can be rewritten in a more illuminating way using a property of the vector area, $\vec{a}$. Note that if the loop is flat, $\vec{a}$ is the ordinary area enclosed, with the

direction assigned by the usual right hand rule

$$\oint (\hat{\vec{r}} \cdot \vec{r}\,')d\vec{l} = -\hat{\vec{r}} \times \int d\vec{a}. \tag{1.24}$$

Then,

$$\vec{A}_{dip}(\vec{r}) = \frac{\mu_0}{4\pi} \frac{\vec{\mu} \times \hat{\vec{r}}}{r^2}, \tag{1.25}$$

where $\vec{\mu}$ is the magnetic dipole moment:

$$\vec{\mu} \equiv i \int d\vec{a} = i\vec{a}. \tag{1.26}$$

The parity of the magnetic multipole operator of order L is $(-1)^{L+1}$. As a result, even-order magnetic multipole moments must vanish for the same reason as odd-order electric multipole moments. In addition, the higher-order nonvanishing magnetic terms are small compared to the magnetic dipole moment, as was the case for terms higher than the electric quadrupole moment. Therefore, the only magnetic multipole moment discussed in terms of the underlying nuclear structure is the magnetic dipole moment, and the terms magnetic dipole moment and magnetic moment are often used interchangeably. When the classical definition of μ in Eq. 1.26 is taken over into quantum mechanics, the magnetic dipole moment for nuclei can be calculated from the nuclear wavefunctions, as will be derived in the following sections. Comparison of calculated values with experiment gives direct and detailed tests of the predicted nuclear structure.

The electric quadrupole moment and magnetic dipole moment are both fundamental in the understanding of nuclear structure. The magnetic moment is sensitive to the single-particle nature of the valence nucleon, and gives direct confirmation of the nuclear wavefunction. The quadrupole moment is sensitive to the collective behavior of the nucleus, and gives direct information on its shape (deformation). Both quantities can be directly compared with the predicted values in different nuclear models and

can help explain changes in shell structure away from stability. The study of nuclear moments near closed shells is especially important as the nucleus can be approximated as an inert core plus an unpaired nucleon (or hole) and the moments can be calculated rather easily. The focus of this dissertation is an examination of the nature of a shell closure removed from the stability line. The nuclear magnetic moment was used as the probe for such study. What follows in the next section is a review of the magnetic moments of nuclei.

1.2 Magnitude of the nuclear magnetic moment

The magnetic moment from the motion of an arbitrary charge can be calculated using classical kinematics. Consider an electron moving in a circular orbit with velocity v, about a point at a constant radius r, as shown in Fig. 1.3.

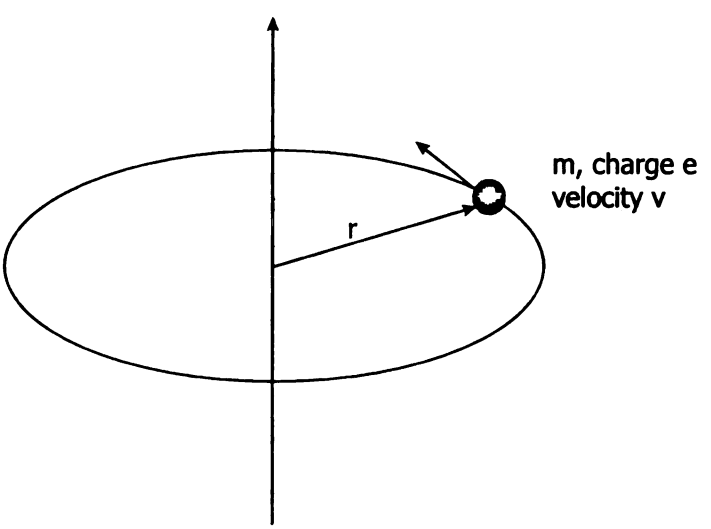

Figure 1.3: Schematic representation of an electron with mass m moving in a circular orbit with radius r.

The magnetic dipole moment was defined in Eq. 1.26 as the product of the current i and the area formed by the electron path, $\vec{a}$. The area of the circle is πr^2, with the direction of the magnetic moment pointing out of the loop. The current i is the

electron charge divided by the time to make a loop, or $e/(2\pi r/v)$. Thus,

$$|\mu| = ia = \left(\frac{ev}{2\pi r}\right)(\pi r^2) = \frac{evr}{2}. \tag{1.27}$$

Recall that the angular momentum of the electron with mass, m, moving in a circle is $l = mvr$, so that the magnetic moment is simply related to l by the expression

$$|\mu| = \left(\frac{evr}{2}\right)\left(\frac{m}{m}\right) = \frac{e}{2m}|\vec{l}| \tag{1.28}$$

where $|\vec{l}|$ is the classical angular momentum. In quantum mechanics, the magnetic moment corresponds to the projection of μ on the rotation axis. Thus, the classical Eq. 1.28 can be "converted" to a quantum mechanical definition by replacing $\vec{l}$ with the expectation value relative to the axis where it has maximum projection, $m_l\hbar$ with $m_l = +l$. Thus,

$$\mu = \frac{e\hbar}{2m}l \tag{1.29}$$

where now l is the angular momentum quantum number of the orbit.

The constants in Eq. 1.29, $(e\hbar/2m)$, are called the Bohr magneton, μ_B, and has the value 9.274×10^{-24} J/tesla. Nucleons behave differently than electrons in terms of their magnetic moments, as will be discussed. None the less, a similar quantity can be obtained for the motion of nucleons which is useful for the discussion of nuclear magnetic moments. Substituting the proton mass for the electron mass in the expression $(e\hbar/2m)$ yields the nuclear magneton $\mu_N = 5.051 \times 10^{-27}$ J/T. Eq. 1.29 can then be rewritten as

$$\mu = g_l l \mu_N \tag{1.30}$$

where the extra factor g_l is the g factor associated with the orbital angular momentum l. g_l is 1 for a proton and 0 for a neutron to reflect the fact that protons are charged, and contribute to the orbital component of the magnetic dipole moment. Neutrons are electrically neutral and their motion does not contribute to the orbital component

of μ.

An equivalent expression to Eq. 1.30 can be written to describe the intrinsic or spin magnetic moments of the fermions as

$$\mu = g_s s \mu_N \tag{1.31}$$

where $s = \frac{1}{2}$ for protons, neutrons, and electrons. The quantity g_s is the spin g factor and can be calculated by solving a relativistic quantum mechanical equation. For a spin $\frac{1}{2}$ point particle, the Dirac equation gives $g_s = 2$. The experimentally measured value for the electron is $g_s = 2.0023$ and the small difference between this value and the Dirac expectation comes from including higher order corrections of quantum electrodynamics. On the other hand, the experimental values for free nucleons are far from the expected value for a point particle:

$$g_s^{\text{proton}} = 5.5856912 \pm 0.0000022 \tag{1.32}$$

$$g_s^{\text{neutron}} = -3.8260837 \pm 0.0000018 \tag{1.33}$$

The proton value is much larger than 2 and the uncharged neutron has a nonzero magnetic moment. The observed deviation from expected values is attributed to the internal structure of the nucleons with internal charged particles in motion (i.e., quarks) that result in currents giving the observed spin magnetic moments. It is noted that g_s for the proton is greater than its expected value by about 3.6, while g_s for the neutron is less than its expected value (zero) by roughly the same amount. The difference has been ascribed to clouds of π mesons that surround the nucleons, with positive and neutral mesons in the proton's cloud, and negative and neutral mesons in the neutron's cloud [5].

The derived spin and orbital components of the magnetic moment of individual nucleons (protons and neutrons) can be used to determine the magnetic moments of

nuclei. The nuclear magnetic dipole moment has contributions from all of the orbital and spin angular momenta, and the magnetic dipole operator for a nucleus can be expressed as a sum of two terms [5]

$$\vec{\mu} = \sum_{k=1}^{A} g_L^{(k)} \vec{L}^{(k)} + \sum_{k=1}^{A} g_S^{(k)} \vec{S}^{(k)}, \tag{1.34}$$

where $\vec{L}^{(k)}$ and $\vec{S}^{(k)}$ are the orbital and spin angular momentum operators for the kth nucleon, summed over all A nucleons in the nucleus. $g_L^{(k)}$ and $g_S^{(k)}$ are known as the orbital and spin nucleon g factors as defined previously. The magnetic moment is obtained by taking the expectation value of the z-component of $\vec{\mu}$ from Eq. 1.34 for the nuclear substate in which $M = J$. Thus, for a nucleus described by total angular momentum quantum number J and magnetic substate M, the wavefunction is ψ_{JM}, and the magnetic moment μ is given by

$$\begin{aligned} \mu &= \int \psi^*_{J,M}(\vec{\mu})_z \psi_{J,M} \\ &\equiv \langle J, M = J | (\vec{\mu}) | J, M = J \rangle \qquad (1.35) \\ &= \langle J, M = J | \sum_{k=1}^{A} g_L^{(k)} \vec{L}^{(k)} + \sum_{k=1}^{A} g_S^{(k)} \vec{S}^{(k)} | J, M = J \rangle \qquad (1.36) \end{aligned}$$

where the integration is over the coordinates (position and spin) of all A nucleons. Then, an equivalent overall expression to Eqs. 1.30 and 1.31 for a nucleus is

$$\mu = g_I I \mu_N \tag{1.37}$$

where g_I is the nuclear g factor, sometimes referred to as the gyromagnetic ratio and written as γ, and I is the nuclear spin.

1.2.1 Single-particle model

The extreme single-particle model is the simplest form of the shell model. It describes a nucleus in which a single unpaired nucleon moves in a central potential formed as a result of the other nucleons in the nucleus. In the single-particle limit, the contributions of all of the paired nucleons exactly cancel so that only the single unpaired nucleon contributes to the overall nuclear magnetic moment and Eq. 1.36 reduces to

$$\mu_{s.p.} = \langle j, m = j | g_l \vec{l} + g_s \vec{s} | j, m = j \rangle \tag{1.38}$$

where $|j, m\rangle$ is the single-particle wavefunction of the unpaired nucleon. Evaluating the expectation value of the vector sum in Eq. 1.38 and given that $\vec{j} = \vec{l} + \vec{s}$, where s is 1/2 for protons and neutrons, the single-particle expression can be simplified further to

$$\mu_{s.p.} = j \left[g_l \pm \frac{g_s - g_l}{2l + 1} \right] \text{ for } j = l \pm \frac{1}{2}. \tag{1.39}$$

Recall that the free nucleon g-factors, g_{free}, are given as

$$g_{l,\text{ free}} = \begin{cases} 1 & \text{for proton} \\ 0 & \text{for neutron} \end{cases} \qquad g_{s,\text{ free}} = \begin{cases} 5.587 & \text{for proton} \\ -3.826 & \text{for neutron} \end{cases} \tag{1.40}$$

and the further assumption is made that the structure of a bound nucleon inside a nucleus is the same as in its free state ($g_l = g_{l,\text{free}}; g_s = g_{s,\text{free}}$). The magnetic dipole moment of an odd-mass nucleus is thus completely determined by the l and j values of the unpaired nucleon in the extreme single particle model.

The magnetic moment for a single nucleon in orbital nlj that is calculated using the free nucleon g factors is known as the single particle, or Schmidt, value. One way to illustrate the connection between the single particle expectation and experiment is to plot experimentally-measured μ against j, along with the calculated Schmidt values. Such diagrams are shown in Figs. 1.4 and 1.5 for odd p and odd n nuclei,

respectively. The Schmidt values are successful in predicting the general trend of

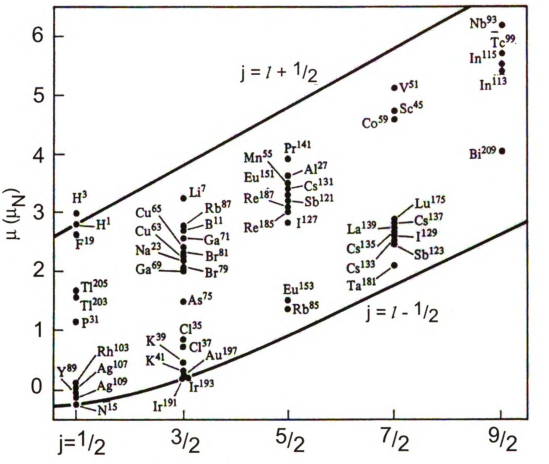

Figure 1.4: Experimental magnetic moments plotted with Schmidt limits for odd proton nuclei. Figure taken from [3].

the magnetic moments of odd-mass nuclei, but the experimental values are generally smaller than the Schmidt values. One limitation of the single particle theory is the assumption $g_s = g_{s,\text{free}}$. The presence of other nucleons, however, introduces meson exchange currents (MEC) that produce an electromagnetic field when the two nucleons interact. In addition, the deviation from the Schmidt values grows as more nucleons are added within a shell, a trend which can be understood by introducing configuration mixing (core polarization) among the single particle states. The basic shell model assumes that the odd nucleon is in a single-particle state, while even small configuration admixtures can appreciably change the magnetic moment. The single

particle model should be taken as a starting point, with corrections added to account for its limitations.

1.2.2 Effective nucleon g factors: microscopic treatment

The limitations of the single-particle model may be compensated for by introducing corrections using perturbation theory. When such corrections are applied, the g factors are no longer given by the free nucleon values, but renormalized due to the presence of other nucleons in the nucleus. The renormalized g factors are called "effective" g factors and have the form $g_{l,\text{eff}} = g_l + \delta g_l$ and $g_{s,\text{eff}} = g_s + \delta g_s$, i.e., the free nucleon value and a correction to it.

Such treatment has been done in Refs. [5,6] starting from an expanded description of the magnetic moment operator:

$$\vec{\mu}_{\text{eff}} = g_{l,\text{eff}}\langle \Sigma l \rangle + g_{s,\text{eff}}\langle \Sigma s \rangle + g_{p,\text{eff}}[Y_2, \langle \Sigma s \rangle], \tag{1.41}$$

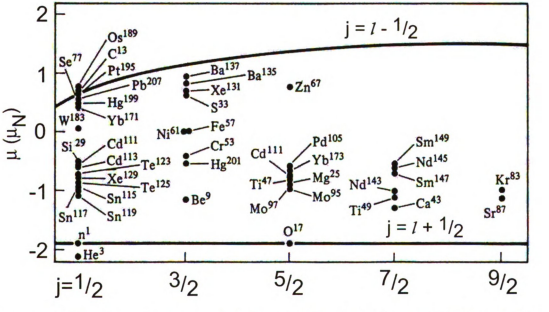

Figure 1.5: Experimental magnetic moments plotted with Schmidt limits for odd neutron nuclei. Figure taken from [3].

where $g_{x,\text{eff}} = g_x + \delta g_x$, with $x = l, s$, or p, and g_p denotes a tensor term. The tensor term contains a spherical harmonic of rank 2 (Y_2) coupled to a spin operator to form a spherical tensor of multipolarity 1. The corrections, δg_x, are computed in perturbation theory for the closed-shell ± 1 configuration.

There have been a number of sources for corrections. Core polarization (CP) is a correction to the single-particle wavefunction that occurs when there is an excitation in the closed-shell core made by a particle in orbital $(l - s)$ coupling to a hole in orbital $(l + s)$. MEC corrections applied to the magnetic moment operator arise from nucleons interacting via the exchange of charged mesons. The isobar correction arises from population of the Δ-isobar resonance, which de-excites by the electromagnetic field (the isobar current). Relativistic corrections to the one-body moment operator to order $(p/M)^3$, where p is a typical nucleon momentum and M is its mass, also can contribute to the magnetic moment. The perturbation treatment has proven effective in reproducing experimental magnetic moments over a large mass region, but at the same time, it is a simple model. There are more complex shell model calculations that use sophisticated wavefunctions that take into account configuration mixing to obtain effective g factors. One such shell model calculation is described in the next section.

1.2.3 Effective nucleon g factors: empirical fit to data

One way to obtain effective g factors is to use shell model wavefunctions with empirical fits to experimental magnetic moment data. The shell model calculation starts with a simple form of the magnetic moment operator $\mu = g_s\langle s\rangle + g_l\langle l\rangle$ where g_l and g_s are the free nucleon g factors defined previously. An effective interaction is generally used to determine the two-body matrix elements for the wavefunction. The wavefunction, therefore, is more sophisticated than the pure single-particle wavefunctions considered in the earlier section. For example, the GXPF1 interaction has proven to be a successful interaction for use in the *fp* shell [4]. The magnetic moment is first cal-

culated with g_{free}. Higher-order corrections such as configuration mixing over many major oscillations, MEC, isobar excitations, and/or other effects should be considered to improve the agreement between the experimental μ and that obtained in the shell model calculations with g_{free}. These higher-order corrections are all represented in effective nucleon g-factors, g_{eff}, that are derived empirically by a least-square fit of the magnetic moment operator to experimental μ in a limited region of nuclei. In general, the values $g_{\text{eff}} = 0.6 g_{\text{free}}$ have been found to be in reasonable agreement with data [8].

1.3 Analysis of mirror moments

It has been shown in the previous section that the magnetic moment of a nucleus can be calculated and compared to experimental values to learn about nuclear structure. Going one step further, the simultaneous consideration of the magnetic dipole moments of mirror nuclei can provide a framework to test present day nuclear structure models. A pair of mirror nuclei have the numbers of protons and neutrons interchanged. For example, the mirror partner of $^{55}_{28}\text{Ni}_{27}$ is $^{55}_{27}\text{Co}_{28}$. Analyses have been carried out on the magnetic moments of mirror pairs and certain regularities have been observed. Two approaches described below amplify the different aspects of studies with mirror nuclei.

1.3.1 Isoscalar spin expectation value

Examination of the specific contribution from nuclear spins to the magnetic moment can provide insight into shell structure and configuration mixing. The magnetic moment can be expressed as the sum of the expectation values of isoscalar $\langle \sum \mu_0 \rangle$ and

isovector $\langle \sum \mu_z \rangle$ components, assuming isospin is a good quantum number, as

$$\mu = \left\langle \sum \mu_0 \right\rangle + \left\langle \sum \mu_z \right\rangle \tag{1.42}$$

$$= \left\langle \sum \frac{l_z + (\mu_p + \mu_n)\sigma_z}{2} \right\rangle + \left\langle \sum \frac{\tau_z[l_z + (\mu_p - \mu_n)\sigma_z]}{2} \right\rangle, \tag{1.43}$$

where l and σ are the orbital and spin angular-momentum operators of the nucleon, respectively, τ is the isospin operator, $\mu_p = 2.793\,\mu_N$ and $\mu_n = -1.913\,\mu_N$ are the magnetic moments of free proton and neutron, respectively, and the sum is over all nucleons. The isovector $\langle \sum \mu_z \rangle$ part depends on the isospin, τ_z, and changes its sign for $T_z = \pm T$. The isoscalar spin expectation value $\langle \sum \sigma_z \rangle$ can be extracted from the sum of mirror pair magnetic moments as

$$\left\langle \sum \sigma_z \right\rangle = \frac{\mu(T_z = +T) + \mu(T_z = -T) - I}{\mu_p + \mu_n - 1/2}, \tag{1.44}$$

where the total spin is $I = \langle \sum l_z \rangle + \langle \sum \sigma_z \rangle /2$.

Sugimoto [9] and later Hanna and Hugg [10] analyzed data on magnetic moments of mirror nuclei, and found regularities in the spin expectation values as a function of mass. All of the ground state magnetic moments of $T = 1/2$ mirror nuclei have been measured in the *sd* shell and a systematic trend has been established, as shown in Fig. 1.6. The values of $\langle \sum \sigma_z \rangle$ are close to the single-particle value at the beginning and end of a major shell, and decrease approximately linearly with mass number in the region in between, reflecting core polarization effects. All values for the $T = 1/2$ mirror nuclei in the *sd* shell lie within the single particle model limits.

1.3.2 Buck-Perez mirror analysis

Buck and Perez *et al.* analyzed the magnetic moments of mirror nuclei in a different framework. They studied the relationship between gyromagnetic ratios for odd proton, γ_p, and odd neutron, γ_n, nuclei and the strengths of the β-decay transitions of mirror

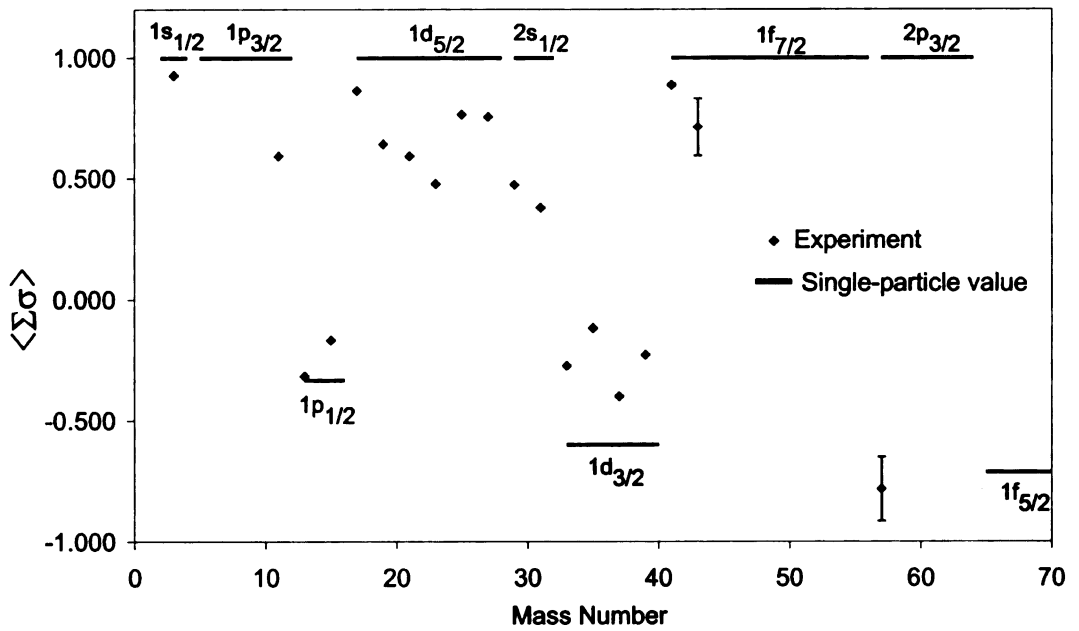

Figure 1.6: Isoscalar spin expectation values for $T = 1/2$ mirror nuclei. The single-particle limits for each orbital are shown by the black horizontal lines.

nuclei [11–13]. Assuming the contributions from the even nucleon to the z components of the total spin S and total angular momentum J of the mirror pair are small, they derived the following relation:

$$(\gamma_p + \Delta\gamma_p) = \alpha(\gamma_n + \Delta\gamma_n) + \beta, \tag{1.45}$$

with $\alpha = (g_s^p - g_l^p)/(g_s^n - g_l^n)$ and $\beta = g_l^p - \alpha g_l^n$ with the free-nucleon values of the g factors $g_l^p = 1.0$, $g_l^n = 0.0$, $g_s^p = 5.586$, $g_s^n = -3.826$. The $\Delta\gamma_{p,n}$ are corrections to the gyromagnetic ratios because the even terms, S_{even} and J_{even}, are small. Such treatment is different from the analysis of the isoscalar spin expectation value as α is a ratio of g factors for the proton and neutron. Therefore, any "effective" quenching of the g factors is cancelled. A plot of γ_p against γ_n revealed a linear trend, as shown in Fig. 1.7 for all known $T = 1/2$ mirror pairs. The single-particle values for γ_p and γ_n lie close to this line, but the interesting feature is that the points representing measured magnetic moments deviate from those estimates simply by sliding along

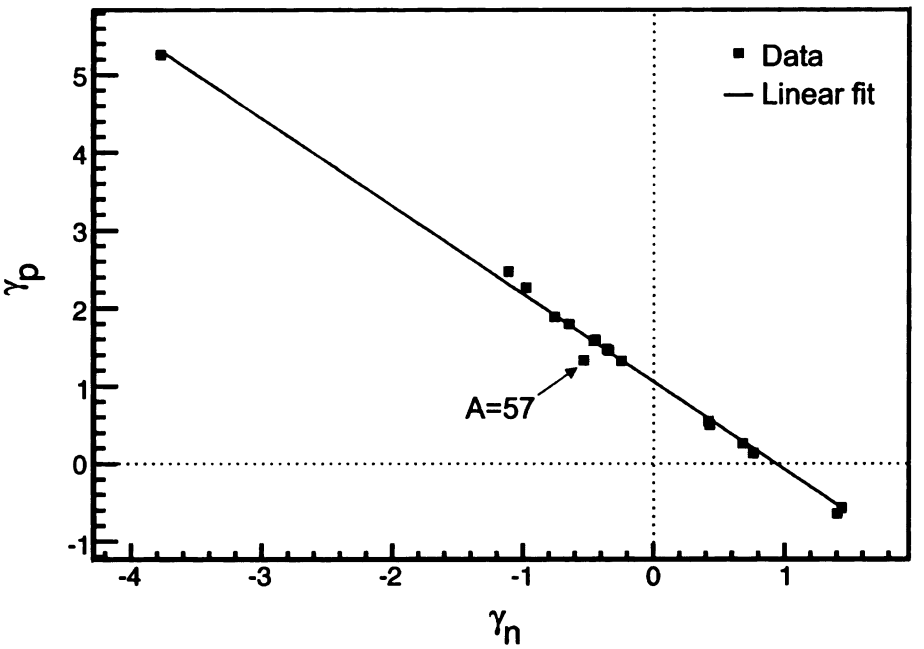

Figure 1.7: Nuclear g factors of $T = 1/2$ mirror pairs plotted as the odd proton nucleus g factor γ_p versus the odd neutron nucleus g factor γ_n, also known as a Buck-Perez plot. The squares are the experimental data and the solid line is a linear fit to the data.

the same line [11].

The total spin is related to the Gamow-Teller matrix element for the cross-over β-decay obtained from the ft value for $T = 1/2$ mirror pairs and thus the following relations are also true:

$$(\gamma_p + \Delta\gamma_p) = g_l^p + \frac{g_s^p - g_l^p}{R}\gamma_\beta \tag{1.46}$$

and

$$(\gamma_n + \Delta\gamma_n) = g_l^n + \frac{G_s^n - g_l^n}{R}\gamma_\beta. \tag{1.47}$$

In Eqs. 1.46 and 1.47, R is the ratio of the axial-vector coupling constant, C_A, to the vector coupling constant, C_V, and γ_β is a variable related to the β-decay ft value

$$|\gamma_\beta| = \frac{1}{2}\left[\left(\frac{6170}{ft} - 1\right)\frac{1}{J(J+1)}\right]^{1/2}. \tag{1.48}$$

The free-nucleon value for R is $R = |C_A/C_V| = 1.26$.

When the value of γ_β is known for a particular nucleus, the value of $\gamma_{n,p}$ can be deduced for that nucleus using Eqs. 1.46 and 1.47. A second prediction can be made when $\gamma_{p,n}$ is known for the mirror partner using Eq. 1.45. The Buck-Perez extrapolation is a valid prediction for nuclei with unknown magnetic moments, and an important tool for future measurements. Specifically, in the fp shell, many magnetic moments of $T_z = +1/2$ nuclei are known and can be used to predict μ for the unknown $T_z = -1/2$ mirror partners.

1.4 Nuclear moments and nuclear structure

Comparison of both the magnetic moment and isoscalar spin expectation value to model predictions provides a test of the shell closure and shell evolution. The properties of nuclei near double shell closures, in particular, are of interest as these nuclei generally have very simple structures compared to their neighbors. The magnetic moment is one such property that is sensitive to which orbits are occupied by the valence particles, and is therefore essential in the investigation of double shell closures.

1.4.1 Magnetic moments near closed shells

The character of stable nuclei with magic numbers of both protons and neutrons, such as ^{16}O and ^{40}Ca, has been well established. The radioactive doubly magic nuclei, however, have revealed interesting surprises. An extreme example is that of ^{28}O, which was expected to be bound based on its doubly-magic character (proton and neutron numbers $Z = 8$ and $N = 20$, respectively), but has been shown to be unbound [14]. The study of β unstable ^{56}Ni, residing three neutrons away from the lightest stable nickel isotope, may provide insight into changes in the structure of doubly-magic nuclei as one moves away from stability. All eight magnetic moments of the eight neighbors to the doubly-closed shell ^{16}O and ^{40}Ca ($\pm$ 1 nucleon) nuclei are experimentally known [15–22] and agree well with the values obtained assuming an inert core $\pm$

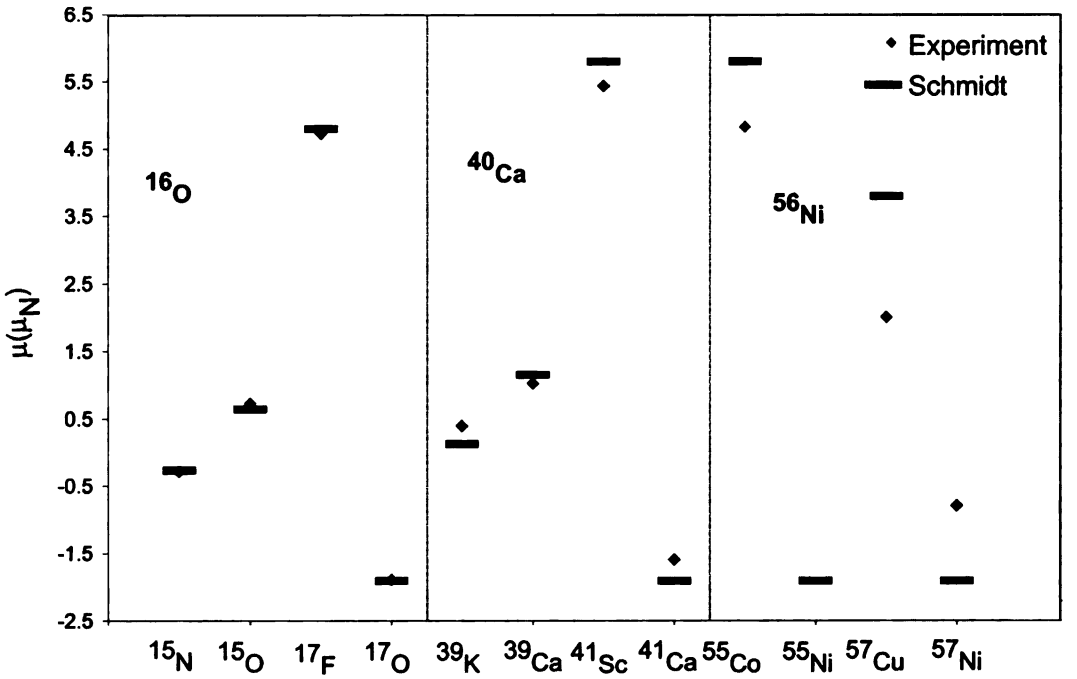

Figure 1.8: Experimental magnetic moment values compared to Schmidt limits for nuclei around ^{16}O, ^{40}Ca, and ^{56}Ni.

1 nucleon (single-particle value), as shown in Fig. 1.8. The agreement reflects the inertness of the ^{16}O and ^{40}Ca cores. The nucleus ^{56}Ni is the first self-mirror nucleus, with closed-shell neutron and proton numbers ($N = Z = 28$), that is radioactive. The three known magnetic moments of neighbors to ^{56}Ni [23–25] do not agree with single-particle values. The discrepancy indicates the necessity of corrections to the simple picture of a ^{56}Ni closed shell. The ^{56}Ni core is better described by the lowest order configuration of nucleons plus a sizable mixture of other configurations, in other words, the ^{56}Ni core is not very inert, that is "soft".

1.4.2 Evidence of ^{56}Ni as a doubly-magic nucleus

The softness of the ^{56}Ni core also appears in contradiction to the behavior of the first excited 2^+ state and the reduced transition matrix element, $B(E2; 0_1^+ \rightarrow 2_1^+)$, in the even-A Ni isotopic chain. The energy of the 2_1^+ state in ^{56}Ni is $E(2_1^+) = 2701$ keV and lies significantly higher in energy than $E(2_1^+)$ in the neighboring even-even

nuclei, which is indicative of a shell closure. On the other hand, $B(E2;0_1^+ \rightarrow 2_1^+)$ in ^{56}Ni has been deduced from a variety of experimental methods with a variety of results. A lifetime measurement using the Doppler-shift attenuation method yielded $B(E2;0_1^+ \rightarrow 2_1^+) = 385(160)e^2$ fm^4 [26] and Kraus *et al.* performed a proton scattering experiment that gave a higher value of $B(E2;0_1^+ \rightarrow 2_1^+) = 600(120)$ e^2 fm^4 [27]. Two intermediate-energy Coulomb excitation measurments by Yanagisawa *et al.*, yielding $B(E2;0_1^+ \rightarrow 2_1^+) = 580(70)$ e^2 fm^4 [28], and Yurkewicz *et al.*, where $B(E2;0_1^+ \rightarrow 2_1^+) = 494(119)$ e^2 fm^4 was deduced [29], support the higher value obtained from proton scattering. A summary of the experimental results for $E(2_1^+)$ and $B(E2;0_1^+ \rightarrow 2_1^+)$ values for the Ni isotopes are depicted in Fig. 1.9. While there is a range of experimental values for $B(E2;0_1^+ \rightarrow 2_1^+)$ at ^{56}Ni, the overall trend is that the $B(E2;0_1^+ \rightarrow 2_1^+)$ for ^{56}Ni is not reduced, within error, with respect to neighboring even-even Ni isotopes, as expected for a good core. Yet, the high $E(2_1^+)$ value for ^{56}Ni is indicative of a good core. The disparate nature between the $E(2_1^+)$ and $B(E2;0_1^+ \rightarrow 2_1^+)$ in ^{56}Ni was explained by a large scale shell model calculation with the quantum Monte Carlo diagonalization method in the full *fp* shell [31]. The calculation reproduced the experimentally-observed $E(2_1^+)$ and $B(E2;0_1^+ \rightarrow 2_1^+)$ using the FPD6 interaction, wherein the probability of the $N = Z = 28$ closed shell component in the wavefunction of the ^{56}Ni ground state is only 49%, compared to an 86% closed shell component in the wavefunction of the ^{48}Ca ground state.

1.4.3 Magnetic moments around ^{56}Ni

The four nuclei that lie one nucleon away from ^{56}Ni are ^{55}Ni (neutron hole in the $1f_{7/2}$ shell), ^{57}Cu (proton particle in the $2p_{3/2}$ shell), ^{57}Ni (neutron particle in the $2p_{3/2}$ shell), and ^{55}Co (proton hole in the $1f_{7/2}$ shell). The measured magnetic moments of ^{55}Co [25] and ^{57}Ni [24], isospin projection $T_z = 1/2$ nuclei, are well reproduced by shell model calculations [4], and support ^{56}Ni as being a soft core (see Fig. 1.10). The magnetic moment of the $T_z = -1/2$ nucleus ^{57}Cu was measured to be $|\mu(^{57}\text{Cu})| =$

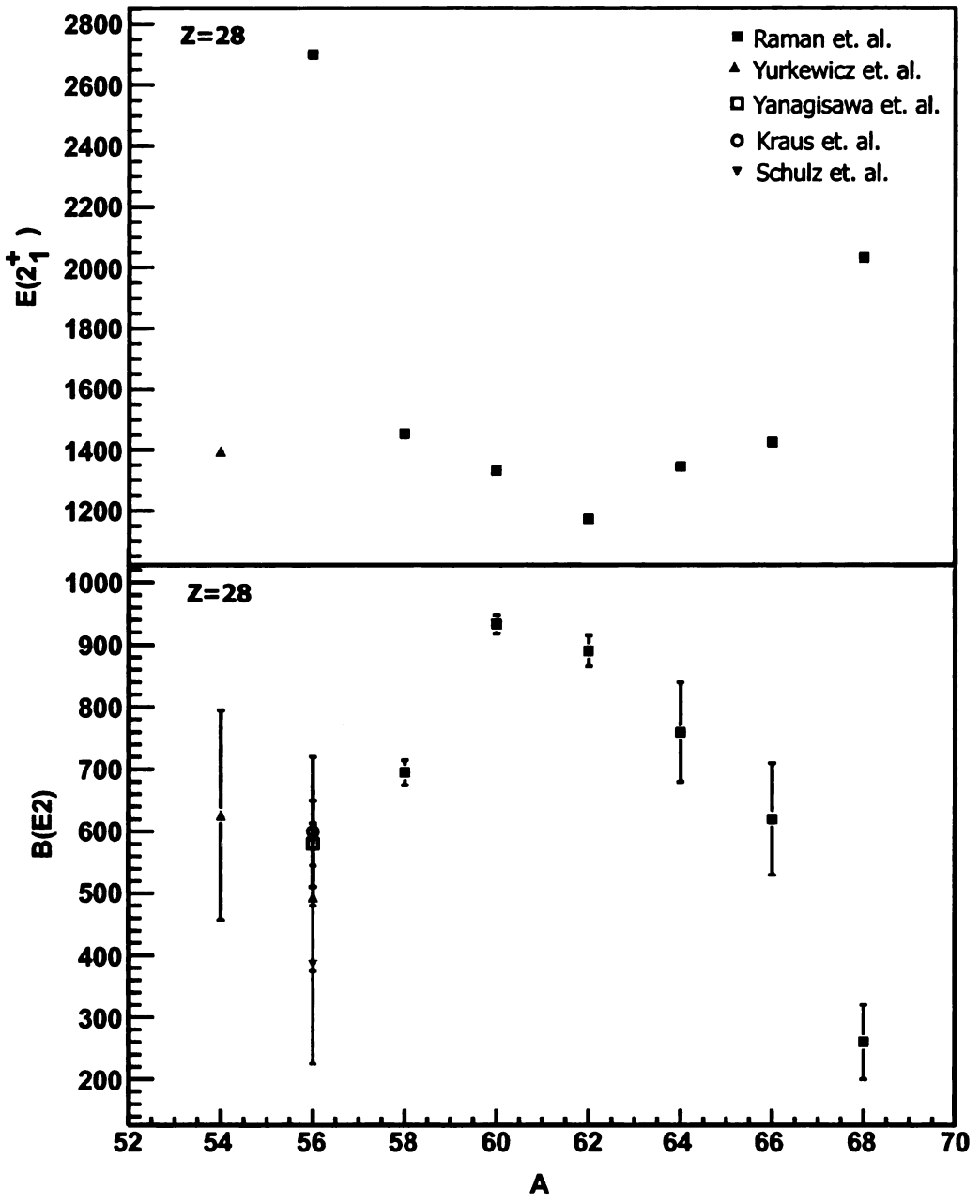

Figure 1.9: Experimental $E(2_1^+)$ and $B(E2; 0_1^+ \rightarrow 2_1^+)$ for the Ni isotopes. Values taken from [26–30].

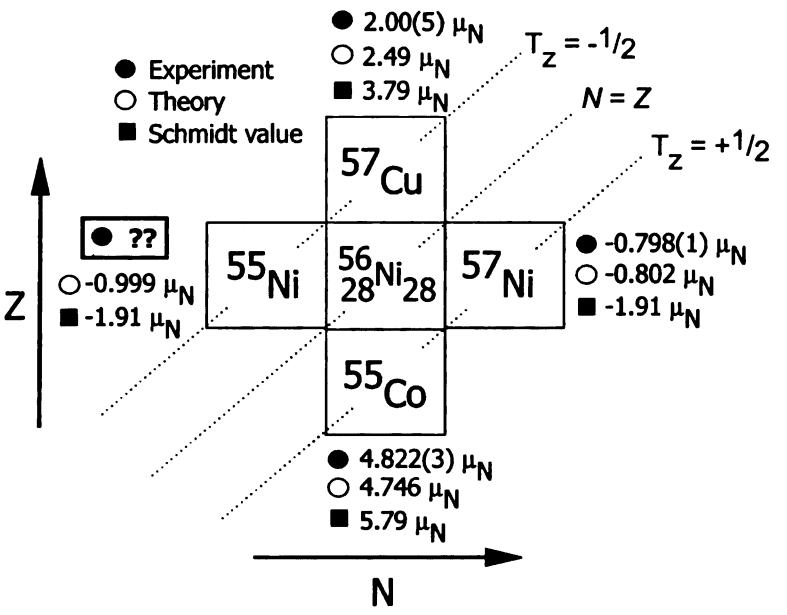

Figure 1.10: Experimental magnetic moment values of nuclei one nucleon away from ^{56}Ni compared to shell model calculation using GXPF1 interaction [4]. Note the discrepency in the value for ^{57}Cu as discussed in the text.

(2.00 $\pm$ 0.05) μ_N [23]. The same shell-model calculation for ^{57}Cu gives $\mu(^{57}\text{Cu})$= 2.45 μ_N [4], suggesting a major shell breaking at ^{56}Ni. All of the other odd-mass Cu isotopes have magnetic moments which agree well with theoretical predictions (see Fig. 1.11). The one μ value not yet attained is that for the one neutron hole nucleus ^{55}Ni.

1.4.4 Proposed $\mu(^{55}\text{Ni})$ measurement

The measurement of $\mu(^{55}\text{Ni})$ can provide important information on the $N = Z = 28$ doubly-magic shell closure, as ^{55}Ni is one neutron removed from the core. The anomolous $\mu(^{57}\text{Cu})$ leaves the open question of whether the one neutron hole in $1f_{7/2}$ in ^{55}Ni, also with $T_z = -1/2$, shows the same deviation from shell model as the one proton particle does for ^{57}Cu.

The theoretical calculations discussed in the previous sections were carried out for $\mu(^{55}\text{Ni})$ and the results are shown in Table 1.1. The calculation with g_{free} refers to the

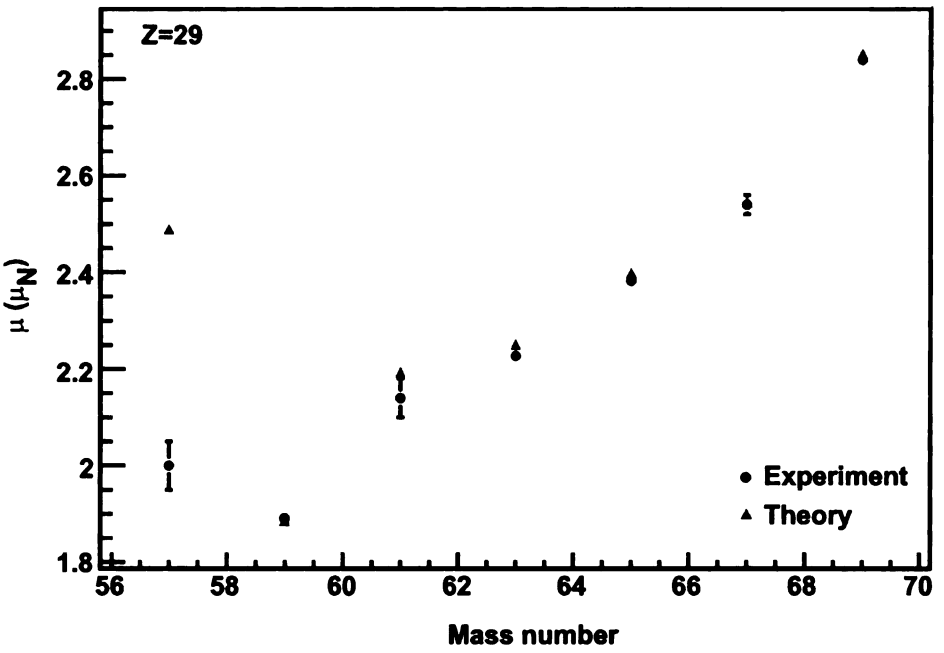

Figure 1.11: Magnetic moments of the odd-mass Cu isotopes compared to theory. Theory is a shell model calculation using the GXPF1 interaction and effective nucleon g-factors. All values were taken from Ref. [32].

shell model calculation with GXPF1 and free nucleon g factors, while the calculation with $g_{\text{eff}}^{\text{moments}}$ is the same shell model calculation with effective g factors obtained from an empirical fit to data (section 1.2.3). The calculation with $g_{\text{eff}}^{\text{perturbation}}$ refers to the microscopic treatment that added corrections to the magnetic moment operator through perturbation theory (section 1.2.2). The Buck-Perez predictions (section 1.3.2) were determined from the known ft value for ^{55}Ni, and in a separate prediction from the known $\mu(^{55}\text{Co})$.

A new value for $\mu(^{55}\text{Ni})$ can also be combined with the known magnetic moment of its mirror partner ^{55}Co to deduce the isoscalar spin expectation value for the mass $A = 55$ system. All of the ground state magnetic moments of $T = 1/2$ mirror nuclei have been measured in the sd shell and a systematic trend of $\langle \sum \sigma_z \rangle$ as a function of mass has been established. In the fp shell, however, only three mirror pairs have been measured, masses $A = 41$, 43, and 57, and no systematic behavior has been

Table 1.1: Theoretical expectations for the magnetic moments of ^{55}Ni.

Theory	$\mu(^{55}\mathrm{Ni})\ \mu_N$
with g_{free}	-0.809[a]
with $g_{\mathrm{eff}}^{\mathrm{moments}}$	-0.999[a]
with $g_{\mathrm{eff}}^{\mathrm{perturbation}}$	-1.072[b]
Buck-Perez (dependence on ft value)	-0.872 ± 0.081[c]
Buck-Perez (linear trend of experimental g factors)	-0.945 ± 0.039[c]
Single-particle value	-1.913

[a]From Ref. [4]
[b]Private Communication with I.S. Towner
[c]From Ref. [13]

established. It is essential to measure more mirror magnetic moment pairs in this region in order to explore nuclear structure in the fp shell and beyond.

The magnetic moment of ^{55}Ni was measured to address questions regarding the ^{56}Ni core. Comparison of both the deduced $\mu(^{55}\mathrm{Ni})$ and $\langle\sum\sigma_z\rangle$ for the $T = 1/2$, A=55 system with theory provides important information on the structure of doubly-magic nuclei as one moves further from stability.

1.5 Organization of Dissertation

An introduction to the nuclear magnetic dipole moment was presented in this chapter, as well as a motivation for the measurement of $\mu(^{55}\mathrm{Ni})$. In Chapter 2, the experimental technique of nuclear magnetic resonance of β-emitting nuclei (β-NMR), used to complete the $\mu(^{55}\mathrm{Ni})$ measurement, is described. Chapter 3 contains details of the experimental setup including production of the spin polarized ^{55}Ni fragments and the β-NMR apparatus. The results of the experiment are given in Chapter 4, followed by a discussion of these results in Chapter 5. Chapter 6 concludes with a summary of the present experiment, and outlook on the future of magnetic moment measurements at NSCL.

Chapter 2

Technique

Methods for measuring the magnetic dipole moment of the nuclear ground state depend on the interaction between the magnetic moment and a magnetic field. One of the earliest methods is the technique of nuclear magnetic resonance (NMR), pioneered in 1946 by Purcell [33]. NMR measurements rely on an external magnetic field to break the degeneracy of the magnetic substates, and spins being distributed among those substates according to Boltzmann's law, with the lower levels slightly more populated than the upper levels. When an oscillating magnetic field is applied perpendicular to the external field, the resonance absorption of electromagnetic energy can occur if there is any population difference. Conventional NMR methods typically require approximately 10^{17} nuclei for an observable resonance due to the very small population imbalance of the magnetic substates at room temperature. This technique is also restricted to stable or long-lived nuclear states due to the time required to make such an NMR measurement, on the order of several minutes.

A variation of the NMR technique has been applied to β-emitting nuclei to measure the ground state nuclear moments for short-lived nuclei on the order of 10^{-2} to 10^{3} s. The so-called β-NMR technique requires an external magnetic field of order 10^{-1} T and the observation of the angular distribuition of β particles from a spin-polarized nucleus, and will be described in more detail in the following sections.

Collinear laser spectroscopy has been employed to measure nuclear moments as well. Lasers are used to scan the hyperfine structure of atomic transitions and the relevant energy splittings are determined from the observed resonance frequencies. The magnetic moment is deduced from the strength of the hyperfine interaction, which is obtained from the energy splitting. Further, lasers can be used to spin polarize nuclei via optical pumping with circularly polarized light. The resulting spin-polarized ensemble can then be measured with β-NMR to determine nuclear moments. NSCL is developing a laser system as a promising avenue for future measurements of nuclear spin, charge radii, and nuclear moments.

In the work described in this dissertation, the β-NMR method was applied to deduce the magnetic moment of ^{55}Ni. ^{55}Ni is suited to the β-NMR technique since ^{55}Ni decays via β^+ emission with a half life of 204 ms. The remainder of this chapter will describe in detail the necessary components for the β-NMR measurement including: 1) production of spin-polarized nuclei, 2) β-decay angular distribution from a spin-polarized nucleus, 3) measurement of the spin polarization, and 4) measurement of the magnetic moment with the β-NMR technique.

2.1 Nuclear spin polarization

Nuclear spin polarization is a necessary condition for many types of physics experiments, including β-NMR spectroscopy. Spin polarization occurs when the population for a given magnetic substate, m, is not equal to the population for the opposite substate $-m$, and a linear distribution among the m states is present (see Fig. 2.1). Spin polarization is generally discussed in terms of the statistical tensor, ρ, which characterizes the orientation of a particular state [34]. The spin polarization for a given spin value I is defined as the ratio of the statistical tensor $\rho_1(I)$ to its value for

maximum spin polarization $\rho_1^{max}(I)$. Thus, with

$$\rho_1(I) = -\sum_m \frac{mP(m)}{\sqrt{I(I+1)}} \tag{2.1}$$

and

$$\rho_1^{max}(I) = \frac{-I}{\sqrt{I(I+1)}} \tag{2.2}$$

the spin polarization is

$$\frac{\rho_1(I)}{\rho_1^{max}(I)} = \sum_m \frac{mP(m)}{I} \equiv \left\langle \frac{I_z}{I} \right\rangle, \tag{2.3}$$

where $P(m)$ is the normalized population for substate m [$\sum_m P(m) = 1$]. Thus, spin polarization is a measure of the orientation of the total angular momentum relative to a fixed axis (z).

Several methods are commonly used to produce spin polarized nuclei for β-NMR studies. Low-temperature nuclear orientation uses a strong external magnetic field to break the degeneracy of the magnetic substates. The population of the states follows the Boltzmann distribution law, as described previously. The splitting of the state should be of order kT for a measurable polarization effect, namely $g\mu_N H_0 = kT$, where H_0 is the strength of the magnetic field, k is the Boltzmann constant, and T is the temperature. The condition is that $H_0/T = 2.8 \times 10^3$ T/K for a state with $g\mu_N = 1\mu_N$. A successful measurement then requires temperatures as low as 0.002

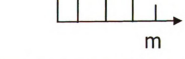

Figure 2.1: Population distribution of a spin polarized system with respect to magnetic substate for a nucleus with $I = 3/2$.

K when an external field of 5 T is used. Such conditions have been achieved but are not well suited to projectile fragments.

Spin polarized nuclei can also be produced by laser optical pumping as mentioned previously. Optical pumping relies on the fact that if the electronic spins can be oriented, the hyperfine coupling will cause the nuclear spin to be oriented as well. Circularly polarized light is used to excite atomic transitions in an atom to a single F-spin atomic sublevel. The nuclear spin then follows the orientation of the electron spins, and a nuclear spin polarization is produced. This technique requires very low and well defined velocities that have only recently been obtained for projectile fragments [35].

Another method to produce spin polarization for β-NMR is via nuclear reactions. When reaction products are collected away from the incident beam axis, the outgoing particle and residual nucleus from a reaction will be spin polarized. Transfer reactions such as (d,p) are particularly effective, as well as other types of reactions. At NSCL, rare isotopes are produced by intermediate-energy heavy-ion reactions, in which spin polarization at small angles has been observed. Spin polarization of projectile-like residues from intermediate-energy heavy-ion reactions was first reported at the Institute of Physical and Chemical Research (RIKEN) of Japan in the peripheral reaction ^{197}Au(^{14}N,^{12}B) at a primary beam energy of 40 MeV/nucleon [36]. The spin polarization, as a function of momentum, was observed to follow an S-shaped curve, with zero polarization at the peak of the yield distribution, and maximum polarization (as large as 20%) at the wings of the momentum distribution. A qualitative description of the polarization mechanism was found in a classical kinematic model that considers conservation of linear and angular momenta and assumes peripheral interactions between the fast projectile and target. Figure 2.2 presents a schematic of the expected polarization and yield for the nucleon removal process for fragmentation of a projectile on a heavy target.

A systematic study of spin polarization following few-nucleon removal from light

projectiles as a function of beam energy and target nucleus was completed by Okuno *et al.* [37]. This study demonstrated that the relation between the outgoing fragment momentum and the sign of spin polarization depended on the mean deflection angle $\bar{\theta}_{def}$. Near-side reactions occur for high-Z targets, where the Coulomb deflection dominates the internuclear potential between projectile and target (see Fig. 2.3). Near-side reactions give the polarization dependence shown in Fig. 2.2. The nucleon-nucleon potential governs removal reactions on low-Z targets. Far-side reactions prevail in this case, in which the path of the fragment is toward the target, and the sign of the observed polarization is reversed.

The spin polarization has a near-zero value at the peak of the fragment yield curve for both near- and far-side dominated reactions, since $|\bar{\theta}_{def}|$ is large. This behavior can be qualitatively understood from the projectile rest-frame diagram in Fig. 2.2. The removed nucleons have momentum K. The z component of the induced angular momentum of the projectile-like species is $z = -Xk_y + Yk_x$, where X, Y

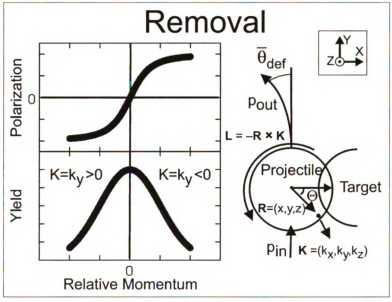

Figure 2.2: Illustration of nuclear spin polarization produced in a nucleon removal reaction at intermediate energies, for a high Z target. The yield and polarization curves are given relative to the incident projectile momentum. The removal schematic is given in the projectile-like rest frame (see text for definition of terms).

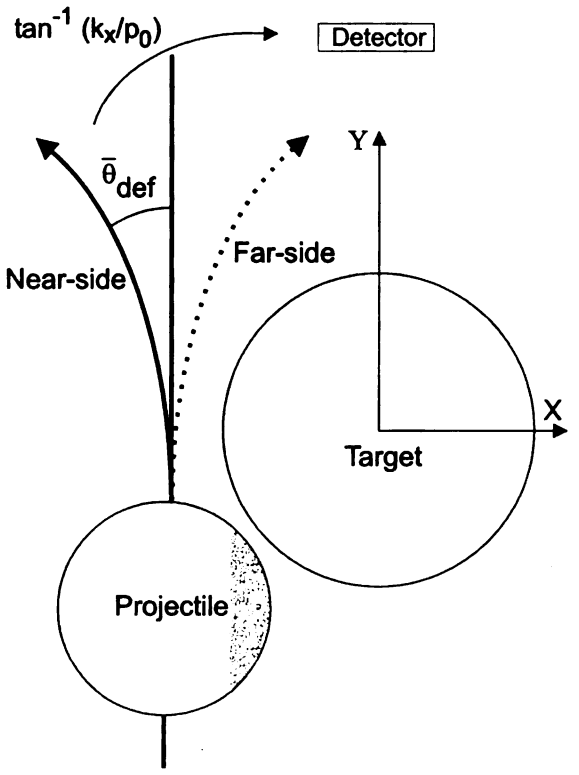

Figure 2.3: Schematic of near- and far-side reactions.

are the localized Cartesian coordinates of the removed nucleon(s), and k_x, k_y are the momentum components of the removed nucleons in the reaction plane. If the nucleon removal occurs uniformly in the overlap region, $X \sim R_0$ (the radius of the projectile), $Y \sim 0$, then $z = -Xk_y$. Zero polarization will therefore result when the fragment momentum equals the projectile momentum, since $k_y = 0$ in the projectile rest frame under these conditions.

If nucleon removal is not uniform in the overlap region, $Y \neq 0$ and the term Yk_x can contribute to z. Such a contribution will only be observed experimentally when $|\bar{\theta}_{def}|$ is small. The final scattering angle of the fragment is $\theta_L = \bar{\theta}_{def} + \Delta\theta$, where $\Delta\theta$ is the change in angle caused by the transverse momentum component of the removed nucleons, $\Delta\theta = \tan^{-1}(-k_x/p)$. Here, p is the total momentum of the projectile-like fragment. In reactions where $|\bar{\theta}_{def}| \sim 0$, it is the transverse momentum component of the removed nucleon(s) that "kicks" the fragments to small angles, and the resulting polarization is negative since $k_x > 0$ to give a positive $\Delta\theta$ and $Y < 0$ for non-uniform nucleon removal as illustrated in Fig. 2.2.

As stated earlier, the nuclei must be spin polarized to perform a β-NMR measurement. There is a strong dependence of polarization on the momentum (yield distribution) of the fragment nucleus, therefore it is crucial to know the magnitude of polarization prior to the experiment. While fragmentation reactions provide one means of producing spin-polarized exotic nuclei, these nuclei tend to be produced at low rates. A useful figure of merit for β-NMR measurements is P^2Y, where P represents polarization and Y is yield, since the optimization of polarization with yield is critical. Improvements in yield will come with the development of new radioactive ion beam (RIB) facilities, but while yields remain small, the ability to accurately predict the expected polarization is required for experimental success. A Monte Carlo code was developed [37] based on the ideas discussed above to simulate the spin polarization generated in nucleon removal reactions at intermediate energies. The general behavior of spin polarization as a function of projectile-like momentum was reproduced,

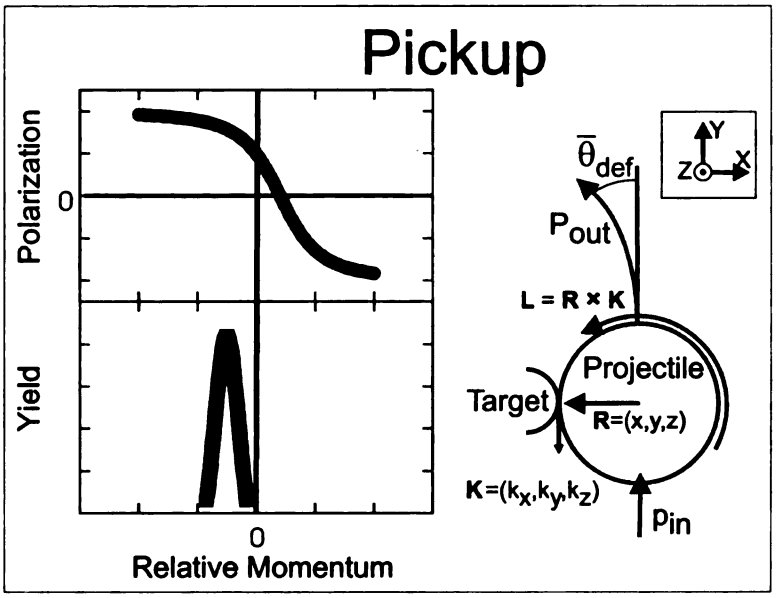

Figure 2.4: Illustration of nuclear spin polarization produced in a nucleon pickup reaction at intermediate energies, for a high Z target. The yield and polarization curves are given relative to the incident projectile momentum. The pickup schematic is given in the projectile-like rest frame.

although a scaling factor of 0.25 was needed to match the magnitude of polarization observed experimentally. Previous work at NSCL improved the quantitative performance of this Monte Carlo approach. The progress made in this area will be discussed later in detail in section 5.1.

While nucleon removal at intermediate energies has been shown to produce spin polarization, certain nuclei are more easily produced via other reactions, such as nucleon pickup. Spin polarization in nucleon pickup reactions at intermediate energies was first demonstrated at NSCL [38]. Positive spin polarization was determined for ^{37}K nuclei collected at small angles from the reaction of 150 MeV/nucleon ^{36}Ar projectiles with a ^{9}Be target. Figure 2.4 illustrates the features of spin polarization and yield from nucleon pickup reactions. The key to understanding the observed spin polarization in the pickup process is the knowledge that the picked-up nucleon must have an average momentum equal to the Fermi momentum oriented parallel to the beam direction. Souliotis *et al.* [39] showed this to be the case based on the observed

shifts in the centroids of the longitudinal momentum distributions for one- and two-nucleon pickup products. The average projectile-like momentum $\langle p \rangle$ was found to satisfy the relation $\langle p \rangle = \langle p_p \rangle + \langle p_t \rangle$, where $\langle p_p \rangle$ is the average momentum of the projectile and $\langle p_t \rangle$ is the average momentum of the picked-up nucleon, which is equal to the Fermi momentum.

The momentum of the picked-up nucleon will be antiparallel to the incoming projectile momentum in the rest frame of the projectile-like species. The z component of orbital angular momentum induced by the nucleon pickup process is $l_z = R\Delta p$, where Δp is the momentum difference between the projectile and the picked-up nucleon, assuming a peripheral interaction where the nucleon is picked up to a localized position on the projectile given by R in Fig. 2.4. l_z and thus the spin polarization will be zero when the momentum of the picked-up nucleon matches the momentum of the incoming projectile ($\Delta p = 0$). This zero crossing occurs at the projectile-like momentum $p = [(A_p + 1)/A_p]p_p$, where A_p and p_p are the mass number and momentum of the projectile, respectively. A linear increase in l_z is expected with a decrease in the momentum of the outgoing pickup product. Groh *et al.* [38] found that proton pickup reactions follow the trend shown in Fig. 2.4, except for the low momentum side of the momentum distribution. At low momentum values of the pickup products, the momentum matching conditions for pickup are no longer satisfied, and the spin polarization is observed to rapidly approach zero.

Turzó *et al.* showed that neutron pickup reactions at intermediate energies behave in a similar manner [40]. Turzó *et al.* extended the Monte Carlo simulation of Ref. [37] to include nucleon pickup and the momentum considerations discussed by Groh *et al.* [38]. Qualitative agreement of the observed spin polarization as a function of the projectile-like product was found, as was the case with nucleon removal reactions. However, the scaling factor of 0.25 was again needed to reproduce the magnitude of the observed spin polarization. The requirement of scaling factors of the same magnitude for both nucleon removal and nucleon pickup suggest that the same quantitative

correction factors should apply to both and has been demonstrated in Ref. [41]. As noted earlier, additional components have been added to the Monte Carlo simulation to achieve better quantitative agreement with data, and will be described in section 5.1.

The kinematic model proposed by Asahi *et al.* has been successfully employed to quantitatively explain spin polarization at intermediate energies for both nucleon removal and pickup reactions [41]. Further, polarization produced during fragmentation and nucleon pickup reactions has proven to be an important means for extending magnetic moment measurements further from stability. Success has been realized in improving the reach for such measurements, as shown in Fig. 2.5.

2.2 β Decay

Another requirement of the β-NMR technique is that the nucleus of interest decays via the spontaneous emission of an electron (β^-) or a positron (β^+), a process known as β decay, and that the asymmetry parameter A_β associated with this decay not be zero. During β^- decay, a neutron is transformed into a proton, while in β^+ decay, a proton is transformed into a neutron. The general form of β decay of a parent nucleus ${}^A Z$ can be written as:

$$ {}^A Z_N \rightarrow {}^A (Z+1)^+_{N-1} + \mathrm{e}^- + \bar{\nu}_e + Q_{\beta-} \qquad \beta^-\text{decay} \tag{2.4} $$

$$ {}^A Z_N \rightarrow {}^A (Z-1)^-_{N+1} + \mathrm{e}^+ + \nu_e + Q_{\beta+} \qquad \beta^+\text{decay} \tag{2.5} $$

where the Q value describes the energy released during the nuclear reaction:

$$ Q_{\beta-} = M[{}^A Z] - M[{}^A (Z+1)] \tag{2.6} $$

$$ Q_{\beta+} = M[{}^A Z] - (M[{}^A (Z-1)] + 2 m_e c^2) \tag{2.7} $$

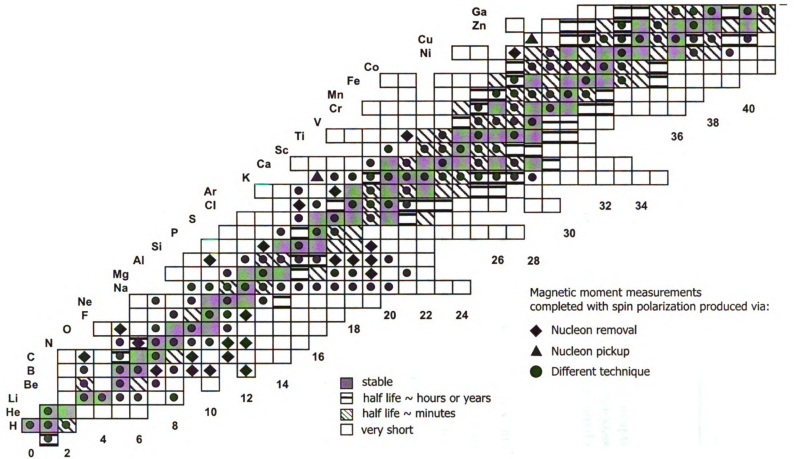

Figure 2.5: Magnetic moment measurements performed with various means of producing spin polarization.

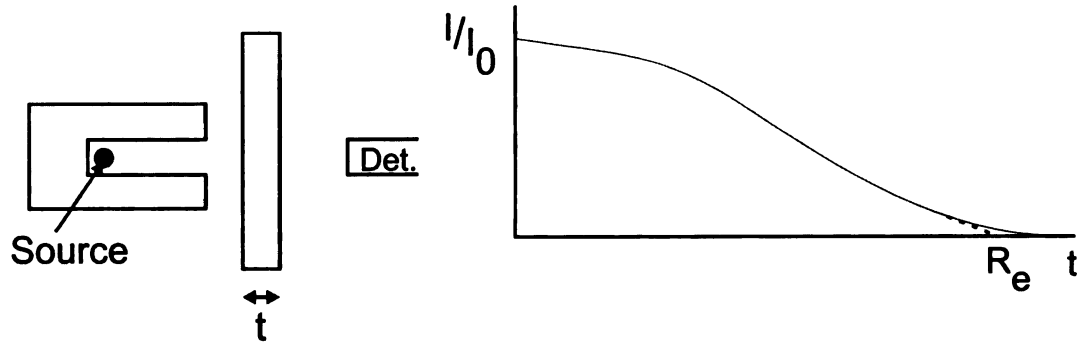

Figure 2.6: Transmission experiment for monoenergetic electrons, adapted from Ref. [57]. I is the detected number of electrons through an absorber thickness t, whereas I_0 is the number detected without the absorber. R_e is the extrapolated range.

2.2.1 Electron interactions

When the electron that is emitted from β-decaying nucleus passes through an absorbing material, such as a detector, the electron does not follow a straight path. Large deviations in the electron path are possible because its mass is equal to that of the orbital electrons with which it is interacting, and a large fraction of its energy can be lost in a single encounter [57]. In addition, electron-nuclear interactions can abruptly change the electron direction. The transmission curve for monoenergic electrons is shown in Fig. 2.6. Even small values of the absorber thickness lead to the loss of some electrons from the detected beam because scattering of the electron effectively removes it from the flux striking the detector. Therefore, the plot begins to drop immediately and gradually approaches zero for large absorber thicknesses. Those electrons that penetrate the greatest absorber thickness will be the ones whose initial direction has changed least in their path through the absorber. Range is therefore not a clearly defined concept for electrons because the electron total path length is considerably greater than the distance of penetration along the initial velocity vector. Normally, the electron range is taken from an extrapolation of the linear portion of the transmission curve to zero and represents the absorber thickness required to ensure that almost no electrons can penetrate the entire thickness.

The continuous distribution of energy from a β-emitting nucleus causes the trans-

mission curve to differ from that of monoenergetic electrons. The low-energy β particles are rapidly absorbed even in small thicknesses of the absorber, so that the initial slope on the attenuation curve is much greater. The transmission curve for β-emitting nuclei is nearly exponential in shape, although the behavior is only an empirical approximation.

The tracks of positrons in an absorber are similar to those of normal negative electrons, and their energy loss and range are about the same for equal initial energies. Coulomb forces are present for both positive and negative charges, and whether the interaction involves a repulsive or attractive force between the incident particle and orbital electron, the impulse and energy transfer for particles of equal mass are about the same.

2.2.2 β-decay angular distribution

β decay is governed by the parity-violating weak force, and the direction of emitted β particles can be anisotropic under certain conditions. The angular distribution of β particles emitted from a polarized nucleus is given [42,43] as

$$W(\theta) = 1 + A_\beta P \cos\theta, \tag{2.8}$$

where θ denotes the emission angle with respect to the axis of polarization, P, as defined previously. The asymmetry parameter A_β for allowed β transitions is

$$A_\beta = \frac{\pm\lambda\rho^2 - 2\rho\sqrt{\frac{J}{J+1}}\delta_{JJ'}}{1+\rho^2} \tag{2.9}$$

where

$$\lambda = \begin{cases} 1 & \text{for } J \to J' = J-1 \\ 1/(J+1) & \text{for } J \to J' = J \\ -J/(J+1) & \text{for } J \to J' = J+1. \end{cases} \tag{2.10}$$

ρ is the mixing ratio defined by the constant $\rho = (C_A\langle\sigma\rangle)/(C_V\langle 1\rangle)$ where C_V and C_A are the Fermi and the Gamow-Teller coupling constants, respectively, and $\langle 1\rangle$ and $\langle\sigma\rangle$ are the corresponding nuclear matrix elements. The upper and lower signs correspond to β^+ decay and β^- decay, respectively.

The β-NMR measurement requires such angular anisotropy of the emitted β particles, and the anisotropy also permits measurement of spin polarization. If the nucleus of interest has some spin polarization, then the β particles will be emitted asymmetrically as given by Eq. 2.8, under the condition that $A_\beta \neq 0$. When the spin polarization of the nucleus of interest is zero, the β particles are emitted isotropically. Thus, the angular distribution can be used as a probe for measuring both spin polarization and the magnetic moment, as outlined in the following two sections.

2.3 Measuring spin polarization

The magnitude of spin polarization may be deduced from the results of a successful β-NMR measurement, as will be described in more detail in the following section. However, it is useful to know the spin polarization for the nucleus of interest prior to the start of a β-NMR measurement. The spin polarization depends on the fragment momentum, as described in the previous section. Therefore, it is desireable to optimize spin polarization as a function of momentum according to the figure of merit, P^2Y, before the β-NMR measurement. Also, a spin polarization measurement that deduces the magnitude of spin polarization as well as direction is ideal, to compare to the magnitude and direction of the NMR effect observed in the β-NMR measurement.

A technique has been developed at NSCL to measure polarization using a pulsed external magnetic field. The technique does not require advanced knowledge of the nuclide's magnetic moment [44]. The β angular distribution will be anisotropic if the implanted nuclei have some spin polarization when the external magnetic field is on. When the magnetic field is off, quadrupolar interactions between the implanted

nucleus and electrons in the lattice will generally dominate the local field interaction at the location of the impurity in a face-centered cubic host material. These quadrupolar interactions will, in effect, depolarize the nuclear spin system and lead to an isotropic β angular distribution. The angular distribution shows maximum deviation at angles 0° and 180° relative to the spin polarization axis, as shown in Eq. 2.8. Therefore, the double ratio

$$R = \frac{[W(0°)/W(180°)]_{\text{field on}}}{[W(0°)/W(180°)]_{\text{field off}}}, \tag{2.11}$$

will deviate from unity when the implanted nuclei are spin polarized, while for unpolarized nuclei R will be unity. Substituting $[W(0°) = W(180°)]_{\text{field off}}$ in Eq. 2.11, the spin polarization can be deduced from R as

$$R = \frac{1 + A_\beta P}{1 - A_\beta P} \tag{2.12}$$

$$R \sim 1 + 2A_\beta P. \tag{2.13}$$

Thus, the spin polarization can be extracted from the experimentally measured quantity R. However, R will also reflect any instrumental asymmetries, for example, the effect of the external magnetic field on the photomultiplier tubes used to detect the β particles. A normalization for the double ratio can be provided by producing the secondary beam at 0° along the incident beam direction to correct for this asymmetry. With the primary beam at 0°, the implanted beam has no spin polarization [45], and β emission will be isotropic. The system asymmetry can be removed from the data by taking a ratio of the double ratios for the polarized (beam angle 2°) and unpolarized (beam angle 0°) sources. The pulsed magnetic field method for measuring spin polarization provides a means of maximizing P^2Y for magnetic moment measurements that use the β-NMR technique, which is described in the following section.

2.4 Nuclear magnetic resonance of β-emitting nuclei

Nuclear magnetic resonance (NMR) is a branch of spectroscopy, and therefore deals with the energy levels of a system and transitions between these levels, either by absorption or emission of photons. β-NMR is a type of radiation-detecting NMR. The sensitivity of β-NMR is about fourteen orders of magnitude greater than conventional NMR. While details of conventional NMR experiments will not be discussed, the detection step involves measurement of a small electrical signal. More than 10^{17} nuclei are needed to obtain a large enough signal above noise. The β-NMR technique involves the detection of β particles emitted from radioactive nuclei, which produce a large electrical signal in the detectors. It has been found that only about 10^3 nuclei are needed in the β-NMR technique. The details of the β-NMR technique are described in the remainder of this section.

As mentioned previously, NMR spectroscopy depends on the interaction between the magnetic dipole moment $\vec{\mu} = g\mu_N I$ and an external magnetic field $\vec{H_0}$, which is defined along the z-axis. The Hamiltonian describing the interaction is given by

$$H = -\vec{\mu} \cdot \vec{H_0} \tag{2.14}$$

$$= -g\mu_N H_0 m \text{ where } m = I, I-1, \cdots -I. \tag{2.15}$$

The interaction induces a splitting in energy known as Zeeman splitting between the formerly degenerate magnetic sublevels (see Fig. 2.7).

When the frequency of the oscillating magnetic field in a resonance experiment corresponds to the separation of neighboring levels, transitions between adjacent substates (selection rule $\Delta m = \pm 1$) are induced by this field. Provided that the static field H_0 is sufficiently uniform and that no electric field gradients are present in the vicinity of the nuclei being studied, the separation between all neighboring levels will be the same, and transitions induced between adjacent levels will have a common resonance frequency. The energy levels E_m and their separation ΔE in such a case

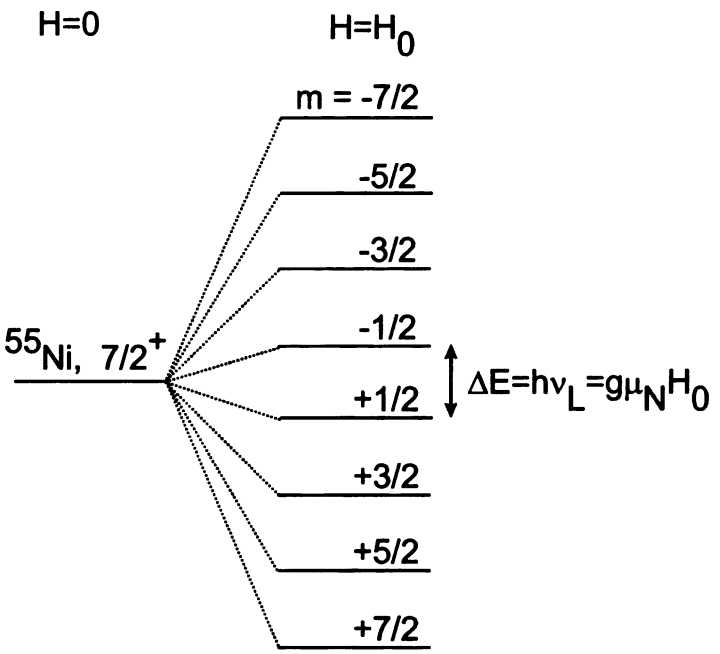

Figure 2.7: Zeeman levels of the ^{55}Ni nucleus in the presence of an external magnetic field.

are given by

$$E_m = -g\mu_N H_0 m \text{ where } m = I, I-1, \cdots -I, \text{ and} \tag{2.16}$$

$$\Delta E = g\mu_N H_0 = h\nu_L \tag{2.17}$$

where ν_L is the Larmor precession frequency. The value of ν_L for $g \sim 1$ and $H_0 \sim 0.5$ generally falls in the radiofrequency (rf) region.

The populations among Zeeman sublevels will be asymmetric after any of the various techniques described previously have been applied. The β-angular distribution from a polarized nucleus shows a maximum deviation at angles 0° and 180° relative to the spin polarization axis (see Eq. 2.8). Therefore, when the number of β particles are monitored at these angles, an anisotropy is observed as long as the nucleus maintains spin polarization and $A_\beta \neq 0$. Given an initially spin-polarized collection of nuclei, an alternating magnetic field H_1 of the proper radiofrequency ν_L applied perpendicular to H_0 induces transitions between the substates. The H_1 drives transitions with $\Delta m =$

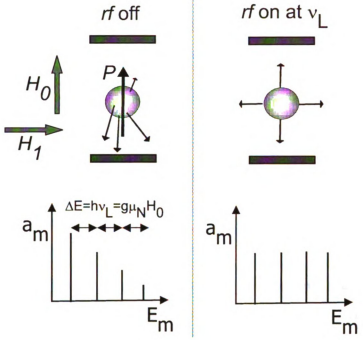

Figure 2.8: Schematic description of the β-NMR technique for an $I = 3/2$ nucleus.

± 1, causing re-distribution of magnetic substate population. If enough *rf* power is applied, the populations may be equalized and the polarization destroyed (see Fig. 2.8). The β-angular distribution is then isotropic.

The *rf* can be applied continuously for a period of time, known as continuous wave (CW) excitation, or it can be applied in short pulses. The ^{55}Ni measurement described in this thesis used the CW technique. The *rf* was scanned using a frequency modulated (FM) signal, while the external magnetic field was held constant. The FM signal allowed for an efficient scan of a frequency region in a short period of time. A wide band FM scan was especially important during the initial search for a resonance. The FM *rf* was applied in a repetitive fashion. The beam was always on and the detectors were always counting. The NMR effect was monitored as the double ratio

$$R = \frac{[W(0°)/W(180°)]_{\text{rf off}}}{[W(0°)/W(180°)]_{\text{rf on}}}. \tag{2.18}$$

When the frequency is off resonance, R is unity, as there is no difference between having the *rf* off or on. At the Larmor frequency, the *rf* off condition results in an asymmetric distribution of β particles, while during the *rf* on phase the β particles are emitted isotropically if polarization is entirely destroyed, as shown in Fig. 2.8. As stated before, at the Larmor frequency, the double ratio reduces to Eq. 2.12. $A_\beta P$ is monitored as a function of applied frequency to determine the Larmor frequency. The g factor is then extracted from the resonance frequency

$$h\nu_L = g\mu_N H_0. \tag{2.19}$$

The μ can be deduced from the nuclear g factor if the nuclear spin is known (Eq. 1.37). The uncertainty in μ is evaluated from the width of the FM signal, which appears as an uncertainty on ν_L. The uncertainty in H_0 is usually small. H_0 was measured in this work with a proton resonance probe to a precision of $1{:}10^4$. Other experimental uncertainties are specific to the nucleus under study and the solid lattice into which it is implanted. In general, for β-NMR experiments, these uncertainties are much smaller than the error in the FM signal, which is typically around 5% for FM= $\pm$25 kHz and $\nu_L = 1$ MHz. The origin of these two uncertainties are described briefly in the following sections, and will be discussed in the context of the ^{55}Ni measurement in the next chapter.

2.4.1 Spin-lattice relaxation

The process of spin-lattice relaxation is the means by which a spin polarized system comes into thermal equilibrium with the surrounding lattice. To conserve energy in the equilibration process, any nuclear Zeeman transition induced by influence of the lattice is accompanied by a compensating change to the lattice. Although there are many contributions to this relaxation, it is generally convenient to use a characteristic time constant to describe the total process, called the spin-lattice relaxation time T_1.

A successful β-NMR experiment clearly requires the spin-lattice relaxation time to exceed the nuclear lifetime, so that the spin polarization is maintained until the nucleus decays.

The spin-lattice relaxation time depends sensitively on the nuclear implantation site and any local radiation damage caused by the implantation process. If the neighboring nuclei in the lattice have non-zero spins, they will change the local magnetic field that the nucleus of interest experiences, and contribute to the relaxation process. In addition, the interactions of the nucleus with electrons in the lattice also cause relaxation. The contribution and nature of the interaction of the nucleus with electrons differs depending on whether the lattice is a metal or insulator.

In metals, the interaction between the nuclear moment and the magnetic field produced by conduction electrons is the dominant spin-lattice relaxation mechanism. The interaction process can be viewed as a scattering process, in which a conduction electron scatters from an initial to a final state, while the nucleus undergoes transition from one magnetic substate to another. The interaction is governed by a potential V which describes the "scattering". Calculations of this type yield what is called the Korringa relation [46], and leads to the following approximate result,

$$T_1 \left(\frac{\Delta H}{H}\right)^2 = \frac{\hbar}{4\pi k T} \frac{\gamma_e^2}{\gamma_n^2}, \tag{2.20}$$

where γ_e and γ_n are the spin g factors for the electron and the nucleus, respectively, and $(\frac{\Delta H}{H})$ is the Knight shift [47]. The Knight shift arises from the difference in the magnetic field produced by the conduction electrons (ΔH) and the external field (H). Note that T_1 is proportional to the inverse of the lattice temperature T. Low temperatures can be employed to lengthen T_1 and extend the time window to evaluate nuclear spin polarization.

The absence of conduction electrons in insulators makes the character of coupling between nuclei and electrons different, and there is no simple relationship between

T_1 and T, as was the case for metals. One source for relaxation in insulators arises from the coupling of the nucleus to the magnetic field produced by the electrons precessing under the influence of H_0. Additionally, a nucleus can indirectly couple with its neighbors via the distortions in the electron shells produced by their magnetic moments, but for rare isotope experiments, the dilute nature of the impurity makes such effect unlikely. In general, typical T_1 for a metal in metal is on the order of ms, while a metal in insulator has a T_1 greater than seconds. It should be noted that the spin relaxation time does not contribute to the error on μ, but remains an important experimental consideration.

2.4.2 Line broadening

Resonance line broadening is characterized by a spread in ν_L for nuclei residing at various sites within the implantation crystal. Provided that the external magnetic field is homogeneous, broadening arises from the local environmental effects surrounding the nuclei. Sources contributing to the overall shape of the resonance line are numerous and can make the shape quite complicated. A common method used to take into account the distribution of interactions with different strengths, directions, and symmetries is the two-site model [48]. It is assumed that a fraction f of the nuclei experience the full local field of undisturbed substitutional sites whereas the rest $(1 - f)$ is not oriented. The latter fraction accounts for nuclei which experience hyperfine fields of different strengths but no preferred direction in space as may be present for instance in a nonmetallic material. For this model the anisotropy is simply $R^{\text{eff}} = fR(\nu_{\text{hf}})$, where $R(\nu_{\text{hf}})$ is the anisotropy expected for the undisturbed substitutional frequency ν_{hf} (or a narrow distribution around it) and R^{eff} is the experimental anisotropy.

In metals, the dominent broadening effect comes from the existence of couplings between neighboring spins, known as dipolar broadening, and is on the order of a few kHz or less. The interaction between two nuclear spins depends on the magnitude and orientation of their magnetic moments and also on their separation [49]. In addition,

spin-lattice relaxation processes place a lifetime limit on the Zeeman levels, which effectively broadens the line by the order of $\hbar T_1$.

The effects described above for metals are small for insulators if the insulator is a perfect crystal. Imperfections in the crystal create, at the position of a nucleus, quadrupole gradients. These quadrupolar effects vary not only in orientation but also in magnitude from site to site and have a considerable influence on the shape of the resonance line. The imperfections in the crystal can be created by dislocations, strains, vacancies, foreign atoms, and/or radiation damage, and the amount of broadening depends on the goodness of the crystal. Most of these effects are expected to be small for β-NMR spectroscopy on rare isotopes.

In this chapter, the necessary components of a β-NMR measurement were introduced including the production of nuclear spin polarization, the β-decay angular distribution, a method to measure spin polarization, and a description of the β-NMR technique. In the next chapter, detailed information is given of the experimental setup that was necessary for carrying out the techniques described previously.

Chapter 3

Experimental Setup

In the previous chapter, the techniques required for a successful magnetic moment measurement using β-NMR were described. This chapter will detail the experimental systems required for beam production and the β-NMR measurement on ^{55}Ni at NSCL.

3.1 Nuclide Production

At NSCL, radioactive ion beams are produced by projectile fragmentation, in which a high-energy projectile impinges a stationary target. A large number of fragments, both stable and radioactive, emerge from the target with velocities near the projectile velocity. The purpose of the experiment described in this dissertation was to measure the magnetic moment of ^{55}Ni. ^{55}Ni was produced by neutron removal reaction from a ^{58}Ni projectile on a ^{9}Be target. A solid sample of ^{58}Ni was vaporized and partially ionized in a room temperature electron cyclotron resonance (ECR) ion source (see Fig. 3.1). The $^{58}Ni^{11+}$ primary beam was accelerated to 13.7 MeV/nucleon in the K500 cyclotron, and then injected into the K1200 cyclotron. In the K1200 cyclotron, the ^{58}Ni primary beam was further stripped with a thin carbon foil to a charge state of 27^{+} and accelerated to 160 MeV/nucleon. After exiting the K1200, the primary beam impinged upon on a 610 mg/cm^2 ^{9}Be target, resulting in many fragmentation

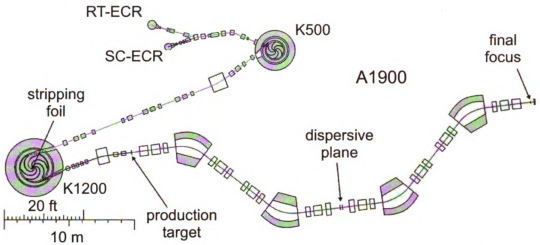

Figure 3.1: Schematic representation of ion source, K500, K1200, and A1900 at NSCL coupled cyclotron facility.

products including ^{55}Ni produced by three neutron removal. The A1900 [50] was used to separate the ^{55}Ni from other reaction products. The first half of the A1900 separated fragments based on magnetic rigidity (momentum/charge), a wedge-shaped degrader at the intermediate image (dispersive plane) induced a velocity shift proportional to the nuclear charge, and finally the second half of the spectrometer separated the desired fragment back into a single spot at the focal plane for transmission to the experimental areas.

The primary beam was set at 2° with respect to the target to break the symmetry of the fragmentation reaction and observe polarization, as shown in Fig. 3.2. Two dipole bending magnets, labeled Z002DH and Z008DS, were used to set the beam angle. A viewer, labeled Z013, located upstream of the target, was used to check the beam position. When the beam was at 0°, the beam spot was located at the center of Z013. At 2°, the beam spot was located to the left of the center position. Polarization of ^{55}Ni was measured at three different momentum settings (-1%, 0%, and +1% relative to the peak of the ^{55}Ni momentum distribution) of the A1900. The full momentum acceptance of the A1900 was kept at $\Delta p/p = 1\%$ via slits at the intermediate image. The magnetic rigidity values of the first two dipole magnets

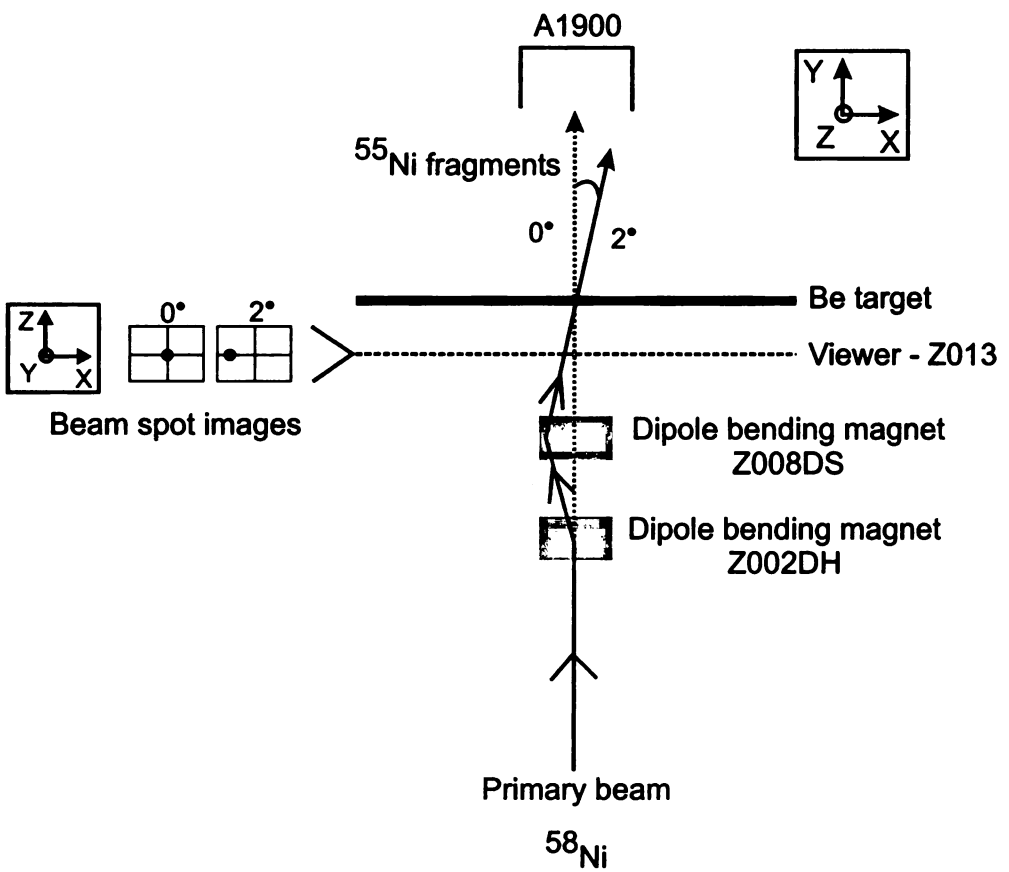

Figure 3.2: Schematic drawing of the placement of the primary beam at a 2° angle on the target.

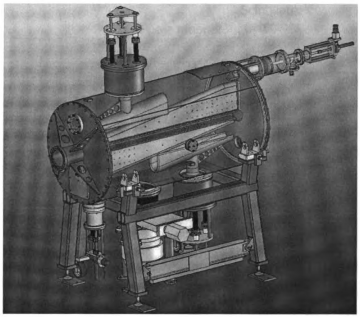

Figure 3.3: Mechanical drawing of the Radio-frequency Fragment Separator. The beam enters the port on the left and a large time-dependent electric field can be applied on the perpendicular axis in phase with the arrival of various particles.

($B\rho_1$) and second two dipole magnets ($B\rho_2$) for each of the three momentum settings are summarized in Table 3.1.

Table 3.1: A1900 $B\rho$ values for the various momentum settings for ^{55}Ni fragments.

Momentum (%)	$B\rho_1$ (Tm)	$B\rho_2$ (Tm)
-1	3.15860	2.67580
0	3.22240	2.76520
+1	3.19050	2.72080

A high beam purity is required for observation of maximum NMR effect due to the continuous nature of the β energy spectrum. The Radio-frequency Fragment Separator (RFFS) [51] was used in conjunction with the A1900 for further purification. A mechanical drawing of the RFFS is shown in Fig. 3.3. The RFFS applied a sinusoidal voltage of $\sim$ 100 kV_{pp} across two copper plates that caused a phase dependent transverse deflection of the beam. The RFFS frequency was operated at the cyclotron frequency of 24.39780 MHz with an adjustable phase difference. The RFFS deflected particles based on time-of-flight, as ions with different velocities arrived at different

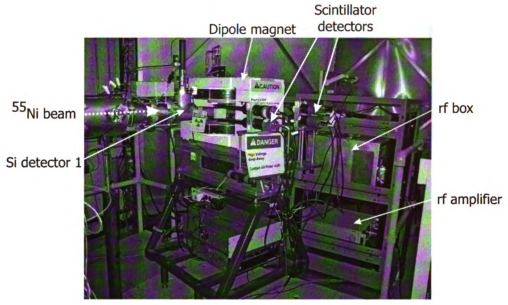

Figure 3.4: Photo of the β-NMR apparatus.

times with respect to the phase of the applied voltage and experienced different transverse angular deflections. An adjustable vertical slit system located 5.38 m after the end of the RFFS allowed for selective removal of unwanted fragments and provided a beam purity of >99% for ^{55}Ni.

3.2 β-NMR Apparatus

3.2.1 Overview

Upon exiting the RFFS, the ^{55}Ni fragments were sent to the β-NMR apparatus [52], pictured in Fig. 3.4. A schematic drawing of the important components is shown in Fig. 3.5. The fragments first passed through a circular collimator, 1.5 cm in diameter, before being implanted into a NaCl single crystal located at the center of the apparatus. The β-NMR apparatus consisted of a large room-temperature dipole magnet with its poles perpendicular to the beam direction with a gap of 10 cm. The magnet induced the required Zeeman hyperfine splitting of the spin-polarized nuclear ground state. The β particles from ^{55}Ni were detected with a set of plastic

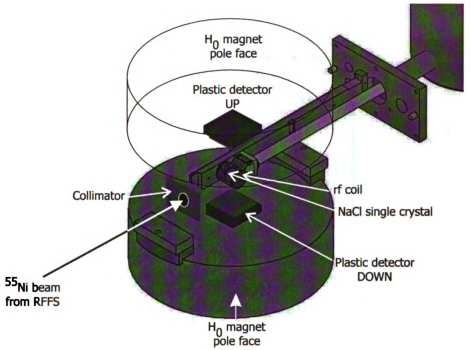

Figure 3.5: Schematic drawing of the β-NMR apparatus. The copper cooling rod was not used as the measurement was performed at room temperature.

scintillator detector telescopes located between the poles of the magnet. One telescope was located at 0° and one at 180°, relative to the direction of H_0. Each telescope contained a thin ΔE scintillator (4.4 cm × 4.4 cm × 3 mm), and a thick E scintillator (5.1 cm × 5.1 cm × 2 cm). Each scintillator was coupled to an acrylic light guide and a photomultiplier tube (PMT). The thick detector acted as a total energy detector for β particles up to 4 MeV. β particles from ^{55}Ni have an endpoint energy of 7.7 MeV with a mean energy of 3.6 MeV (see Fig. 3.6). Only a fraction of the β particles were completely stopped in the thick detector due to the high endpoint energy and scattering effects through the scintillator and surrounding material. The β detectors were labeled as B1 (thick detector on top), B2 (thin detector on top), B3 (thin detector on bottom), and B4 (thick detector on bottom), as shown in Fig. 3.7.

The dipole magnet had a fringe field that affected the performance of the PMTs. The light guides were bent at an angle of 45° to place the PMTs close to the yoke steel (see Fig. 3.7), where the fringe field was smallest. Even when the PMTs were placed

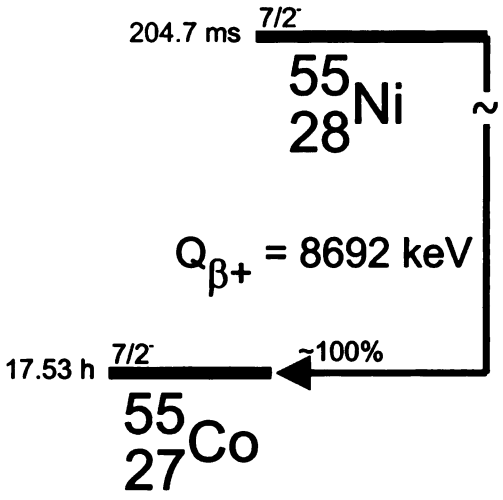

Figure 3.6: β-decay scheme for ^{55}Ni.

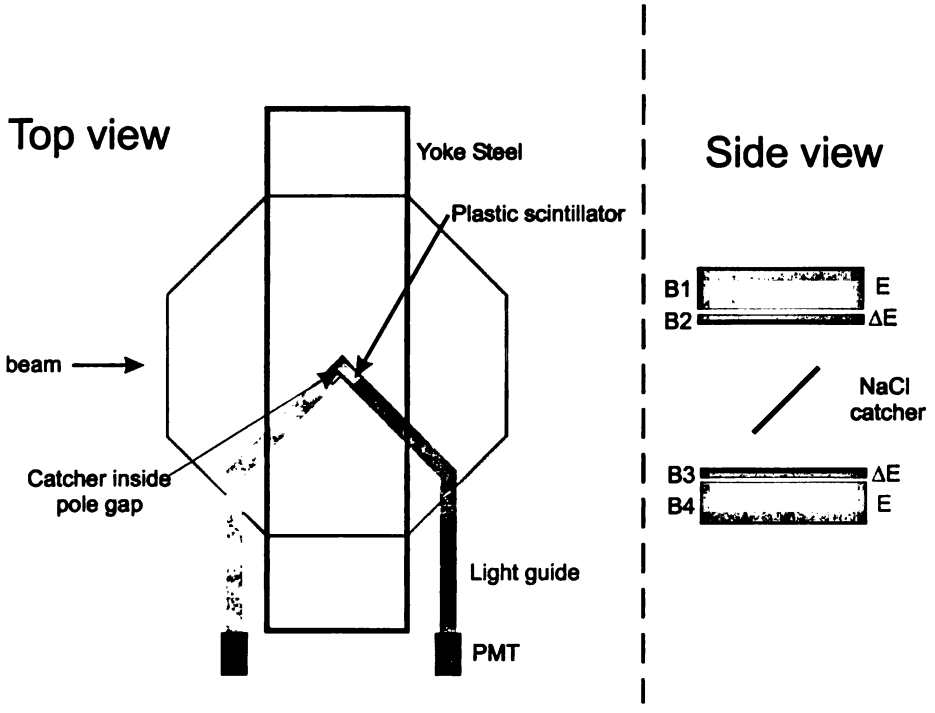

Figure 3.7: Schematic drawing of detector system.

next to the yoke, there remained a fringe field that ranged from 1 to 6 gauss for a magnet current up to 190 A (~0.45-T holding field). A number of different shielding configurations were tested, but none reduced the fringe field significantly. The final configuration included a 0.4-mm thick μ metal sheet rolled into a cylinder and placed around the PMT.

Two silicon surface barrier detectors were used for fragment identification. Silicon detector number 1 (thickness 150 μm) was placed 34 cm upstream of the catcher, and was attached to an air-activated drive, providing the ability to insert and remove the detector from the line of the beam without breaking vacuum. Silicon detector number 2 (thickness 300 μm) was placed 12 cm downstream from the catcher and served as a veto detector for fragments that traveled through the NaCl.

Two identical *rf* coils in a Helmholtz-like geometry were placed within the magnet and between the β detectors, with the field direction perpendicular to both the direction of the beam and the static magnetic field. Details of the *rf* system are given in the next section. A 2.5-cm diameter, 2-mm thick disc-shaped NaCl single crystal was mounted on an insulated holder, between the pair of *rf* coils. The crystal was placed at an angle of 45° relative to the normal beam axis to minimize the energy loss of the β particles emitted at 0° and 180°. A 1.5-mm thick Al degrader was placed in front of the collimator to lower the energy of the incoming ^{55}Ni ions to cause the ions to stop in the center of the NaCl crystal. The LISE++ code [53] was used to calculate the appropriate thickness of the degrader. NaCl was chosen as a catcher because it is known to hold polarization for Cu ions with a long T_1 [23] given that Ni ions have similar atomic radii to Cu ions, however, the T_1 for Ni ions in NaCl is unknown. A photo of the *rf* coil, crystal, collimator, and silicon detector 2, all of which under vacuum during the measurement, is shown in Fig. 3.8.

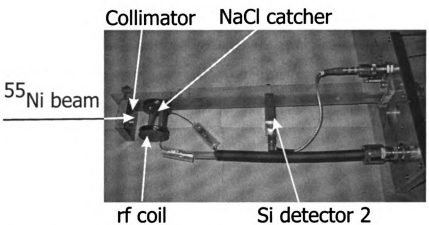

Figure 3.8: Photo of the *rf* coil with crystal, collimator, and silicon detector 2. All of the pictured components are under vacuum during the measurement.

3.2.2 Radiofrequency system

The transverse H_1 field used to destroy the polarization was created by the Helmholz-like coils that made up part of an *LCR* resonance circuit. L is the inductance of the *rf* coil that produces the H_1, C is the capacitance, and R is the resistance. The *LCR* resonance condition for frequency f is given by

$$f = \frac{1}{2\pi\sqrt{LC}}. \tag{3.1}$$

Several variable capacitors were used with fixed L and R to tune the resonance circuit and achieve impedance matching to the *rf* amplifier. Such operation ensured a sufficiently large value of H_1 for all transition frequencies within a frequency modulated (FM) scan. Transition frequencies were sequentially applied to the *LCR* resonance circuit by selecting one of the variable capacitors using fast relay switches. The selected capacitor was tuned to the specific capacitance that satisfied the *LCR* resonance condition for a particular frequency. The basic scheme is shown in Fig. 3.9.

The *rf* system used one of three function generators to generate the FM *rf* signal. A pulse pattern generator, REPIC model RPV071, triggered the function generators. The *rf* signal was sent to a 250 W *rf* amplifier. The amplified signal was then applied

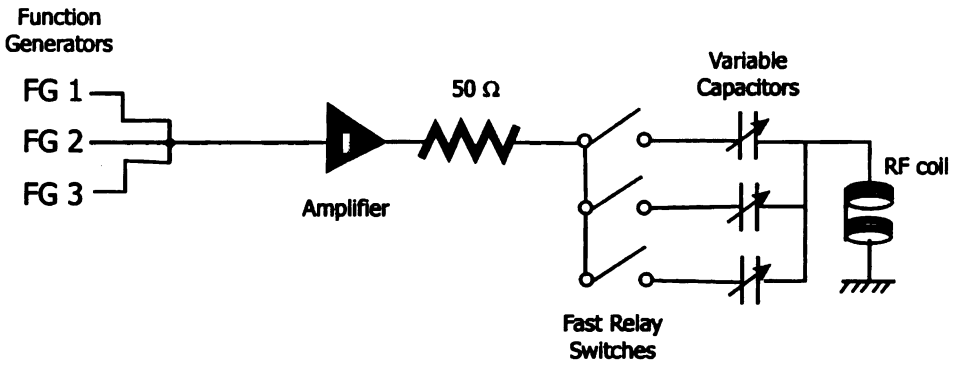

Figure 3.9: Schematic drawing of the LCR resonance system.

to the rf coil, which was part of the LCR resonance circuit. A 50 Ω resistor fulfilled the impedance matching condition between the amplifier and the rf coil. One (or more) of six variable capacitors were used to complete the LCR circuit. The primary capacitor used during the NMR measurement was a 4000 pF variable capacitor. A remotely-controlled stepper motor was used to tune this capacitor. The generated resonance curve is also called a Q curve, and an example is shown later in this section. After a fixed rf irradiation time, the frequency from a second function generator was sent to the same LCR resonance circuit. A different capacitor was then selected by the fast-switching relay system. Only one function generator was used for the majority of the NMR measurements presented in this thesis, as only a single central frequency with FM was applied for any one rf measurement. However, for a portion of the experiment, a new multiple-frequency NMR technique was tested. Three function generators were used to scan a larger frequency region for the initial resonance search. Additional details on the rf system are available in Ref. [54].

The operating parameters for the rf depended on the conditions of the NMR measurement. The theoretical predictions for $\mu(^{55}\mathrm{Ni})$ given in section 1.4.4 suggested a search region for $\mu(^{55}\mathrm{Ni})$ between -0.6 μ_N and -1.2 μ_N. With an external magnetic field of $H_0 = 0.4551$ T, the μ search region corresponded to a frequency range of 588 kHz to 1176 kHz, where $g = \mu/I$ in Eq. 2.16 and $I = 7/2$ for ^{55}Ni. The inductance of the coil and capacitance were chosen according to Eq. 3.1 to match the desired

frequency region. With a fixed inductance of $\sim 15\ \mu H$, the capacitance ranged from 4500 pF for the lowest frequency to 1000 pF for the highest frequency. The capacitors available in the rf system included: one 3900 pF fixed capacitor, two 4000 pF variable capacitors, two 1500 pF variable capacitors, and one 1000 pF variable capacitor.

The rf coil support was made of the polyimide-based polymer Vespel®, made by DuPont™, and rated to 260°C. The copper wire used to wind the coil was 20 AWG (round) with a polyimid insulation called Allex®, ordered from Superior Essex®. The wire insulation was rated to 240°C. Such temperature ratings were sufficient to withstand the heat generated by the voltage drop across the coil. The inductance of the coil was measured as a function of turn number as shown in Fig. 3.10a. The measurement was made with an LCR meter (Electro Science Industries - model 253). The total turn number is the sum of turns for the two coils. The relationship between the inductance and total number of turns, N, followed a $L \sim N^2$ dependence, as shown in Fig. 3.10b. Therefore, to achieve a coil with an inductance of $\sim$15 μH, a 14/14 turn coil was used. The measured inductance of the 14/14 turn coil was 14.3 μH.

The strength of H_1 needed to destroy the initial polarization is given by the expression

$$H_1 = \frac{1}{\gamma}\left(\frac{2\pi\Delta f}{\Delta t}\right)^{1/2}, \tag{3.2}$$

where Δf is the frequency window, Δt is the rf time, and $\gamma = \frac{g}{\hbar}\mu_N$. A FM of $\pm$50 kHz used for the initial wide frequency scan and an rf time of 10 ms required an H_1 field of $\sim$8 G. A FM of $\pm$25 kHz for the narrower scan and an rf time of 10 ms required an H_1 field of $\sim$5 G. Temperature tests proved the rf system could withstand the prolonged application of an H_1 of 8 G, as the temperature was observed to saturate at 155°C.

The DC character of the coil, α, was determined by measuring the magnetic field of the coil as a function of applied current. α is needed to determine H_1 of the coil at

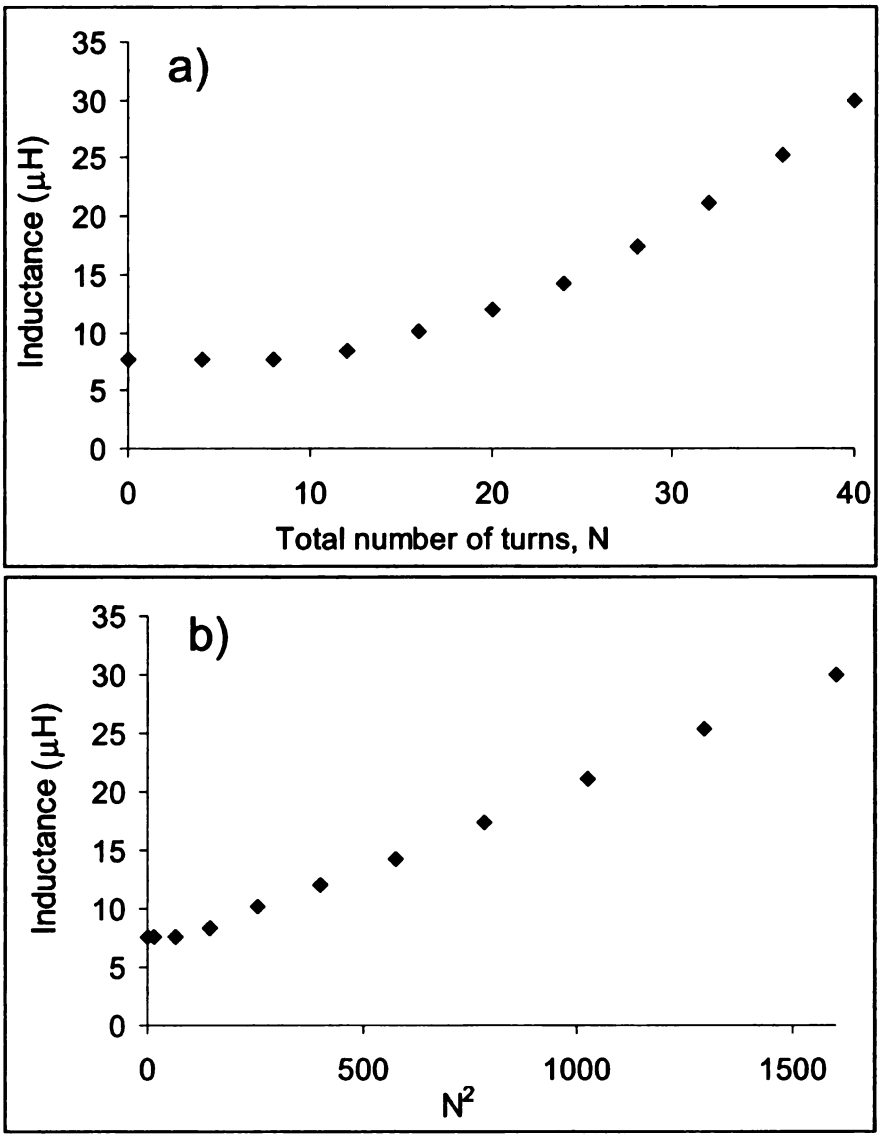

Figure 3.10: Inductance of the *rf* coil as a function of a) total turn number, N and b) N^2.

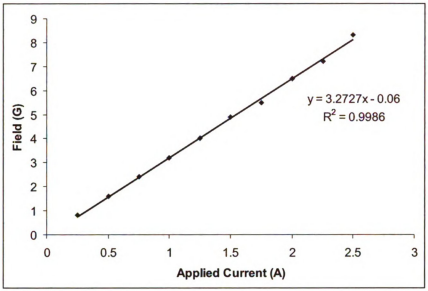

Figure 3.11: DC character of the *rf* coil determined by measuring the magnetic field of the coil as a function of applied current. The α value is equal to the slope of the line.

a given frequency. Current was applied to the *rf* coil using a Tenma Laboratory DC Power Supply (72-6152) from 0 to 2.5 A. The magnetic field was monitored at the center of the coil using a FW Bell Gauss/Teslameter (model 5080) and the results are shown in Fig. 3.11. The α value is the slope of the line, α =3.3 G/A. The H_1 is then calculated as

$$H_1 = \frac{V}{2}\frac{1}{2\pi f L}\frac{\alpha}{2}, \tag{3.3}$$

where V is the voltage across the coil, f is the applied frequency, and L the inductance of the coil. The voltage is determined from the peak-to-peak value on the resonance Q-curve, as shown in Fig. 3.12. The example Q-curve was recorded at frequency 1100 kHz with FM $\pm$ 50 kHz. The input voltage from the function generator (FG) was V_{in} =100 mV_{pp} and the generated voltage was V_{out}=870 V. The calculated H_1 in this case was 7.2 G which matches the required H_1 given by Eq. 3.2.

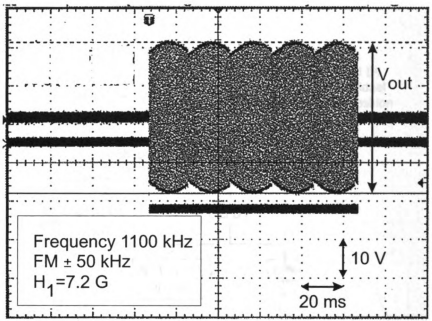

Figure 3.12: Resonance Q-curve at frequency 1100 kHz with FM ± 50 kHz and input voltage V_{in} =100 mV_{pp}. The H_1 is calculated from Eq. 3.3.

3.2.3 Electronics

Readout electronics

The plastic scintillator detectors were used to detect the β particles emitted in the decay of ^{55}Ni. A schematic diagram of the electronics for each of the four plastic scintillators is shown in Fig. 3.13. Each scintillator was coupled to an acrylic light guide, which was coupled to a PMT. The signal from the PMT was shaped, amplified, and separated into a fast signal and a slow signal. The slow signal was sent to a VME analog-to-digital converter (ADC, CAEN mod. V785) where the energy was determined from the maximum voltage peak. The fast timing signal was sent to a constant fraction discriminator (CFD, Tennelec TC 455). One of the fast timing signals from the CFD was converted from NIM type to ECL and used in the VME scaler module (CAEN scaler C3820) for rate monitoring. Another CFD time signal was used for establishing the logic of the master gate (MG).

A schematic diagram of the electronics for the silicon detectors used for particle

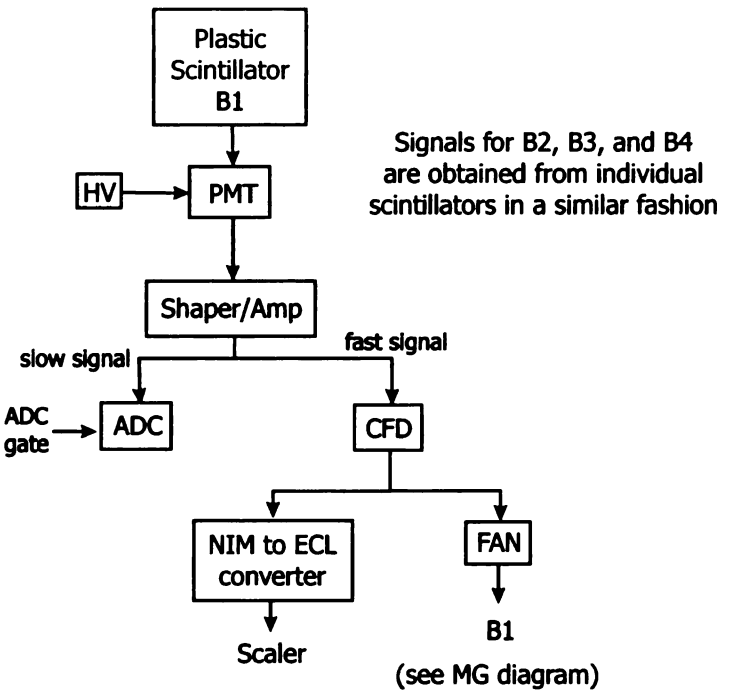

Figure 3.13: Plastic scintillator electronics diagram.

identification is shown in Fig. 3.14. Silicon detector 1 (Ortec SN 27-259B, model TB-020-300-150) was located upstream of the β-NMR apparatus and was used for particle identification. The energy signal was taken from the slow output of the amplifier and digitized in VME. The fast timing signal of Silicon 1 was compared with the cyclotron *rf* to generate a time-of-flight (tof) measurement of the incoming beam. Silicon detector 2 (Ortec SN 36-153D, model TB-020-300-300) was located downstream of the NaCl crystal, and was used for particle identification before the crystal was put in place. After the NaCl crystal was in place, the detector was used as a veto detector for fragments that passed through the NaCl crystal. Signals from both detectors were processed with Tennelec (S/N 2104) preamplifiers, and then amplified (Tennelec TC 241 S). The slow signal was sent to the ADC and the fast signal was sent to the CFD for timing purposes. One of the CFD timing signals for both silicon detectors was sent to a logical OR to become part of the master gate (MG). Another CFD timing signal for both detectors was converted from NIM type to ECL type and sent to the scaler for rate monitoring. As noted above, a third timing signal from the silicon detector 1

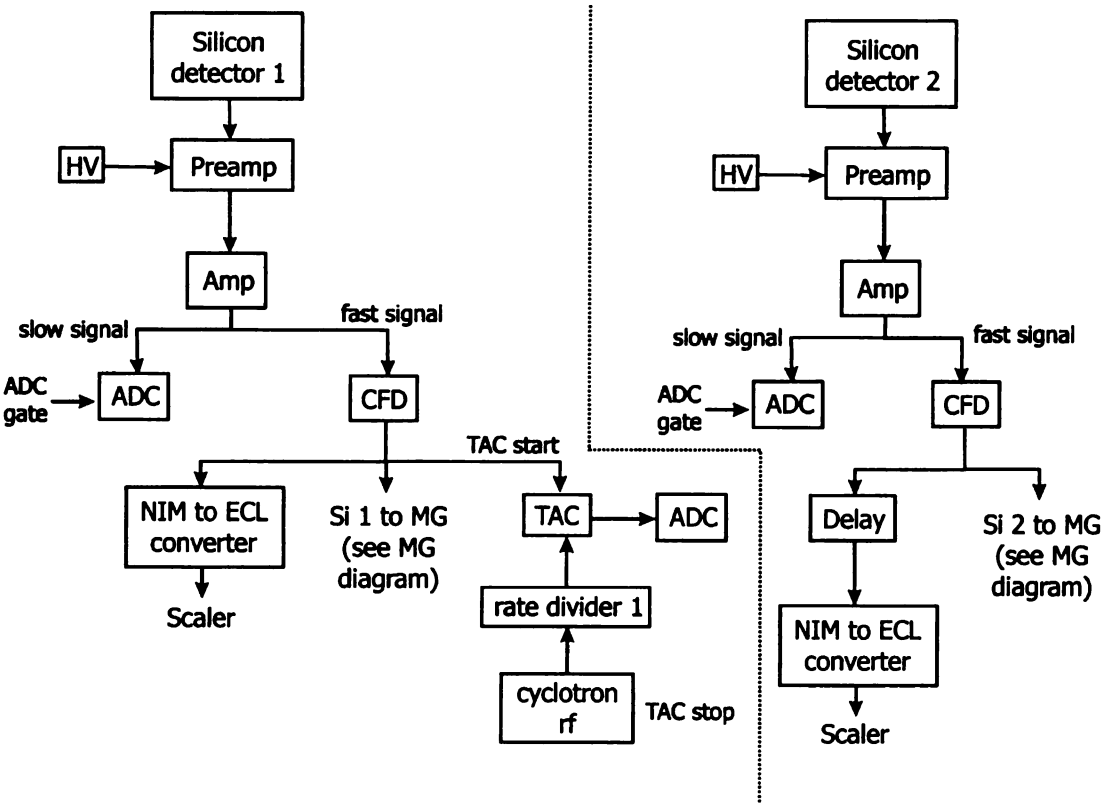

Figure 3.14: Silicon detectors electronics diagram.

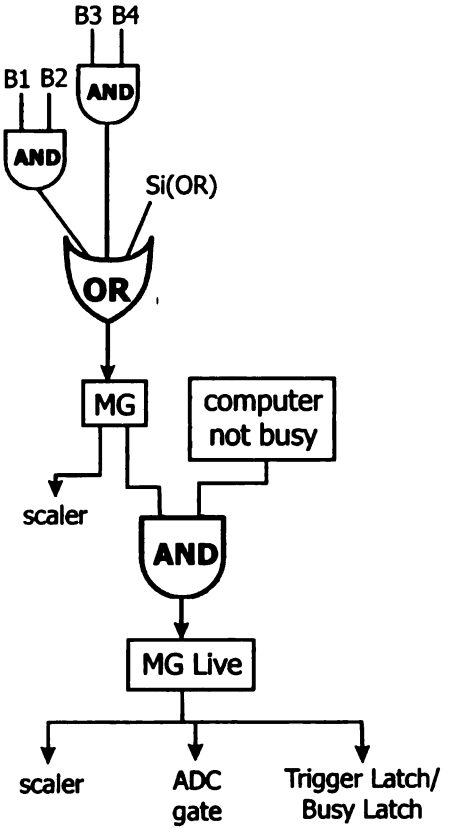

Figure 3.15: Master gate (MG) electronics diagram.

CFD was used as a start for the time-to-amplitude converter (TAC, Ortec 566). The TAC stop came from the K1200 cyclotron *rf*. The TAC output represented the beam tof, and was digitized in VME.

A logical AND was made between B1 and B2, as well as B3 and B4 before being sent to the MG. The coincidence condition was implemented to reduce readout dead time and reduce background events and was used to trigger the readout of all other detectors during the data acquisiton (see Fig. 3.15). The MG was created from the logical OR of scintillator coincidences and the signal from the silicon detectors to trigger during particle identification. The MG made a logical AND with a computer-not-busy signal to provide the master live signal. Master live "opened" the data acquisition gate for ADC conversion.

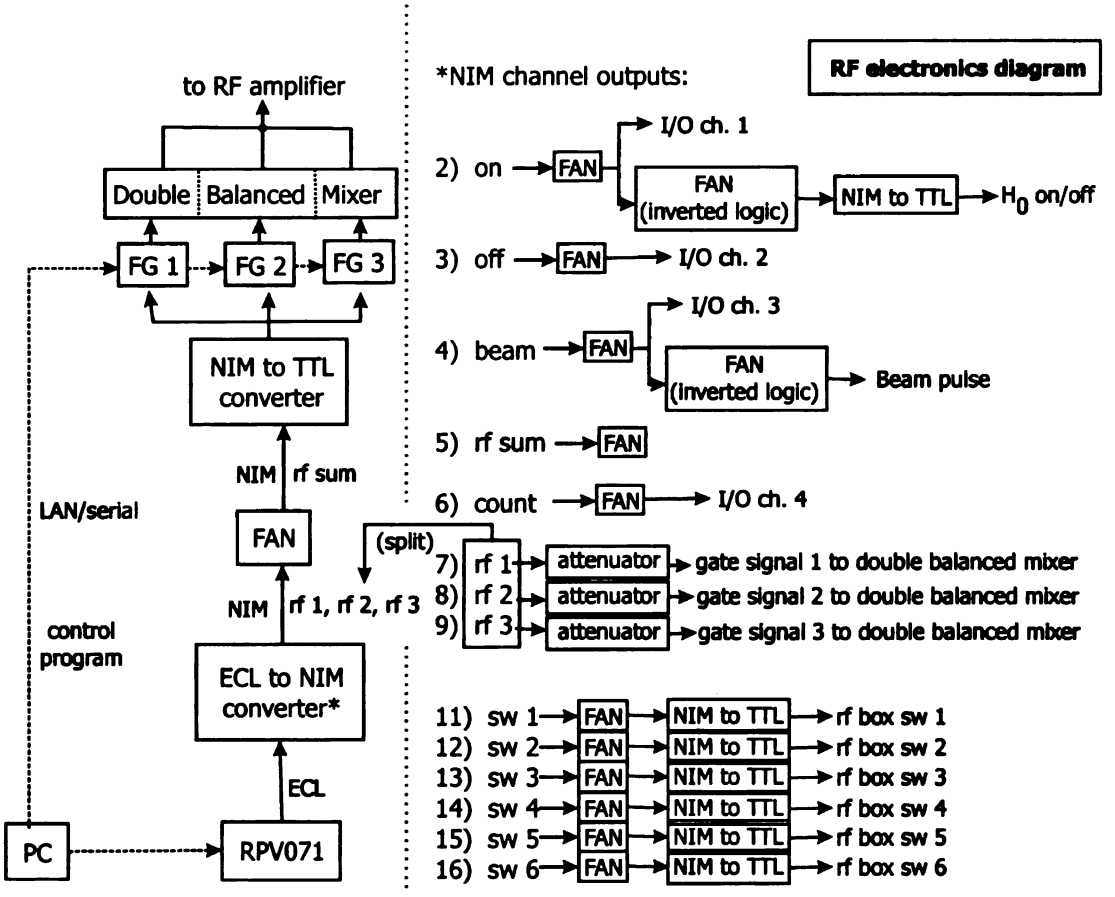

Figure 3.16: Electronics diagram for the radiofrequency system.

rf electronics

Function generators (FG, Agilent function/arbitrary waveform generator, 20 MHz model 33220A) were used to produce the *rf*. Timing control of the *rf* was accomplished with a VME pulse-pattern generator (see Fig. 3.16). The REPIC model RPV-071 pulse-pattern generator had 32 channel output with 65k/channel data memory. A bit pattern was loaded into the memory of the RPV-071 through the VME bus. The pattern was output-synchronized with an external clock signal. Each output was used to trigger and/or gate devices. These devices are listed on the right side of Fig. 3.16. The on, off, beam, and count signals from RPV-071 were sent to an I/O register (CAEN mod. V977) for recording in the data stream and for software gating. The on and off signals were used for *rf* pulsing. The on signal was also sent through TTL

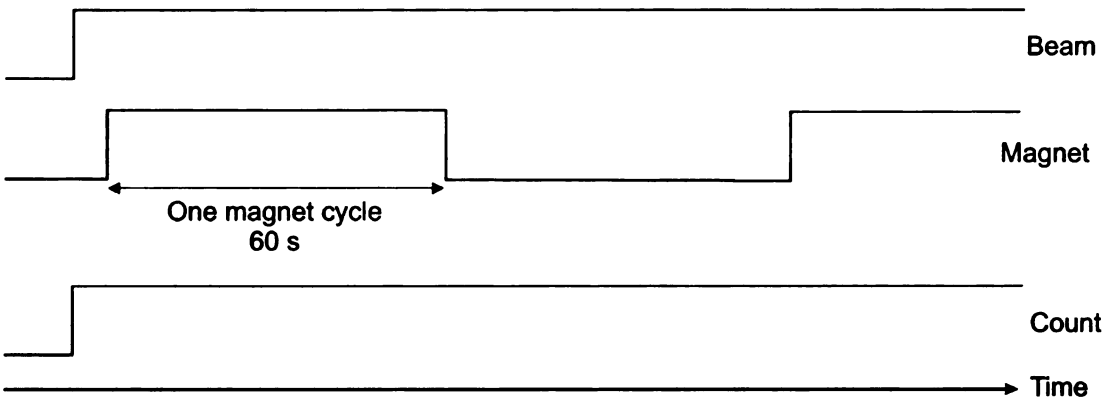

Figure 3.17: Schematic representation of the external magnetic field pulsing sequence during the polarization measurement. The field was pulsed on and off every 60 s. The beam was continously implanted.

to a temperature sensor at the input of the dipole magnet coil to control magnet pulsing. The *rf* pulsing sequence generated by RPV-071 was sent to the function generator. From the function generator, the signal went to the *rf* amplifier (model BBS0D3FOQ, 58 dB, 250 W), and then to the *rf* box. The sw1-6 signals shown in Fig. 3.16 represent the capacitor switch signals, which were generated by RPV-071 and sent to the *rf* box.

The timing sequences programmed to the RPV-071 module for both the polarization measurement and NMR measurement are shown in Figs. 3.17 and 3.18, respectively. In both measurements, the beam was implanted continuously and β counting was performed for the entire measurement. During the polarization measurement, the external magnetic field was pulsed on and off every 60 s. The frequency of the internal clock on the RPV-071 module was 500 Hz, and thus the minimum length of the pulse was 1/(500 Hz)=2 ms. The maximum length of the pulse or one cycle of timing program was (65k data point)/(500 Hz)=130 s.

During the NMR measurement, the FM was realized in a "sawtooth" function with a 10 ms *rf* sweep time. The *rf* was applied continuously for 30 s on and then 30 s off. The RPV-071 clock frequency was 2000 Hz, so the minimum length of the pulse was 0.5 ms. The maximum length of the pulse or one cycle of timing program was 32.5 s. The RPV-071 module was controlled with a graphical user interface developed

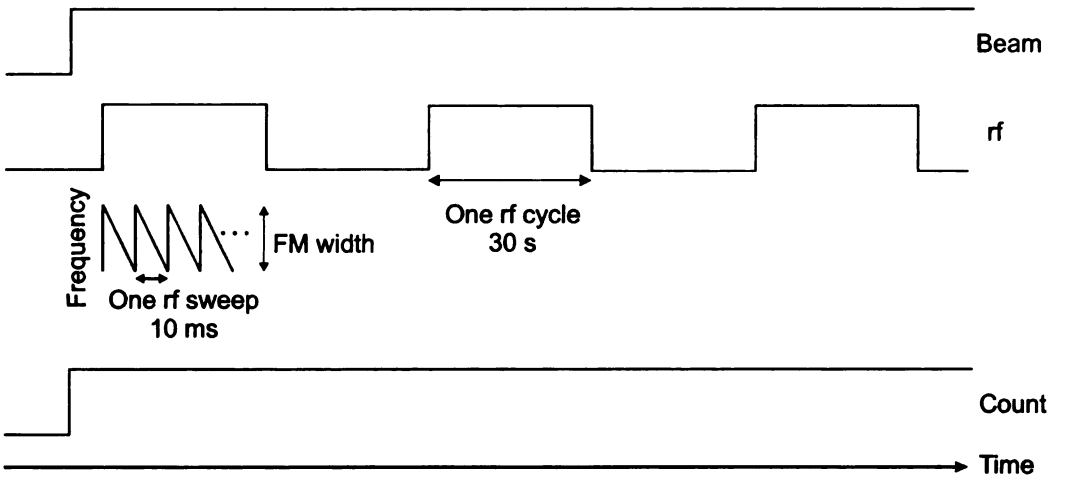

Figure 3.18: Schematic representation of *rf* pulsing sequence during the NMR measurement. The *rf* was pulsed on and off every 30 s, with 20 ms sweep time. The beam was continously implanted.

using Tcl/Tk (scripting language/graphical user interface took kit) [55] based on the NSCLDAQ VME Tcl extension [56].

High voltage (HV) was supplied to each β detector PMT and the silicon detector preamps through a CAEN SY3527 High Voltage Power Supply (HVPS). Individual software controls for voltage ramp rate and maximum voltage were available for each device connected to the CAEN HVPS.

3.2.4 Calibrations

External magnetic field

Precise knowledge of the external magnetic field is necessary to reduce systematic uncertainty in the g-factor result. The g factor is calculated from ν_L and H_0 (Eq. 2.19). The contribution to the overall error on the g factor from the magnetic field can be less than the FM. The dipole magnet field was calibrated by measuring the static field at the center of the *rf* coil as a function of applied current. The magnetic field was measured using the Metrolab PT2025 precision NMR Teslameter with a number 3 solid sample ^{1}H probe (range 0.17 to 0.52 T). Current was supplied to

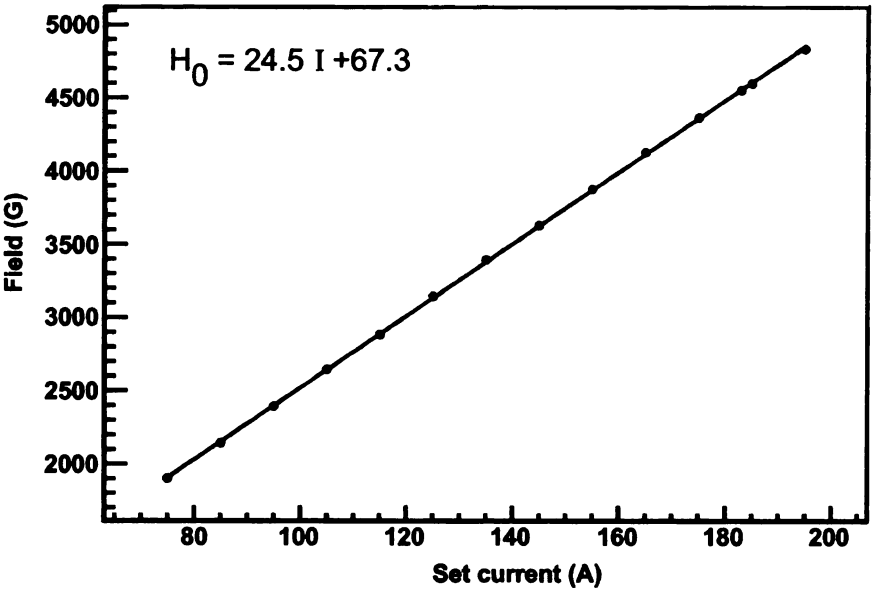

Figure 3.19: Dipole magnet calibration.

the magnet with a Power Ten Inc DC power supply (SN 1010740). The calibration was done with all experimental devices in place, except for the NaCl crystal and silicon detector 2, which would have been in the way of the probe. The calibration of the holding field as a function of applied current is shown in Fig. 3.19. The magnet calibration was done approximately a month before the experiment began to establish the dependence of the field with the applied current. However, for the experiment, it is only important that the field is known *precisely* at the set current, and that the field is stable for the duration of the β-NMR measurement. The field was also monitored immediately before and after the experiment, for one hour to obtain an estimate of the systematic error on H_0. The β-NMR measurement was conducted with a current of 180 A, corresponding to 4477.3 G using the calibration. Over the course of a month period, however, the field shifted. When the field was measured at 180 A prior to the experiment, the field ranged from 4490.6 G to 4494.3 G over one hour. Immediately after the experiment, the field was monitored again for one hour at 180 A and ranged from 4490.0 G to 4491.5 G. The fluctuation in magnetic field mainly came from two sources: inherent instability of the power supply and

temperature. The power supply has a quoted stability of $\pm 0.05\%$ of the set point per 8 hours after warm-up. Variations in the temperature of the room affect the power supply and in turn the magnetic field. A value of 4490.5 G was chosen with an error of 5.0 G at 180 A to take into account the small fluctuations in field over the course of the experiment.

The magnetic field strength chosen for the polarization measurement was 1000 G, which corresponds to 40 A of current in the magnet. In the polarization measurement, the magnetic field is pulsed on and off. The PMTs are affected by the fringe field of the magnet, and this effect is field dependent, as shown in Fig. 3.20, where the energy spectra for B1 and B4 are shown for a ^{90}Sr source as a function of applied current. Therefore, 40 A (1000 G) was chosen as a field strength for the polarization measurement, where the field effects were minimal (see Fig. 3.20).

Plastic scintillator detectors

Ideally, the plastic scintillator detectors would be calibrated with β particles of varying energy. However, there are limited off-line or long-lived sources of β particles with a large endpoint energy. One alternative is to calibrate the energy response with the Compton edge from a γ-ray source, since the scintillators are able to detect the scattered electrons. The accuracy of such a calibration is not high, but is sufficient to check the functionality of the detector.

A Compton scatter results in the creation of a recoil electron and scattered γ-ray photon, with the division of energy between the two dependent on the scattering angle [57]. The energy of the scattered γ ray, E'_γ, in terms of its scattering angle θ and the initial γ energy, E_γ, is given by

$$E'_\gamma = \frac{E_\gamma}{1 + (E_\gamma / m_0 c^2)(1 - \cos\theta)}, \tag{3.4}$$

where $m_0 c^2$ is the rest mass energy of the electron (0.511 MeV). The Compton edge

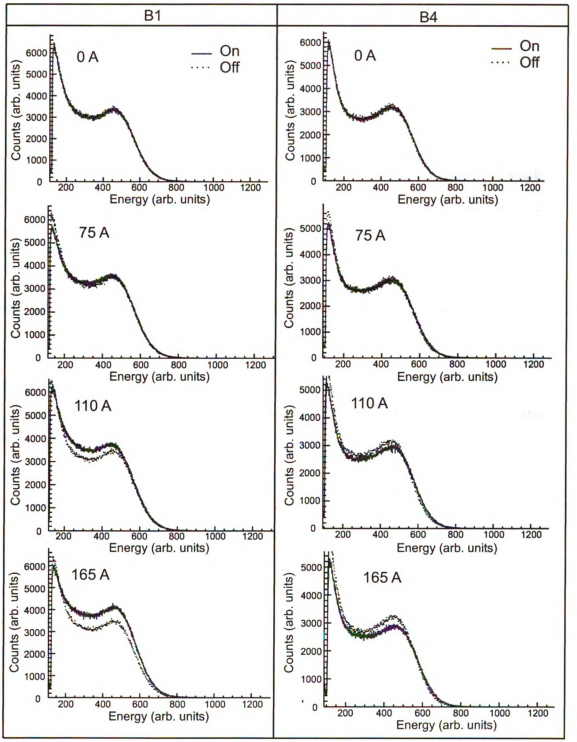

Figure 3.20: Dependence of the β energy spectra for a ^{90}Sr source on the strength of the external magnetic field. Energy spectra of thick detectors B1 and B4 are shown with magnetic field off (dotted line) and magnetic field on (solid line) at 0, 75, 110, and 165 A.

Table 3.2: Peak γ energy and calculated Compton edge for each source used in the plastic scintillator energy calibration.

Source	Peak γ energy (keV)	Compton edge (keV)
^{57}Co	122	40
^{137}Cs	662	481
^{60}Co	1170	964
	1330	1120

represents the maximum energy that can be transferred to an electron in a single Compton interaction, that is, in a head-on collision in which $\theta \simeq \pi$. In this case, Eq. 3.4 reduces to

$$E'_\gamma \simeq \frac{E_\gamma}{1+4E_\gamma}, \tag{3.5}$$

and the Compton edge, E_C, is the maximum energy transferred to the electron, that is

$$E_C = E_\gamma - E'_\gamma. \tag{3.6}$$

Three γ sources were used to energy calibrate the β telescopes: ^{57}Co, ^{137}Cs, and ^{60}Co. The γ peak energy and calculated Compton edge for each source are shown in Table 3.2. An average was taken for the two ^{60}Co values, as the separate Compton edges are not resolved in the plastic scintillator. The Compton edge was determined in the spectrum by taking the channel value at the half maximum of the Compton continuum for each detector. An example of the determination of the Compton edge from the energy spectrum taken with a ^{137}Cs source with B1 is shown Fig. 3.21. This channel number is shown as a function of the calculated Compton edge in Fig. 3.22.

The linear trend shows that the detectors are functioning as expected. The absolute values obtained from the calibration may not be accurate, as it was difficult to determine the location of the Compton edge from the spectra due to the scattering and energy loss properties of electrons discussed in section 2.2.1. Such properties are also the reason for the difference in the slope of the line for thick detectors versus thin detectors.

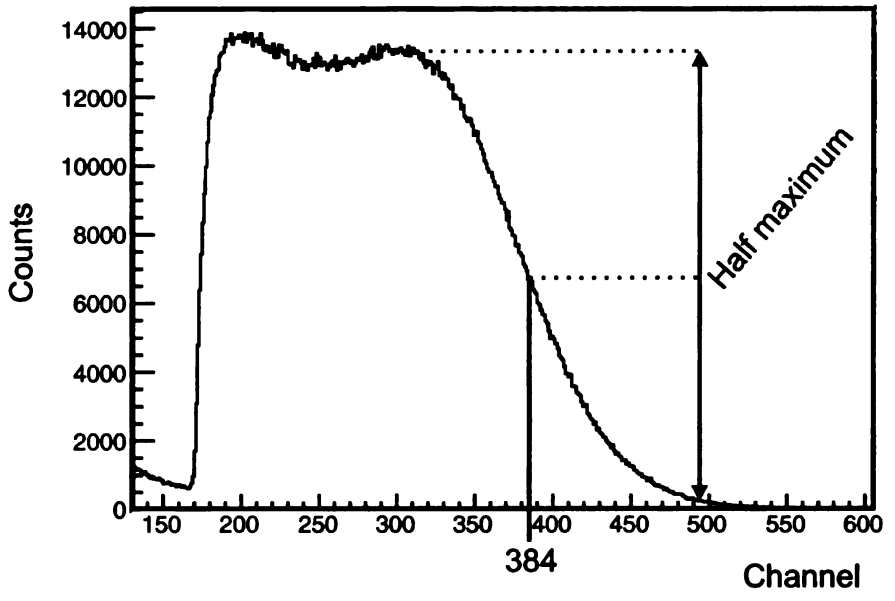

Figure 3.21: Energy spectrum from ^{137}Cs taken with B1 to determine the Compton edge. The Compton edge was determined in the spectrum by taking the channel value at the half maximum of the Compton continuum.

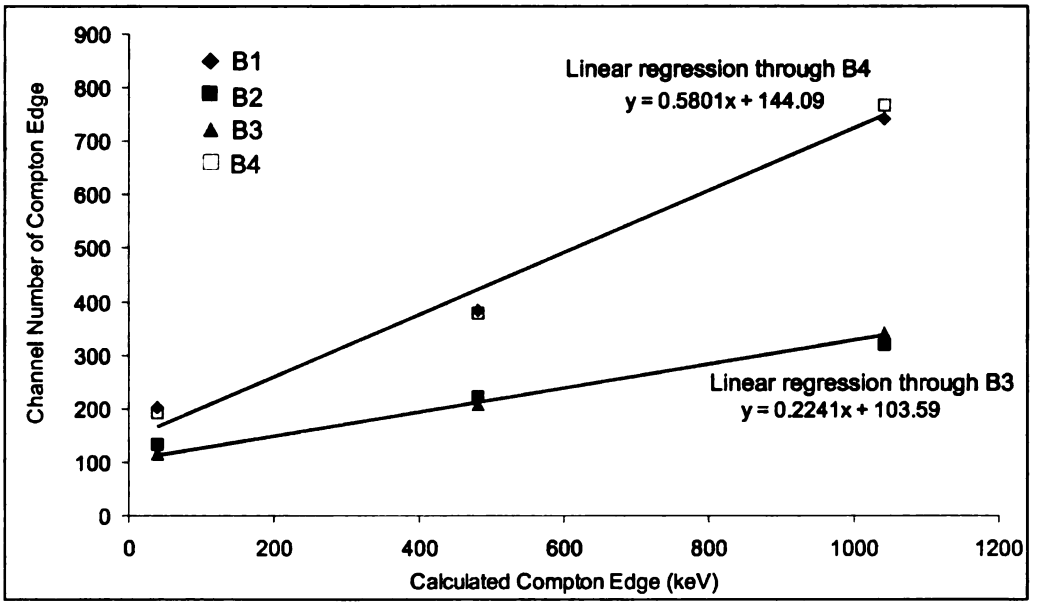

Figure 3.22: Energy calibration of plastic scintillator detectors B1-B4. ^{57}Co, ^{137}Cs, and ^{60}Co were used as γ sources and the calibration was done using the Compton edge of the γ spectrum.

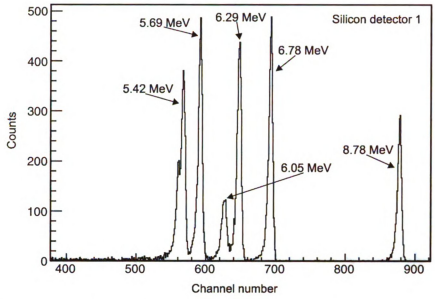

Figure 3.23: α-decay spectrum of ^{228}Th collected with silicon detector 1.

Silicon detectors

The silicon detectors were tested prior to the experiment to check the energy resolution. Silicon detector 1, placed upstream of the β-NMR apparatus on an air activated drive, was the primary detector used for particle identification at the experimental end station. Silicon detector 2, placed downstream of the NaCl crystal, was used to determine if fragments were passing through the crystal. Both detectors were tested by collecting an α spectrum from a ^{228}Th source, with the results shown in Figs. 3.23 and 3.24. The observed resolution was sufficient for particle identification purposes in the ^{55}Ni region. The FWHM at 5.69 MeV was observed to be 64.8 keV for silicon detector 1 and 76.5 keV for silicon detector 2. The silicon detectors were also tested with the external magnetic field on at both 180 A and 40 A, with little change in energy resolution.

β-NMR apparatus

The entire β-NMR apparatus was calibrated to ensure that there were no inherent asymmetries. The same *rf* sequences executed during the experiment were also per-

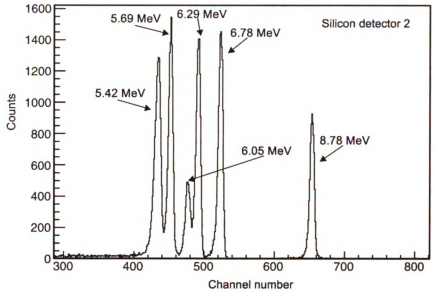

Figure 3.24: α-decay spectrum of ^{228}Th collected with silicon detector 2.

formed with a ^{60}Co γ source at the crystal position. Calibration with a β source would again be ideal, as was the case for the plastic scintillator calibration, but the selection of β sources is limited. The available β source, ^{90}Sr, β^- decays to ^{90}Y with a Q value of 546 keV (mean β energy 196 keV). ^{90}Y then β^- decays to ^{90}Zr with a Q value of 2.3 MeV (mean β energy 933 keV). Most β particles from this source would be absorbed before making it to the thick detector for a coincidence measurement. Some β particles make it through to the thick detector, but the activity of the source was not sufficient to complete the necessary calibrations in a reasonable amount of time. Thus, a γ source was thought to be the best available option. Prior to the experiment, the frequency range of 600 kHz to 1600 kHz was scanned, pulsing the *rf* on and off every 30 s, with a constant external magnetic field of 4490.5 G. The double ratio R was determined as given in Eq. 2.18. Two frequency modulations were applied, the first at $\pm$ 50 kHz, and the second at $\pm$ 25 kHz, to reproduce the expected experimental conditions. Both calibrations are shown in Fig. 3.25 and no significant asymmetry was apparant.

The H_0 on/off double ratio was also determined with the ^{60}Co source. The dipole

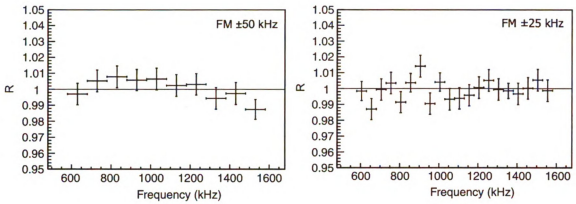

Figure 3.25: *rf* calibration prior to the start of the experiment with ^{60}Co source. The *rf* is pulsed 30 s on then 30 s off. Two frequency modulations (FM) were checked: ±50 kHz and ±25 kHz.

magnet was pulsed on and off every 60 s, at a field of 1000 G. The double ratio R was taken as given in Eq. 2.11. The calibration value of R was found to be 1.0012 ± 0.0074, consistent with zero asymmetry.

Chapter 4

Experimental Results

4.1 Fragment Production

The experimental systems described in the previous chapter were used in the production and identification of ^{55}Ni fragments, and the β-NMR measurement. The ^{55}Ni secondary beam was produced under a variety of conditions to maximize spin polarization and complete the β-NMR measurement. The spin polarization measurements were completed with the ^{55}Ni secondary beam produced at primary beam angles of 2° and 0°, as well as three separate fragment momenta settings of the A1900. The NMR measurement was completed with the primary beam at an angle of 2°, and a single A1900 setting with the momentum corresponding to the peak yield of ^{55}Ni. This chapter presents the particle identification of the secondary beam, the response of the β detectors under the various conditions described above, and the results of both the spin polarization and NMR measurements.

4.2 Particle Identification

Secondary beam particle identification (PID) was performed using the A1900 focal plane detectors for energy loss and tof information. The PID with no wedge at the

intermediate image of the A1900 and a constant value of Bρ is shown in Fig. 4.1. The constant value of B$\rho = mv/q$ yields certain features that are characteristic of the A/q of the fragments. The unbound fragment ^{8}Be did not appear in the PID, and the "hole" where the fragment should appear was used as reference (shown in the lower part of Fig. 4.1). The energy loss of the ^{55}Ni fragments was determined to be 597 MeV through the 0.5 mm thick A1900 focal plane PIN detector.

A 405 mg/cm^2 Al wedge was placed at the intermediate image of the A1900, and the PID was measured again as shown in Fig. 4.2. Based on the energy loss observed in the unwedged PID, the ^{55}Ni fragments were identified with the wedge present.

The Bρ values were scanned and the rate of ^{55}Ni was measured at each Bρ setting to establish the yield distribution as a function of fragment momentum. The momentum distribution is especially important for the spin polarization measurement, as polarization was later measured as a function of fragment momentum at three settings to establish the variation. The measured momentum distribution is shown in Fig. 4.3 with a Gaussian fit. The measured momentum distribution agrees with a calculation that considers conservation of linear momentum, as described in section 5.1.1.

The ^{55}Ni fragments were sent on to the RFFS. Particle identification was performed after filtering at the RFFS diagnostic box, which was located 5.3 m downstream of the RFFS exit. The diagnostic box consisted of an adjustable vertical slit system sandwiched between two retractable parallel-plane avalanche counters (PPAC), and a retractable telescope of Si PIN detectors. The PPACs are position sensitive detectors and were used to determine the slit position for selective removal of unwanted fragments. The vertical position of fragments in the secondary beam after deflection in the RFFS is shown as a function of arrival time in Fig. 4.4. The tof was taken as a time difference between a signal in the RFFS PIN detector and the *rf* frequency of the K1200 cyclotron and thus the faster fragments have longer times in this figure. The upper vertical slit (G183 top) was positioned to +4 mm to select

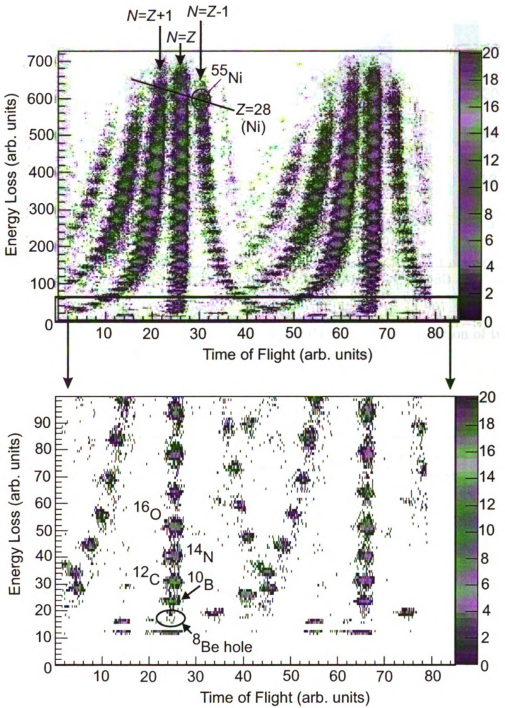

Figure 4.1: Energy loss at the A1900 focal plane PIN detector as a function of time-of-flight with no wedge at the intermediate image. The expanded PID shows the "hole" where unbound ^{8}Be is expected, providing a reference for ^{55}Ni.

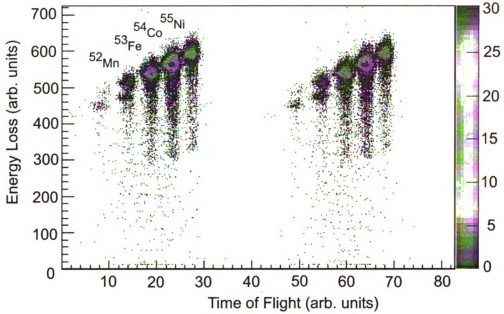

Figure 4.2: Energy loss at the A1900 focal plane PIN detector as a function of time-of-flight with 405 mg/cm^2 Al wedge at the intermediate image.

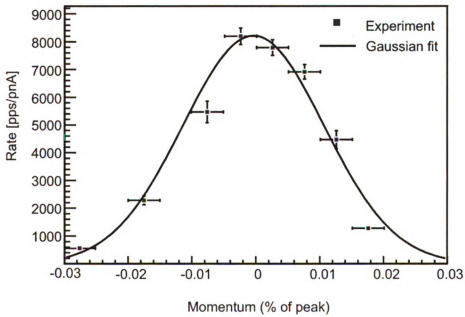

Figure 4.3: Yield distribution of ^{55}Ni as measured at the focal plane of the A1900.

Table 4.1: Fraction of components of the secondary beam, relative to ^{55}Ni, before the RFFS was turned on and after.

Nuclide	Fraction before RFFS	Fraction after RFFS
^{55}Ni	1	1
^{54}Co	1.33	0
^{53}Fe	0.24	0.01
^{52}Mn	0.02	0.02

the deflection region that included the fragment of interest and eliminated unwanted contaminants. Two beam steerers located downstream of the RFFS diagnostic box and upstream of the experimental endstation were used to recenter the fragments onto the optical axis of the experimental endstation. The fractions of each nuclide in the secondary beam relative to ^{55}Ni, before the RFFS was turned on and after, are given in Table 4.1. The primary contaminant in the secondary beam from the A1900 was ^{54}Co, as seen from Fig. 4.4a. Implantation of ^{54}Co would present a particular problem for the β-NMR measurement because it has a half-life and β-endpoint energy similar to that of ^{55}Ni (see Fig. 4.5).

When the RFFS was on with the slits closed, the ^{54}Co contamination was eliminated completely, as shown in Fig. 4.4b. The other contaminants, ^{53}Fe and ^{52}Mn, were not a problem for success of the measurement due to their low β-endpoint energies, although these low-energy contaminants were observed, as will be discussed in section 4.3. Contributions from these low-energy contaminants were removed from the β energy spectra collected at the β-NMR apparatus by making an energy cut in software.

The purified beam was implanted at the center of the β-NMR apparatus. Final particle identification was performed at the endstation as well. Energy loss of the secondary beam was recorded with silicon detector 1, and the tof was taken as a time difference between a signal in that detector and the *rf* frequency of the K1200 cyclotron. The PID measured before the RFFS was turned on is shown in Fig. 4.6a. After the RFFS was turned on and the vertical slits were adjusted, the PID was taken

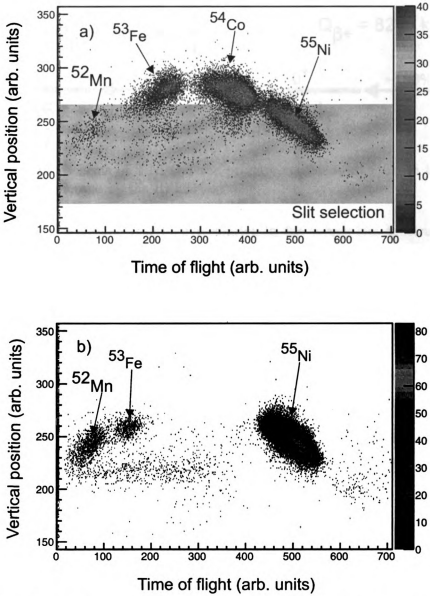

Figure 4.4: Plot of the vertical beam position as a function of tof after the RFFS. a) The gray rectangle highlights the region allowed to pass through the vertical slit system and b) the particle ID resulting from the cut is shown below.

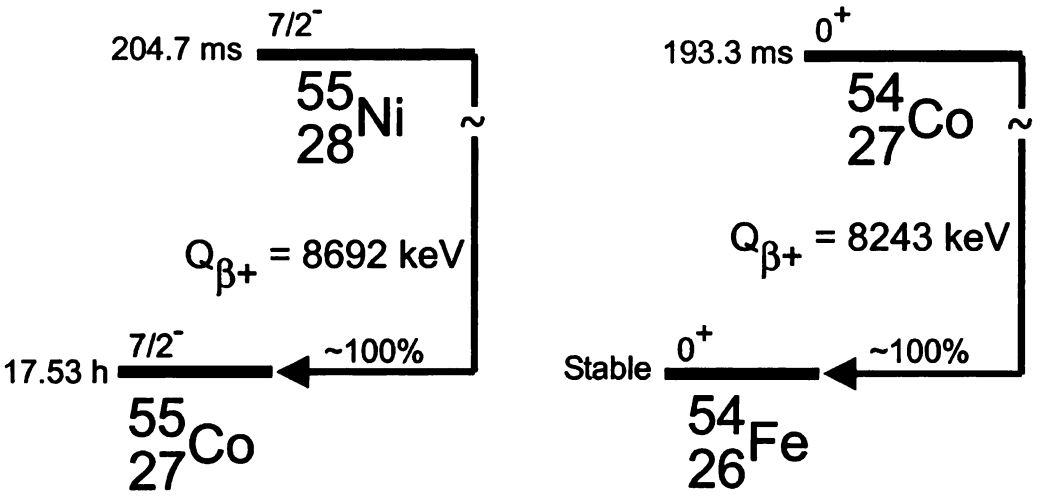

Figure 4.5: Decay scheme of ^{55}Ni and the primary contaminant ^{54}Co in the beam from the A1900 removed by the RFFS.

again as shown in Fig. 4.6b (the poor resolution in the energy loss spectrum was a result of noise from the RFFS slit motors).

4.3 β energy spectra

The β-decay energy spectra for detectors B1-B4 are shown in Figures 4.7 through 4.11. The 1-dimensional spectra taken near the beginning of the experiment as the *rf* was being pulsed on and off is shown in Fig. 4.7. The solid line represents the *rf* on condition, and the dotted black line represents the *rf* off condition. The dotted line falls nearly on top of the solid line, which indicates that the *rf* did not interfere with the detection of β particles or cause the PMTs to behave differently when the *rf* was on versus when it was off. This observation is in agreement with the *rf* on/off source calibration data discussed in section 3.2.4. The small low energy peak that is visable around channel 300 in detectors B1 and B4 represents the decay product, ^{55}Co, which has a Q value of 3.5 MeV (mean β energy 570 keV). A majority coincidence register was added shortly after the experiment started to lower the dead time. The timing signals from B1 and B2, as well as those from B3 and B4, were taken as a logical AND. Further, the CFD thresholds on B1 and B4 were raised from -0.7 V to -1.6 V

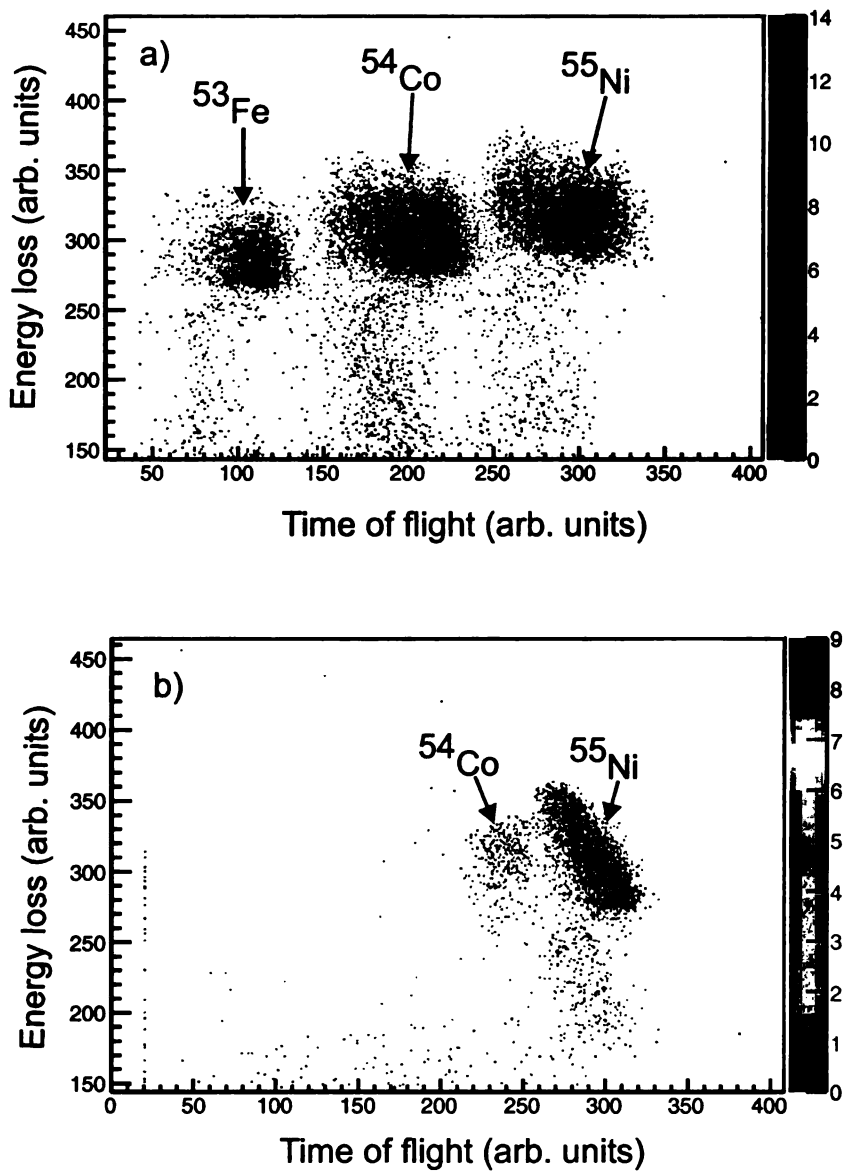

Figure 4.6: Energy loss in silicon detector 1 upstream of the β-NMR apparatus as a function of tof a) before the RFFS was turned on and b) after.

and -1.4 V, respectively, to eliminate the ^{55}Co and other low-energy contamination. The higher threshold on B1 and B4 was at ~400 channels as shown in Fig. 4.8, which corresponds to ~440 keV from the energy calibration in section 3.2.4.

Changes in the β energy spectra were also checked when the external magnetic field, H_0, was pulsed on and off at 1000 G (Fig. 4.9). The spectra show no difference when the external field was on, as compared to when it was off. Again, this observation is in agreement with the calibration data discussed in section 3.2.4. The particular spectra shown were taken before the thresholds on B1 and B4 were raised, and thus the small peak corresponding to ^{55}Co is present in both spectra.

Two-dimensional β-decay energy spectra were constructed by plotting counts in the ΔE detector (B2, B3) as a function of counts in the corresponding E detector (B1, B4) for both up and down telescopes. The thin ΔE detectors has a more uniform response independent of β energy, as demonstrated by the calibration in section 3.2.4.

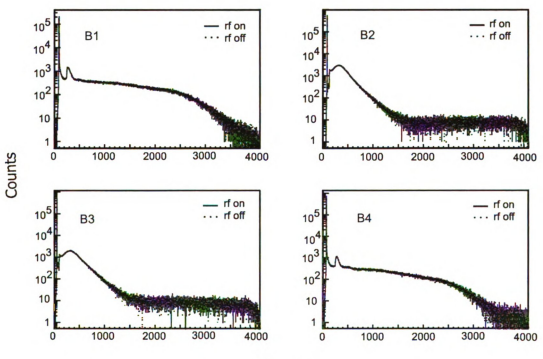

Figure 4.7: ^{55}Ni β decay energy spectra for thick detectors B1 and B4, and thin detectors B2 and B3, for both *rf* on (red) and *rf* off (black).

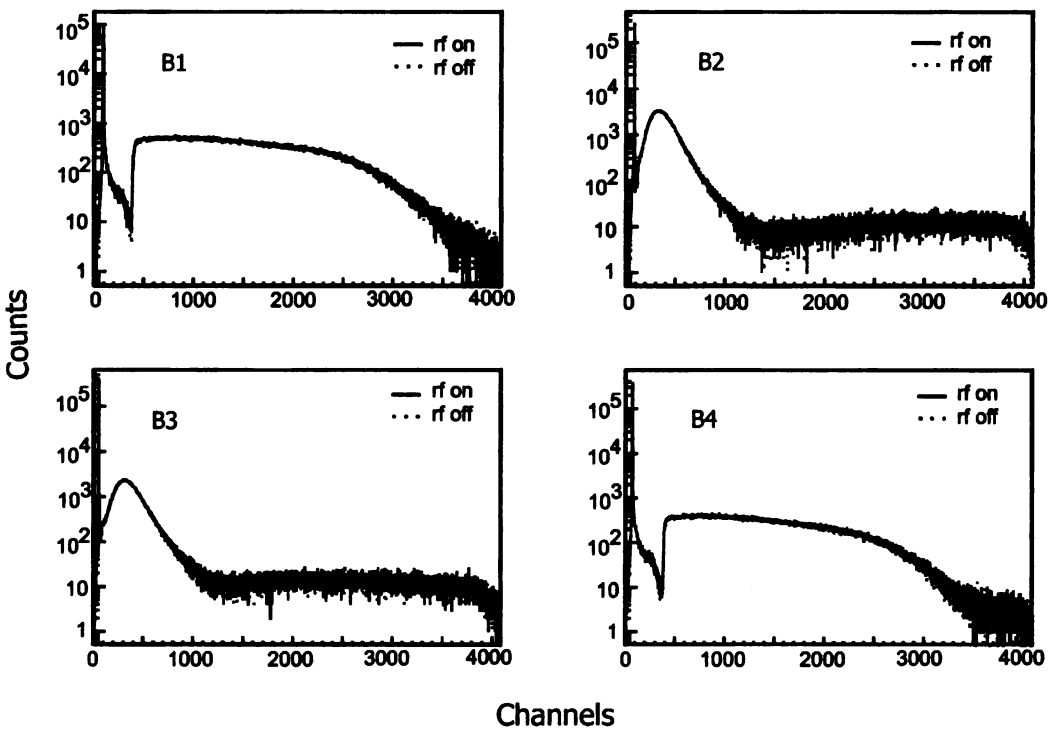

Figure 4.8: ^{55}Ni β-decay energy spectra for thick detectors B1 and B4, and thin detectors B2 and B3, for both *rf* on (red) and *rf* off (black). The B1 and B4 thresholds were raised to reduce low energy contamination.

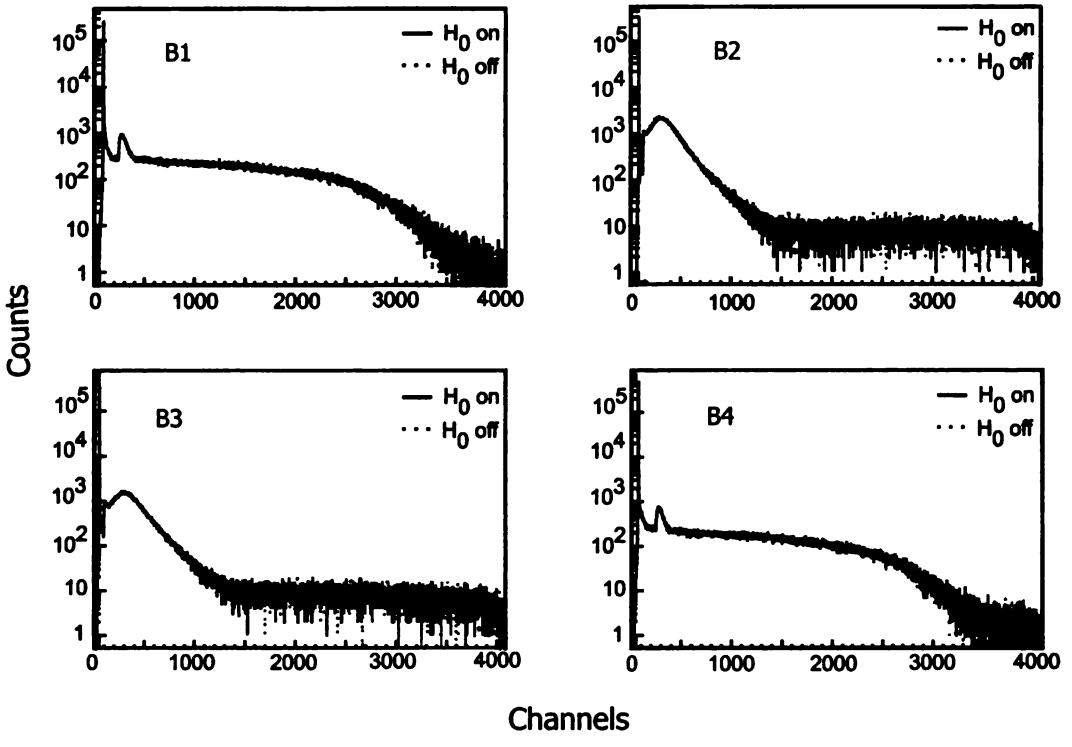

Figure 4.9: ^{55}Ni β-decay energy spectra for thick detectors B1 and B4, and thin detectors B2 and B3, for both external magnetic field H_0 on at 0.45 T (red) and H_0 off (black).

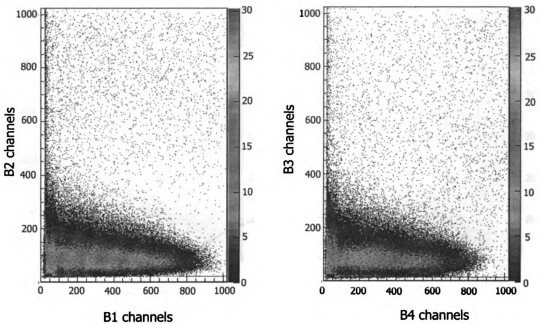

Figure 4.10: Two-dimensional ^{55}Ni β-decay energy spectra plotted as ΔE versus E detector. For these spectra, the external field was held constant at 0.45 T, the *rf* was off, and the threshold on B1 and B4 was -0.7 V.

All β particles deposit the same amount of energy, more or less, as they travel through the thin detector because less scattering occurs. The thick E detector has more of an energy-dependent response since more of the β particles will come to rest in this detector. The 2.0 cm thickness of the E detector is only sufficient to stop β particles with a maximum energy of about 4 MeV. Only a fraction of β particles were stopped in the thick detector due to the high Q value of ^{55}Ni (Q value of 8.7 MeV, mean β energy 3.6 MeV) and the scattering and energy loss properties of the β particles. Shown in Fig. 4.10 are the 2-D telescope spectra for both B2 versus B1 and B3 versus B4. The 2-D spectra constructed after the installment of the MG coincidence condition and with higher thresholds on B1 and B4 are shown in Fig. 4.11.

An example of a background run is shown in Fig. 4.12. A small fraction of high energy cosmic rays were observed. Also, some ^{55}Co (Q value 3.5 MeV, mean β energy 570 keV) remains as background due to its half life of 17 hours, and the fact that the threshold on B1 and B4 was raised to only $\sim$100 channels on B1 and B4, which

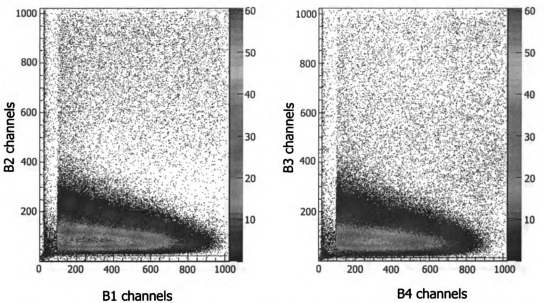

Figure 4.11: Two-dimensional ^{55}Ni β-decay energy spectra plotted as ΔE versus E detector. The external magnetic field was held constant at 0.45 T and the *rf* was off. Thresholds on B1 and B4 were raised to -1.6 V and -1.4 V, respectively, in order to reduce low energy contamination.

corresponds to ~440 keV from the energy calibration in section 3.2.4. At this energy threshold, the majority of the β particles from ^{55}Co were removed as the two strongest β particles have mean energies of 436 keV (26%) and 649 keV. (46%). However, the highest energy particles constitute only a small fraction of the continuous β energy distribution. Additionally, ^{53}Fe and ^{52}Mn are present after the RFFS, and have Q values of 3.7 MeV (mean β energy 1.1 MeV) and 4.7 MeV (mean β energy 1.2 MeV), respectively. ^{53}Fe and ^{52}Mn also contribute to the background spectra. The energy cut taken on the 2-D energy spectra to determine the double ratio did not include the low energy background.

4.4 Spin polarization measurement

An important first step of the ^{55}Ni magnetic moment measurement was to optimize the spin polarization of the secondary beam. The figure of merit for an NMR measurement is P^2Y, where P is the spin polarization and Y is yield. Spin polarization

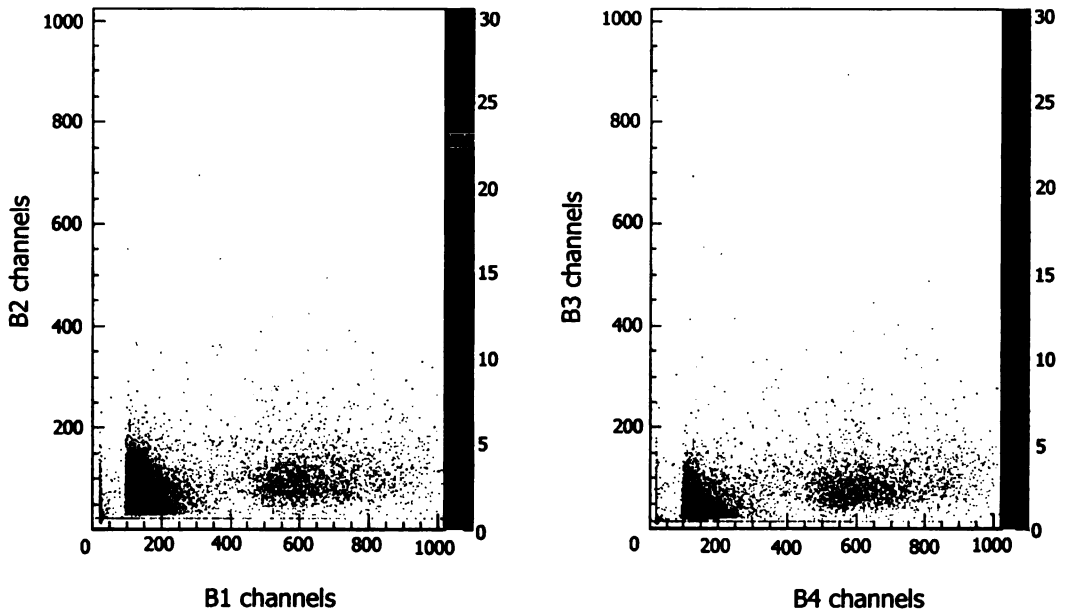

Figure 4.12: Two-dimensional background spectra. The external magnetic field was held constant at 0.45 T and the *rf* was off.

measurements were made at $\Delta p/p$=0 and $\pm 1\%$ relative to the fragment momentum distribution peak to optimize P^2Y and identify the best conditions for the magnetic moment measurement.

The spin polarization was determined for ^{55}Ni fragments produced from bombarding ^{58}Ni on a Be target. The polarization was deduced from the pulsed magnetic field method, where in this application the external magnetic field was set at 1000 G when on, and the pulse duration was 60 s. The β asymmetry was determined from the number of counts in the up and down detectors using Eq. 2.11. The measurement was completed at a 2° primary beam angle to break the symmetry of the fragmentation reaction and realize spin polarization. A normalization run was also taken at 0°, as discussed in section 2.3. At the momentum corresponding to the peak yield of ^{55}Ni, three separate spin polarization measurements were completed at both 2° and 0° at different times throughout the experiment. The deduced spin polarization as a function of the experimental run time is shown in Fig. 4.13. The two spin polarization measurements at $\Delta p/p = \pm 1\%$ were completed near the time of the final central

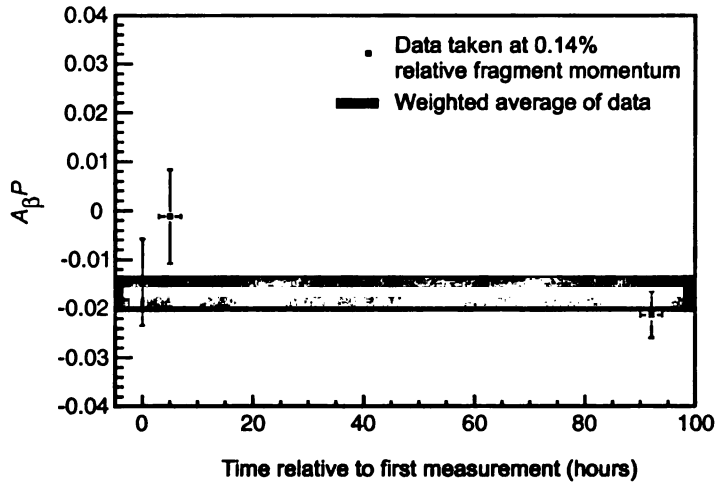

Figure 4.13: Spin polarization of ^{55}Ni plotted as a function of time relative to the first measurement. Data were taken near the central fragment momentum.

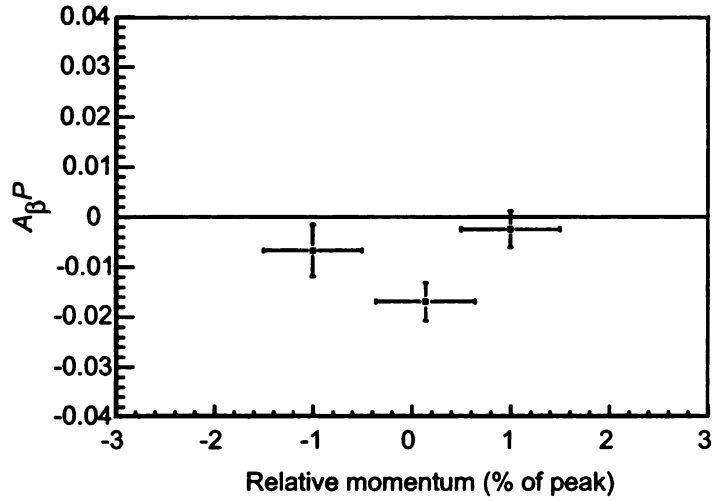

Figure 4.14: Spin polarization of ^{55}Ni plotted as a function of percent momentum relative to the peak of the yield distribution.

momentum measurement. A weighted average was taken of the three points at the central momentum to obtain the final spin polarization curve, as shown in Fig. 4.14.

4.5 NMR measurement

The maximum polarization was observed for ^{55}Ni fragments at the peak of the yield distribution. Therefore, the β-NMR measurement was completed under these condi-

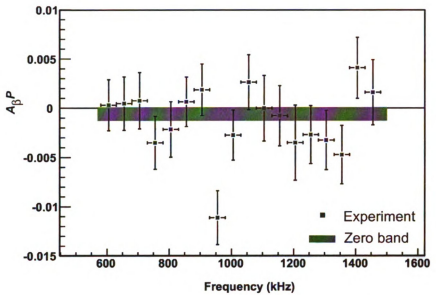

Figure 4.15: Asymmetry $A_\beta P$ as a function of applied frequency. Data taken with FM=$\pm$ 25 kHz is represented by the solid squares with the weighted average of baseline data represented by the gray band.

tions. The primary beam angle was maintained at 2° to break the symmetry of the fragmentation reaction and observe spin polarization. The *rf* was pulsed on and off every 30 s in the region of 605 kHz to 1455 kHz in steps of 50 kHz. H_0 was held constant at 4490.5 G. The FM was $\pm$25 kHz, and the *rf* sweep time was 10 ms (see Fig. 3.18). The H_1 field produced under these conditions was $\sim$5 G. Data was taken at each frequency in Fig. 4.15 for 30 min, and three scans were performed for a total of 90 minutes per frequency point. A resonance was observed at 955 kHz and was found 3.5σ below the weighted average of the other baseline data points. The permutation calculation based on Gaussian statistics gives a probability of 0.83% for a random deviation of at least 3.5σ. Further, the confidence interval for the mean of the baseline was determined, and compared to the statistical error in $A_\beta P$ at 955 kHz. At the 95% confidence level, the 955 kHz point lies 3σ from the baseline.

Prior to the β-NMR scan shown in Fig. 4.15, a new technique was attempted to test the capabilities of the *rf* box. As discussed in Chapter 2, the new *rf* system allowed for the fast, sequential scan of multiple frequencies. Using a frequency modulation of

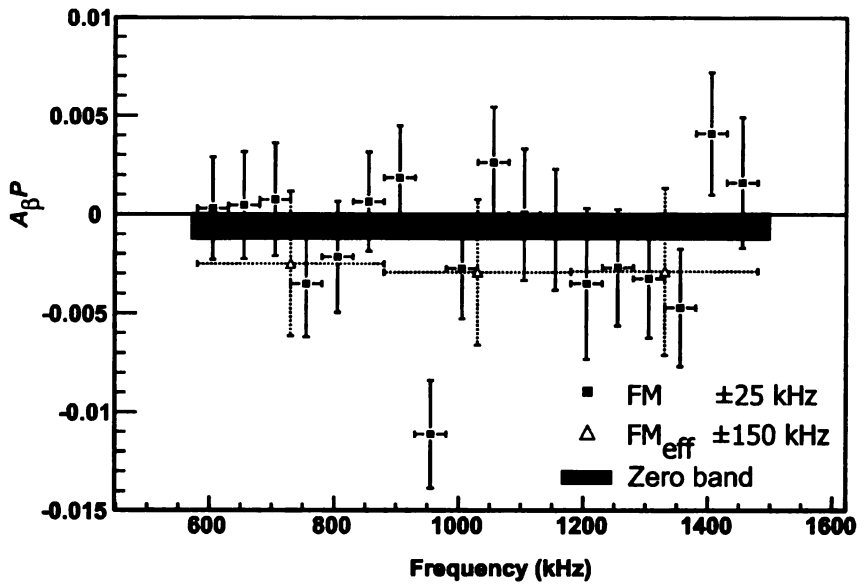

Figure 4.16: Asymmetry $A_\beta P$ as a function of applied frequency. Data taken with FM=± 25 kHz is represented by the solid squares with the weighted average of baseline data represented by the gray band. The multiple frequency scan that used three sequential frequencies of FM=± 50 kHz each is represented by the open triangles with dashed error bars.

±50 kHz, with three sequential frequencies from three different function generators, a frequency region spanning 300 kHz could effectively be monitored. For example, the first scan region included the three frequencies 630, 730, and 830 kHz with a FM of ± 50 kHz each. The *rf* sweep time was still 10 ms, but each frequency was applied for 55 ms in sequence. This sequential application was performed for 30 s, then the *rf* was off for 30 s, and the cycle repeated. Thus, the frequency region 580-880 kHz was scanned in 120 min. The wide modulation scan for the full region 580-1480 kHz is presented in Fig. 4.16. However, the point that covers the identified resonance with the effective ±150 kHz FM did not show the same magnitude of asymmetry as the ±25 kHz resonance point. It may be because the *rf* condition was not exactly the same in both measurements. First of all, the frequency modulation was different; one was ±25 kHz and the other was three points each of ±50 kHz. The *rf* sweep time was the same for both measurements at 10 ms. The wider FM of ±50 kHz required an H_1 of 6 G at the resonance point, according to Eq. 3.2, while an FM of ±25 kHz

only required 4 G. Such difference was accounted for by using an H_1 of 8 G for the ± 50 kHz scan and 5 G for the ± 25 kHZ scan, but there may have been a problem when multiple frequencies were introduced. Further, the statistics on the wide FM data are lower than that for the narrow FM data due to a lower beam intensity at the time the wide FM data was collected. This experiment was the first time the multiple frequency scan technique was attempted for an NMR measurement, and the technique may need more testing before it is fully understood.

The resonance at $\nu_L = 955$ kHz with FM= ± 25 kHz was used to deduce the corresponding g factor as $|g| = 0.279 \pm 0.007$. The magnetic moment was further extracted as $\mu = gI$, with $I = 7/2$ for the ^{55}Ni ground state [58]. The final result is

$$|\mu(^{55}\mathrm{Ni})| = (0.976 \pm 0.026)\mu_N.$$

The uncertainty on μ was evaluated from the width of the FM. The μ was not corrected for the chemical shift due to the interaction of ^{55}Ni with electrons in the lattice, which is not known, but assumed to be small compared to the error on the present result. The sign of g and thus μ cannot be determined directly from the measurement. However, it was assumed negative based on theoretical considerations for a neutron hole in the $1f_{7/2}$ shell.

Chapter 5

Discussion

5.1 Polarization of ^{55}Ni compared to simulation

In Chapter 2, the development of a Monte Carlo code that simulates spin polarization produced in nucleon removal and pickup reactions at intermediate energies was described. The original simulation as described in Ref. [37] was revised to improve the quantitative agreement with experiment [41, 59]. Simulations of the ^{58}Ni fragmentation reaction to produce ^{55}Ni were performed to test the reliability and predictive power of the Monte Carlo code. Details regarding the reaction observables are provided in the following sections.

5.1.1 Momentum distribution reproduction

The Monte Carlo simulation was first used to provide predictions to compare the experimentally-observed momentum distribution to predictions. The momentum of the outgoing fragment was calculated based on conservation of linear momentum. The linear momentum (x, y, and z components) of the group of removed nucleons was modeled using a Gaussian distribution centered at zero with a width, σ, given by

the Goldhaber formula [60],

$$\sigma = \sigma_0 \sqrt{\frac{A_F(A_P - A_F)}{(A_P - 1)}} \tag{5.1}$$

where A_F is the fragment mass, A_P is the projectile mass, and σ_0 is the reduced width. The reduced width is related to the Fermi momentum of the nucleon motion inside the projectile $\sigma_0^2 = p_{Fermi}^2/5$. The $\sigma_{0,expt}$ deduced from experimental distribution variances have been observed to depend on the mass number of the fragmenting projectile nucleus, with a weak dependence on the mass number of the target nucleus and kinetic energy of the projectile [61]. Therefore, a subsequent phenomenological parametrization was used to determine the reduced width for ^{55}Ni. The parametrization considers dependence on fragment mass, target mass, and incident projectile energy, and is applicable over a wide range of masses from $A_P = 12 - 200$. The reduced width was shown to have a linear dependence as a function of A_P. The reduced width was calculated as

$$\sigma_{0,expt} = \left(1 + \frac{E_C}{4T_{lab}}\right)\left(70 + \frac{2A_P}{3}\right) \tag{5.2}$$

where T_{lab} is the beam energy in MeV/nucleon and E_C is the Coulomb energy for the relevant fragmentation reaction, given by

$$E_C = \frac{1.44 Z_P Z_T}{r_P + r_T}. \tag{5.3}$$

In Eq. 5.3, $Z_{P,T}$ are the projectile and target charge numbers, respectively, and $r_{P,T}$ are the uniform distribution nuclear radii given by

$$r_{P,T} = \sqrt{5/3}(r_{P,T})_{rms}, \tag{5.4}$$

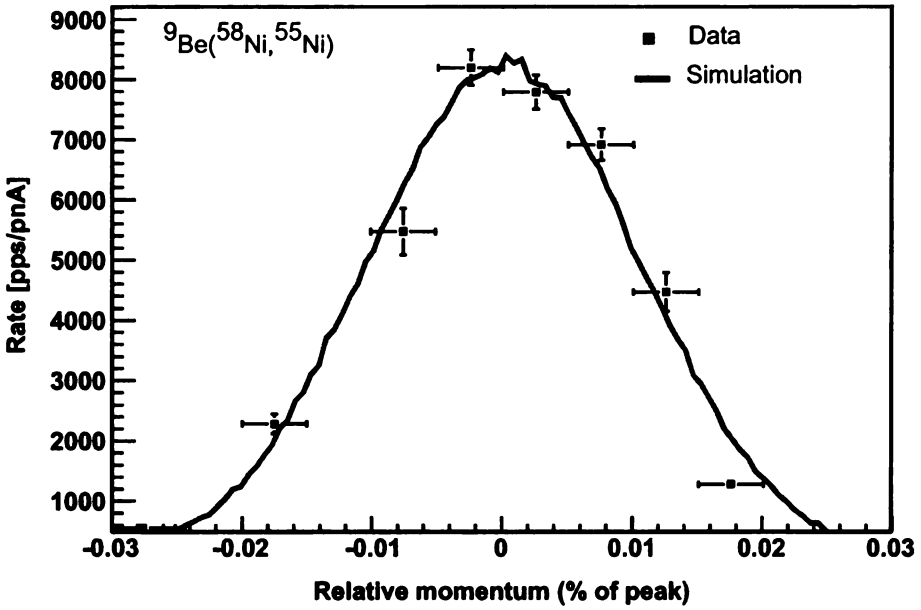

Figure 5.1: Simulated momentum distribution compared to data for the reaction ^{9}Be(^{58}Ni,^{55}Ni) at 160 MeV/nucleon. The red squares represent the data and the blue line represents the results of the simulation.

where the nuclear rms radii are taken from electron scattering measurements [62]. For a 160 MeV/nucleon ^{58}Ni beam on a ^{9}Be target,

$$\sigma_0 = 112 \text{ MeV/c}. \tag{5.5}$$

With this reduced width, the simulation yielded a momentum distribution in good agreement with experiment, as shown in Fig. 5.1.

5.1.2 Optical Potential

The real part of the optical model potential, required to calculate the nucleus-nucleus interaction, V_0, is an input parameter for the mean deflection angle, a parameter of the spin polarization simulation. The deflection angle θ (see Fig. 5.2) for a single interaction is given by

$$\theta = \pi - 2\phi, \tag{5.6}$$

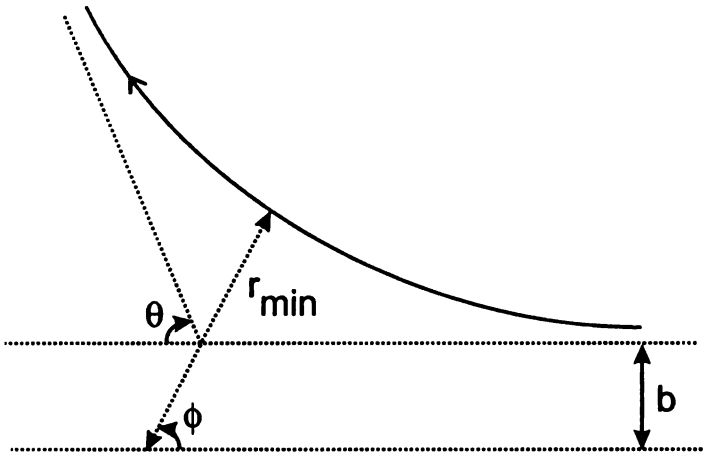

Figure 5.2: Variable definitions for mean deflection angle calculation.

with

$$\phi = \int_{r_{min}}^{\infty} \frac{bdr}{r^2\sqrt{1 - \frac{b^2}{r^2} - \frac{U(r)}{E}}}. \tag{5.7}$$

In Eq. 5.7, b is the impact parameter, r is the distance between the centers of the two interacting objects, $U(r)$ is the potential governing the interaction of the two objects, r_{min} is the separation between the centers of the two point-like objects at the distance of closest approach and the energy, E, is given by

$$E = \frac{1}{2}mv_{\infty}^2, \tag{5.8}$$

where v_{∞} is the velocity of the projectile at $r = \infty$ [63].

The projectile is assumed to move away from the target after the scattering event with momentum equal to the incident momentum, thus $E(v_{\infty}) = E(v_{incident})$. Eq. 5.7 is general for any spherically symmetric potential.

The potential $U(r)$ is defined as

$$U(r) = U_{Coulomb}(r) + U_{nuclear}(r). \tag{5.9}$$

The Coulomb part of the potential is repulsive and is given in Eq. 5.3. The nuclear

part of the potential is taken to be the real part of the optical model [64], and is attractive:

$$U_{nuclear}(r) = \frac{-V_0}{1 + e^{(r-R)/a}}. \tag{5.10}$$

Here V_0 is the depth of the optical model potential, $R = 1.2(\sqrt[3]{A_p} + \sqrt[3]{A_t})$ where A_p and A_t are the masses of the projectile and target respectively, and a is a measure of the diffuseness of the nuclear surface. V_0 and a are parameters fit to experimental data. There are very limited nucleus-nucleus scattering data available in the literature, and an exact determination or parametrization of V_0 is difficult for any given projectile-target combination. Typically this is not a problem because in head-on collisions, the nuclear potential does not have a large influence. However, the treatment of peripheral collisions depends strongly on the optical potential. In the minimum, a determination of V_0 is needed. A parametrization of V_0 based on energy and/or number of nucleons removed would suffice, but unfortunately, such a parametrization does not presently exist.

In the work described in the following sections, V_0 was determined with a folding model calculation [65]. The model was chosen because it reproduces experimental scattering data for heavy ions in the energy range of interest. The folding calculation yields the real part of the optical potential (V_0) as a function of the internuclear radius, the distance between the center of the projectile and target. The internuclear radius was calculated in the simulation code, based on the relations by Gosset *et al.* [66]. For ^{58}Ni at 160 MeV/nucleon on a ^{9}Be target, Khoa calculated the optical potential for a three nucleon removal reaction to be $V_0 = 41$ MeV which corresponds to a mean deflection angle of $\theta_{def} = 0.049$. A renormalization of the real folded potential is usually assumed to account for higher-order effects, with a renormalization coefficient $N = 1 \pm 0.2$ multiplied by the potential. In the case of the ^{9}Be(^{58}Ni,^{55}Ni) reaction, a normalization coefficient of 1.1 ($V_0 = 45$ MeV) was shown to have the best agreement with data.

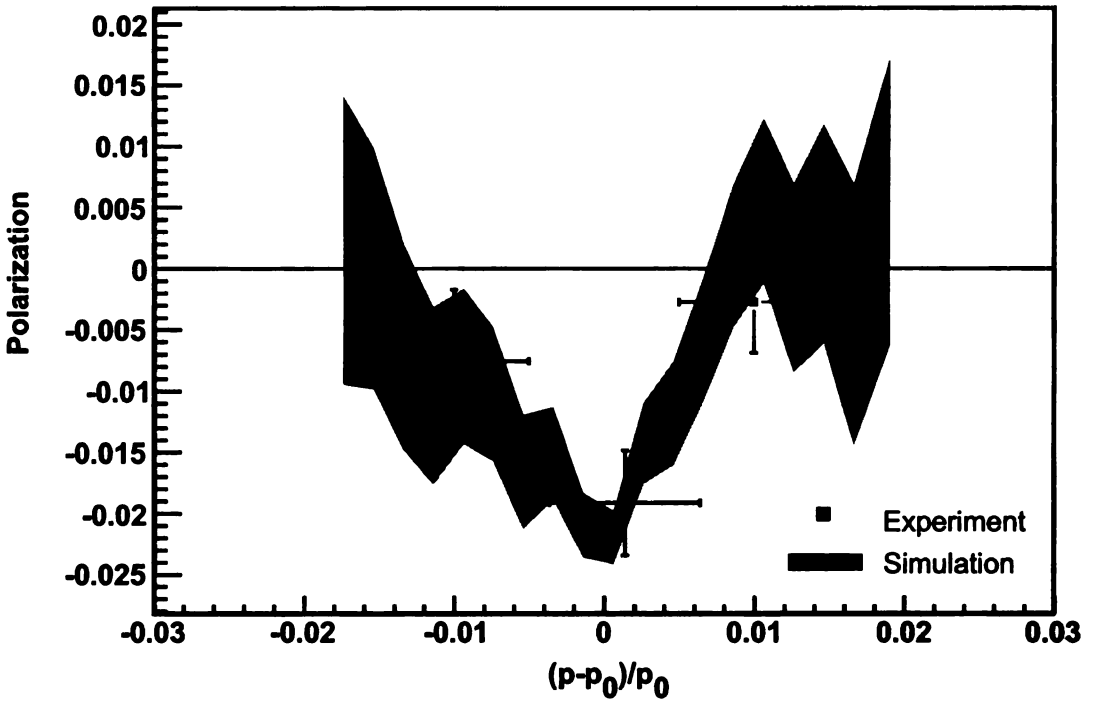

Figure 5.3: Spin polarization as a function fragment momentum p relative to the peak of the yield distribution p_0 for the three neutron removal reaction ^{9}Be(^{58}Ni,^{55}Ni) (160 MeV/nucleon). The red squares are the experimental data points and the grey band represents the range of the Monte Carlo simulation results within a 1σ distribution. The input parameters used in the simulation are given in Table 5.1.

5.1.3 Results of simulation

The spin polarization measurement for the reaction ^{9}Be(^{58}Ni,^{55}Ni) at 160 MeV/nucleon (see Fig. 4.14) is shown along with simulation results in Figure 5.3. The parameters used in the simulation are given in Table 5.1.

A value of $A_\beta = 0.885$ was used to extract polarization for the ^{55}Ni analysis. Calculation of A_β as outlined in Appendix A gives two values, $A_\beta = +0.885$ or $A_\beta = -0.747$ depending on the sign of the mixing ratio ρ, which is not experimentally known. The polarization simulation predicts negative polarization at the peak of the yield distribution. A positive value of A_β is needed for the polarization measurement to have the same sign as simulation. The sign of the Gamow-Teller matrix element should be determined to confirm this assignment of A_β. A negative spin polarization is expected for the three neutron removal reaction based on the previ-

Table 5.1: Input parameters used in the Monte Carlo simulation to model the spin polarization of the nucleon removal reaction ^{9}Be(^{58}Ni,^{55}Ni), and the nucleon pickup reactions ^{9}Be(^{36}Ar,^{37}K) and ^{9}Be(^{36}S,^{34}Al).

Parameter	^{9}Be(^{58}Ni,^{55}Ni)	^{9}Be(^{36}Ar,^{37}K)	^{9}Be(^{36}S,^{34}Al)
A, Z of projectile	58, 28	36, 18	36, 16
A, Z of target	9, 4	9, 4	9, 4
Incident energy (MeV/nucleon)	160	150	77.5
Distance of closest approach (fm)	5.47	5.44	5.40
Number of events	500000	500000	500000
Angular acceptance (deg)	2 ± 2.5	2 ± 2.5	2 ± 1
Optical potential (MeV)	45	29	32
Mean deflection angle (rad)	0.014	-0.07	-0.49

ous considerations of conservation of linear momentum. Recall that the definition of polarization is dependent on $l_z/|L|$. $|L| = \sqrt{L_x^2 + L_y^2 + L_z^2}$ is a positive value and $l_z = -Xk_y + Yk_x$. At the peak of the momentum distribution, the fragment momentum is zero, and thus $k_y = 0$. The fragments accepted into the A1900, as shown in Fig. 3.2, had an x-component of linear momentum that was negative. Therefore, the x-momentum of the removed nucleons, k_x is positive. As discussed above, $Y < 0$ for non-uniform removal as shown in Fig. 2.2; therefore, l_z and P must be negative.

5.1.4 Extension to nucleon pickup reactions

A complete quantitative treatment of intermediate energy reactions is important to the success of the spin polarization simulation code. In addition to nucleon removal reactions, nucleon pickup reactions at intermediate energies provide a means for producing spin polarized nuclei away from stability. The spin polarization mechanism for both nucleon removal and pickup reactions is believed the same. Therefore, the simulation code was extended to include nucleon pickup, independent of the efforts reported in Ref. [40].

The pickup process follows the observations of Souliotis *et al.* [39], in that the picked-up nucleon has an average momentum equal to the Fermi momentum (230 MeV/c), oriented parallel to the beam direction. The momentum distribution for the

one-neutron pickup reaction ^{27}Al(^{18}O,^{19}O) at 80 MeV/nucleon is shifted below the momentum/nucleon of the beam, as observed in Ref. [39], in contrast to the observed shift for nucleon removal products. The simulated position of the centroid agrees with the calculation of Ref. [39], where a simple model based on momentum conservation was used (see Fig. 5.4). The agreement demonstrates that angular momenta considerations are employed correctly in the Monte Carlo code modified for nucleon pickup.

The width of the momentum distribution is observed experimentally to be small (around 20 MeV/c), while it is calculated to be zero. The $\sigma_{\parallel}^2$ from Goldhaber [60] is

$$\sigma_{\parallel}^2 = \sigma_0^2 \frac{A_{PF}(A_P - A_{PF})}{A_P - 1}, \tag{5.11}$$

where $A_{PF} = A_F - \Delta A_t$ is the mass of the projectile part of the final product and ΔA_t is the number of nucleons picked up from the target. As discussed in section 5.1.1, the parameter σ_0 is the reduced width, and is related to the Fermi momentum of the nucleon motion inside the projectile: $\sigma_0^2 = p_{Fermi}^2/5$. Eq. 5.11 assumes that the nucleon is picked up from the target with a fixed momentum and direction, and the picked-up nucleon makes no contribution to the width. Thus, for any pure nucleon pickup process, $A_P = A_{PF}$ and the parallel width is zero. To model the experimental observations of Ref. [39], a parallel width of $\sigma_{\parallel} = 20$ MeV/c was used. In addition to the parallel width, Van Bibber *et al.* [67] showed that in heavy-fragment studies in the 100 MeV/nucleon region, the projectile is subject to an orbital deflection due to its interaction with the target nucleus before fragmentation takes place. The orbital deflection gives an additional dispersion of the transverse momentum, as given in the expression:

$$\sigma_{\perp}^2 = \sigma_1^2 \frac{A_{PF}(A_P - A_{PF})}{A_P - 1} + \sigma_2^2 \frac{A_{PF}(A_{PF} - 1)}{A_P(A_P - 1)}. \tag{5.12}$$

The first term in Eq. 5.12 was defined previously (Eq. 5.11, where σ_0 is replaced by σ_1), and the second term contains σ_2^2, the variance of the transverse momentum

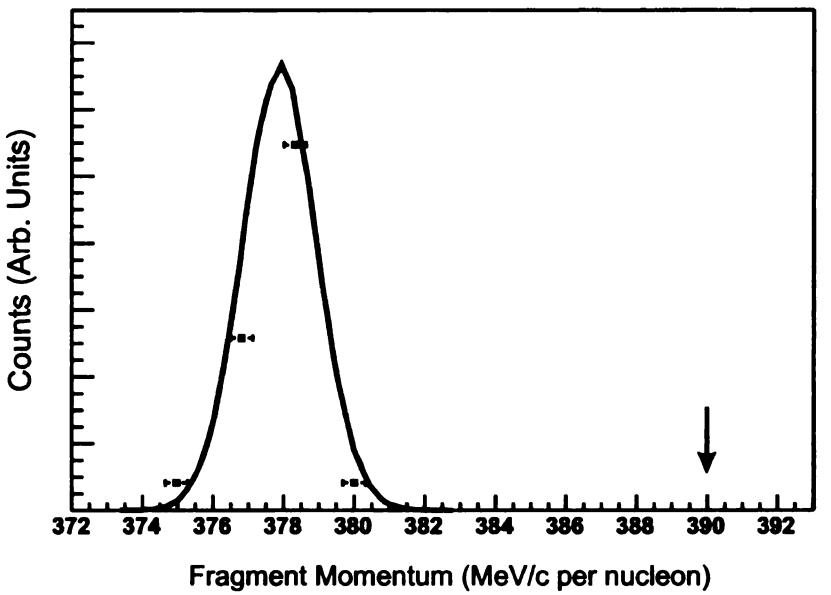

Figure 5.4: Parallel momentum/nucleon distribution calculated with the simulation code for the reaction ^{27}Al(^{18}O,^{19}O) at 80 MeV/nucleon. The red squares are the data [39] and the black line represents the simulation results. The arrow corresponds to the momentum/nucleon of the beam. The simulated momentum distribution has been scaled by the ratio observed in Ref. [39] of experimental centroid/calculated centroid (0.969/0.978), in order to compare to the data.

of the projectile at the time of fragmentation (200 MeV/c as used in Ref. [67]). A comparison of the simulated momentum distribution is shown in Fig. 5.4 with the data taken from Ref. [39].

The simulation results for one-nucleon pickup processes discussed in the literature are shown in Fig. 5.5 and 5.6. Souliotis *et al.* [39] used the "typical" Fermi momentum p_{Fermi}=230 MeV/c in the momentum distribution calculation. p_{Fermi} was calculated here based on data taken from Moniz *et al.* [68]. The p_{Fermi} ranges from 170 MeV/c for the lightest targets to 260 MeV/c for heavier targets. The results of the simulation for a proton pickup ^{9}Be(^{36}Ar,^{37}K)X, first observed by Groh *et al.* [38], are given in Fig. 5.5. The parameters of the simulation are listed in Table 5.1. The momentum matching conditions [69] for simple surface-to-surface pickup are best met for the two data points on the high momentum side of the yield distribution, where the simulation agrees with the data. On the low momentum side of the peak of the yield curve, the picked-up nucleon has a momentum less than the Fermi momentum,

and the momentum matching conditions for direct pickup are poorly satisfied. More complex transfer mechanisms are therefore required to describe the polarization on the low momentum side [38].

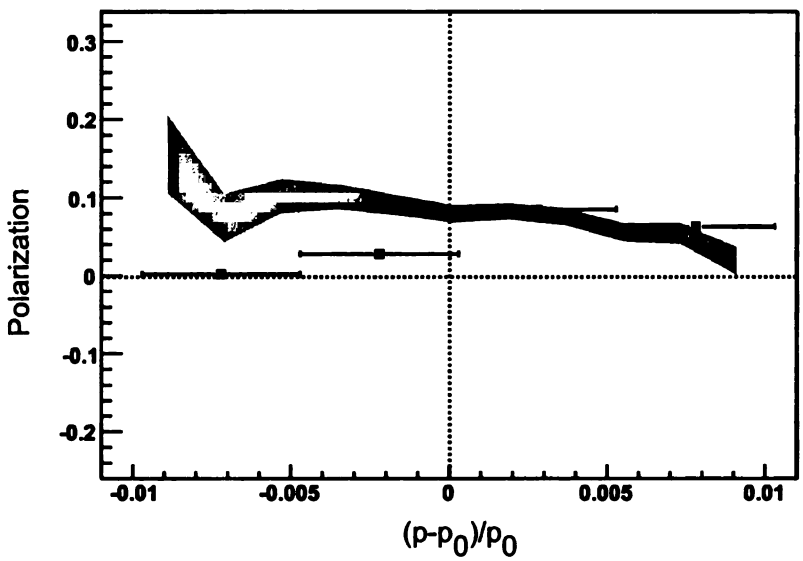

Figure 5.5: Polarization as a function of fragment momentum p relative to the primary beam momentum p_0 for the one-proton pickup reaction ^{9}Be(^{36}Ar,^{37}K) (150 MeV/nucleon). The red squares are the experimental data points from Ref. [38] and the grey band represents the range of simulation results within a 1σ distribution.

The simulation code was also used to model data from a neutron pickup reaction, ^{9}Be(^{36}S,^{34}Al) at 77.5 MeV/nucleon obtained in Ref. [40], as shown in Fig. 5.6. Again, the simulation parameters are given in Table 5.1. These data were reproduced by an independent simulation of the nucleon pickup in Ref. [40], but required a scaling factor of 0.25. No scaling factor was applied in the results presented here to reproduce the polarization from neutron nor proton pickup reactions.

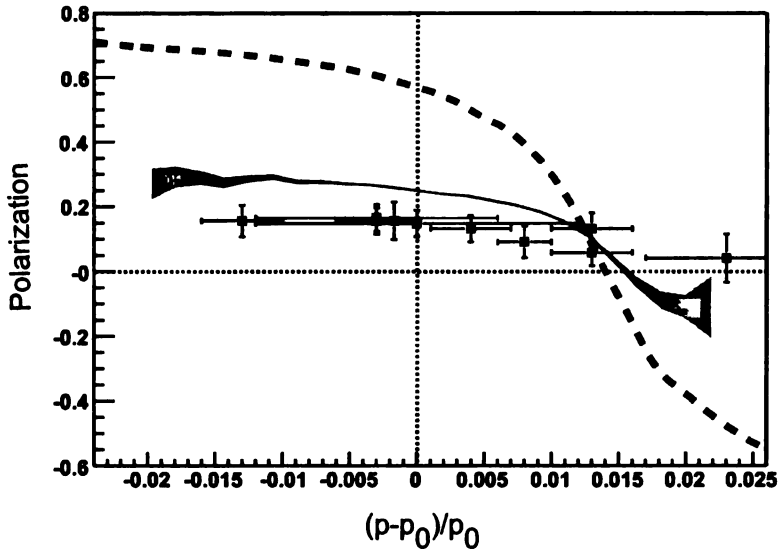

Figure 5.6: Polarization as a function of fragment momentum p relative to the momentum at the peak of the yield distribution p_0 for the one-neutron pickup reaction ^{9}Be(^{36}S,^{34}Al) (77.5 MeV/nucleon). The red squares are the experimental data points and the blue dashed line is the previous simulation result, both from Ref. [40]. The grey band represents the range of the present simulation results within a 1σ distribution.

5.2 Magnetic Moment of ^{55}Ni and the ^{56}Ni closed shell

As given in section 4.5, the magnetic moment of ^{55}Ni was deduced as

$$\mu(^{55}\mathrm{Ni}) = (-0.976 \pm 0.026)\mu_N.$$

The new $\mu(^{55}\mathrm{Ni})$ is compared below to theoretical predictions. The starting point for the discussion is a simple single-particle wavefunction, where μ is then corrected with an effective operator. The discussion is then expanded to consider a more sophisticated wavefunction for the ^{55}Ni ground state.

5.2.1 Single-particle wavefunction and effective g factors

The new $\mu(^{55}\mathrm{Ni})$ was first compared to the results of a calculation that used a simple form of the wavefunction, where ^{56}Ni was assumed to be an inert closed core. The magnetic moment operator was described in Refs. [5,6] as:

$$\vec{\mu}_{\mathrm{eff}} = g_{l,\mathrm{eff}}\langle l\rangle + g_{s,\mathrm{eff}}\langle s\rangle + g_{p,\mathrm{eff}}\langle[Y_2, s]\rangle, \tag{5.13}$$

where $g_{x,\mathrm{eff}} = g_x + \delta g_x$, with $x = l, s$, or p, and g_p denotes a tensor term. Here g_x is the free nucleon g factor g_{free} ($g_s = 5.586$, $g_l = 1$ for proton and $g_s = -3.826$, $g_l = 0$ for neutron) and δg_x the correction to it. s and l represent spin and orbital angular momentum, respectively. The results of the calculation for both a single proton (^{55}Co) and single neutron (^{55}Ni) configuration in the $1f_{7/2}$ shell are shown in Table 5.2. Details of the calculation and individual corrections can be found in [5–7], and the corrections were discussed in section 1.2.2. Starting from the single-particle values for $\mu(^{55}\mathrm{Ni})$ and $\mu(^{55}\mathrm{Co})$, the CP corrections overcorrect experimental values (see Fig. 5.7), but the MEC restore the theoretical prediction close to the experimental values. The isobars and relativistic effects have only small contributions to the correction. The simple theoretical model, labeled as $g_{\mathrm{eff}}^{\mathrm{perturbation}}$, reproduces the experimental values for ^{55}Ni and the mirror partner ^{55}Co well, as shown in Table 5.2.

5.2.2 Shell model in full *fp* shell and g_{free}

Another theoretical approach was taken using a complex wavefunction in a shell model calculation to gain more insight on the details of the ^{56}Ni core. The shell model calculation was performed in the full *fp* shell with the effective interaction GXPF1 [4], where ^{40}Ca was assumed to be an inert closed core. Here, the ^{56}Ni core is soft as the probability of the lowest order closed-shell $\pi(1f_{7/2})^8\nu(1f_{7/2})^8$ configuration in the ground-state wavefunction is ~60%. The magnetic moment can be calculated from g_{free} with a form of the magnetic moment operator $\vec{\mu} = g_s\langle s\rangle + g_l\langle l\rangle$. In

Table 5.2: Contributions to the calculated effective magnetic moment operator for a $1f_{7/2}$ neutron in ^{55}Ni and a $1f_{7/2}$ proton in ^{55}Co.

	Neutron $1f_{7/2}$ (^{55}Ni)				Proton $1f_{7/2}$ (^{55}Co)			
	g_l	g_s	g_p	μ	g_l	g_s	g_p	μ
CP[a]	0.185	1.933	3.339	1.744	-0.183	-2.188	-3.892	-1.905
MEC[b]	-0.245	-0.614	-0.368	-1.066	0.270	0.693	0.340	1.181
Isobars	0.010	0.288	-0.889	0.117	-0.010	-0.288	0.888	-0.117
Relativistic	0.000	0.093	0.000	0.046	-0.024	-0.151	-0.040	-0.150
sum of all corrections	-0.049	1.701	2.082	0.841	0.052	-1.935	-2.704	-0.990
single-particle value	0.000	-3.826	0.000	-1.913	1.000	5.587	0.000	5.794
single-particle value + corrections	-0.049	-2.125	2.082	-1.072	1.052	3.652	-2.704	4.804

[a]contains both random phase approximation (RPA) and second-order effects (CP(2nd)).
[b]contains meson exchange corrections as well as a core-polarization correction to the two-body MEC operator (MEC-CP).

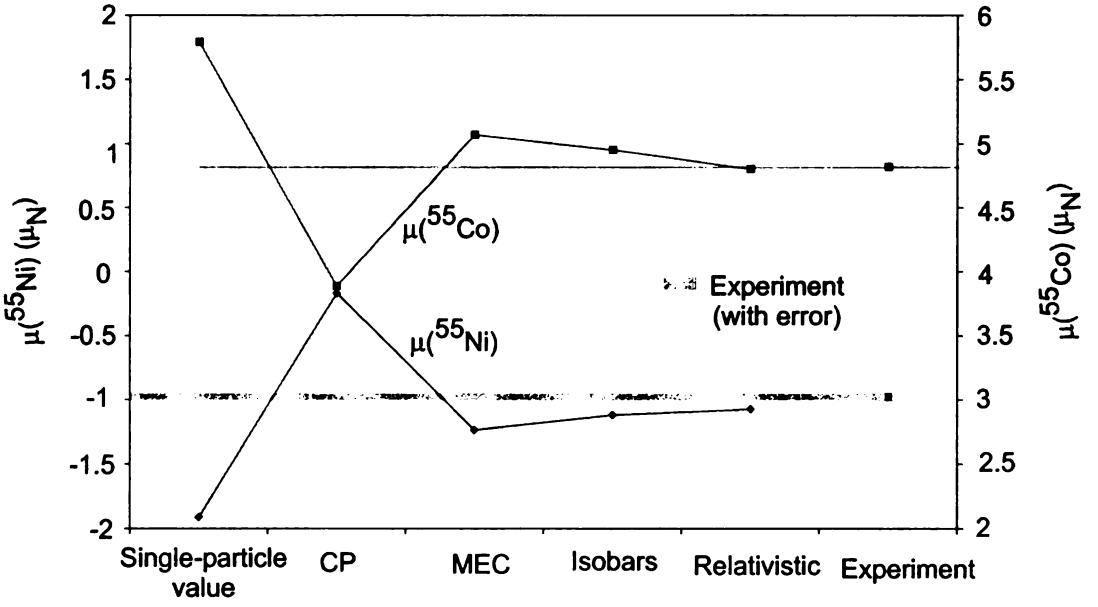

Figure 5.7: Running sum of Towner corrections to the single-particle magnetic moment for ^{55}Ni (blue diamonds) and ^{55}Co (pink squares).

Table 5.3: Magnetic moments of ^{55}Ni,^{55}Co and the isoscalar spin expectation values of the mass $A = 55$ system.

	$\mu(^{55}\mathrm{Ni})\mu_N$	$\mu(^{55}\mathrm{Co})\ \mu_N$	$\langle\sum\sigma_z\rangle$
Experiment	-0.976 ± 0.026	4.822 ± 0.003 [25]	0.91 ± 0.07
Single-particle value	-1.913	5.792	1.00
$g_{\mathrm{eff}}^{\mathrm{perturbation}}$	-1.072	4.803	0.61
full *fp* g_{free}	-0.809	4.629	0.84
full *fp* $g_{\mathrm{eff}}^{\mathrm{moments}}$	-0.999	4.744	0.65
full *fp* $g_{\mathrm{eff}}^{sd\ \mathrm{fit}}$	-1.071	4.926	0.94
full *fp* $g_{\mathrm{eff}}^{sd\ \mathrm{fit}}$ without isoscalar $\delta g_l^{sd\ \mathrm{fit}}$ term	-1.129	4.868	0.63

general, good agreement is realized by this treatment for $N \sim Z$ nuclei over the range $A = 47 - 72$. The shell model calculation gives $\mu(^{55}\mathrm{Ni})$=-0.809 μ_N with g_{free}, which is in fair agreement with the present result as compared with other μ calculations in Ref. [4]. The observed agreement supports the softness of the ^{56}Ni core. Similar results were obtained for the probability of the $\pi(1f_{7/2})^8\nu(1f_{7/2})^8$ closed shell component in the wavefunction from a separate shell model calculation [31] that explained the discrepancy between the systematics of $E(2_1^+)$ and that of $B(E2; 0_1^+ \rightarrow 2_1^+)$ for ^{56}Ni.

5.2.3 Shell model in full *fp* shell and g_{eff}

Effective nucleon g factors, $g_{\mathrm{eff}}^{\mathrm{moments}}$, may be employed in the previously discussed full *fp* shell model calculation for better agreement. The $g_{\mathrm{eff}}^{\mathrm{moments}}$ were derived empirically by the least-square fit of the magnetic moment operator to experimental $\mu(^{57-65,67}\mathrm{Ni})$ and $\mu(^{62-68,70}\mathrm{Zn})$ [4]. The values $g_{\mathrm{eff}}^s = 0.9 g_{\mathrm{free}}^s$, $g_{\mathrm{eff}}^l = 1.1$ and -0.1 for protons and neutrons, respectively, were obtained. The resulting magnetic moment, $\mu(^{55}\mathrm{Ni})$=-0.999 μ_N, gives good agreement with the experimental value. The results of the theoretical calculations are summarized in Table 5.3. It is noted that all of the theoretical calculations give good agreement with the experimental value, and within the accuracy of nuclear structure models, there is not a significant difference between the result of the calculations for μ.

5.2.4 Isoscalar spin expectation value at $T = 1/2$, $A = 55$

The known value $\mu(^{55}\mathrm{Co}) = 4.822 \pm 0.003\ \mu_N$ [25] was combined with the present result for $\mu(^{55}\mathrm{Ni})$ to extract $\langle \sum \sigma_z \rangle$ for the mirror pair at $A = 55$. Using Eq. (1.44),

$$\left\langle \sum \sigma_z \right\rangle = 0.91 \pm 0.07$$

was obtained. A peculiar feature is noted in Table 5.3 between calculated μ and $\langle \sum \sigma_z \rangle$ for $A = 55$. The shell model calculation with g_{free} reasonably reproduces the $\langle \sum \sigma_z \rangle$, although the agreement with μ is only fair. However, the calculation considering $g_{\mathrm{eff}}^{\mathrm{moments}}$ gives good agreement for μ, but does not agree with experimental $\langle \sum \sigma_z \rangle$. Such discrepancy was already noted in the *sd* shell, and can be explained by examining the isovector and isoscalar components of the M1 operator separately [70, 71]. The magnetic moment is dominated by the isovector term due to the opposite signs and nearly equal magnitude of the neutron and proton magnetic moments, whereas $\langle \sum \sigma_z \rangle$ is an isoscalar quantity.

The effective g factors for the $A = 28$ system obtained from a fit to isoscalar magnetic moments, isovector moments, and M1 decay matrix elements [71], $g_{\mathrm{eff}}^{sd\ \mathrm{fit}}$, were applied to matrix elements for $A = 55$ calculated in Ref. [4] with the GXPF1 interaction to see if a similar approach would realize success in the *fp* shell. This approach assumes the hole configuration in the $1d_{5/2}$ shell for $A = 28$ is analogous to that of $1f_{7/2}$ for $A = 55$. Effective g factors for $A = 28$ were obtained as $g_s^{sd\ \mathrm{fit}} = 4.76$, -3.25, $g_l^{sd\ \mathrm{fit}} = 1.127$, -0.089 and $(g_p')^{sd\ \mathrm{fit}} = 0.41$, -0.35 for protons and neutrons, respectively ($g_p' = g_p/\sqrt{8\pi}$). The calculated $\mu(^{55}\mathrm{Ni})$=-1.071 and $\langle \sum \sigma_z \rangle = 0.935$ with $g_{\mathrm{eff}}^{sd\ \mathrm{fit}}$ shows the best agreement with the present result as summarized in Table 5.3.

$\langle \sum \sigma_z \rangle$ is known to be quenched relative to the extreme single particle model. Further, $\langle \sum \sigma_z \rangle$ was shown to be quenched relative to the theoretical $\langle \sum \sigma_z \rangle$ calculated with g_{free} [70] (dotted line in Fig. 5.8) at the beginning ($1d_{5/2}$) and the end ($1d_{3/2}$) of the $A = 17 - 39$ region. It is also known that the $\langle \sum \sigma_z \rangle$ around $A = 30$ are rela-

tively well reproduced with $g_{\rm free}$, as shown in Fig. 5.8. Optimum M1 operators were determined semi-empirically for the *sd* shell nuclei based on the fit to the isoscalar magnetic moment derived from the sum of the mirror magnetic moments [71]. This procedure to determine the effective M1 operator can be justified since the effective operator determined by the magnetic moments ($g_{\rm eff}^{\rm moments}$) is dominated by the large spin isovector component [$g_s^{\rm IVM1} = (g_s^p - g_s^n)/2 = 4.706$] and thus is not sensitive to the small isoscalar components, to which $\langle\sum\sigma_z\rangle$ is sensitive. Corrections to $g_{\rm free}$ were determined for possible pairs of orbits in the *sd* shell [71]. The $\langle\sum\sigma_z\rangle$ calculated with the effective operator better reproduces the experimental result over the *sd* shell and quantitatively reconciles the observed quenching (dashed line in Fig. 5.8). Similarly, in the *fp* shell, the $\langle\sum\sigma_z\rangle$ for the $A = 41$ and 43 mirror pairs at the beginning of the *fp* shell ($1f_{7/2}$) are quenched relative to values calculated with $g_{\rm free}$. The present result at $A = 55$ with single hole in the $1f_{7/2}$ shell is well reproduced by the $\langle\sum\sigma_z\rangle$=0.84 calculated with $g_{\rm free}$ and is close to the extreme single-particle value. The same trend can be seen in the *sd* shell at $A = 27$ (a hole configuration in the $1d_{5/2}$ shell), where the $\langle\sum\sigma_z\rangle$ is well explained by the calculation with $g_{\rm free}$ and restored close to the single-particle value relative to neighboring $\langle\sum\sigma_z\rangle$.

The ^{56}Ni core could be considered as a good core since $\langle\sum\sigma_z\rangle$ for $A = 55$ is very close to the single-particle value. However, if the ^{56}Ni core is soft as shown from the satisfactory μ results from the shell model calculation with the GXPF1 interaction, then configuration mixing should account for the ~40% of the ground state wavefunction not attributed to $\pi(1f_{7/2})^8\nu(1f_{7/2})^8$. This configuration mixing should appear as a deviation in $\langle\sum\sigma_z\rangle$ from the single-particle value, which was not observed. It can be shown from the $\langle\sum\sigma_z\rangle$=0.628 calculated without isoscalar correction to the $g_l^{sd\ \rm fit}$, δ_l^{IS}, that a contribution from the large orbital angular momentum (f orbit) to the $g_l^{sd\ \rm fit}$ enhances the $\langle\sum\sigma_z\rangle$. The contribution to $\langle\sum\sigma_z\rangle$ from the large orbital angular momentum correction cancels the effect from configuration mixing, supporting the softness of the ^{56}Ni core and emphasizing the sensitivity of $\langle\sum\sigma_z\rangle$ to nuclear

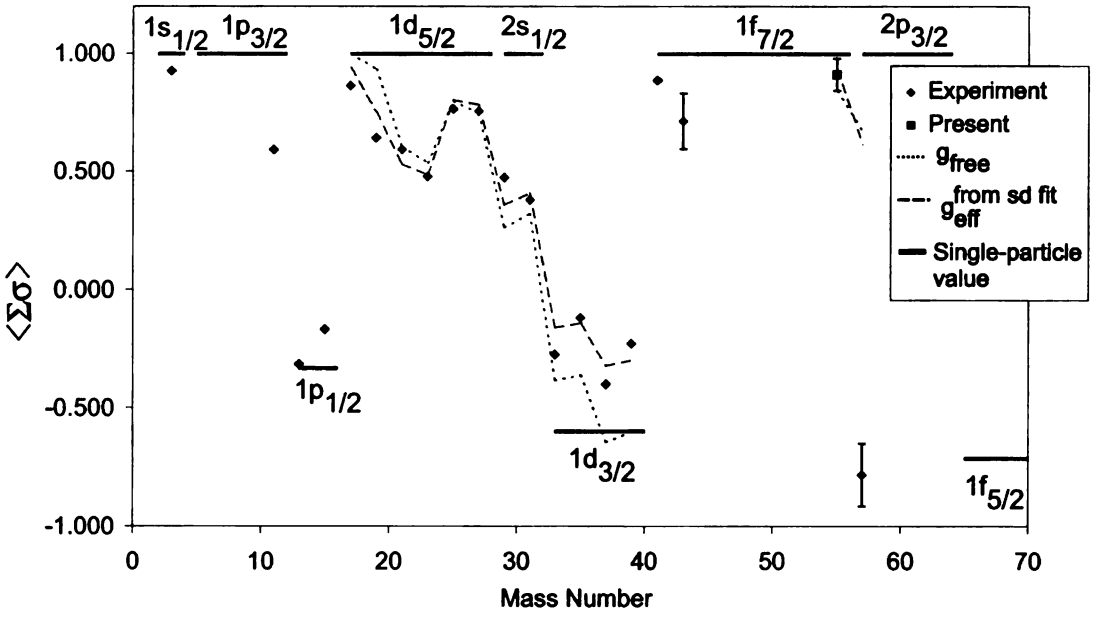

Figure 5.8: Isoscalar spin expectation value for $T = 1/2$ mirror nuclei. The black diamonds represent previous experimental data while the red square is the present result. The blue solid line represents a shell model calculation with free nucleon g-factors. The pink dashed line is the Brown calculation [71] with effective g-factors that were obtained from a fit to the isoscalar magnetic moment in the *sd* shell. The black horizontal lines are the single-particle values.

structure. Similar enhancement of $\langle \sum \sigma_z \rangle$ due to δ_l^{IS} was found in Fig. 5 of Ref. [71] for $A = 39$. The enhancement may be attributed to a large MEC contribution to δ_l^{IS}. Calculations by Arima *et al.* [72] that included MEC corrections were found to agree with the empirical value of δ_l^{IS}. However, it is noted that the MEC depends sensitively on the choice of the meson-nucleon coupling constants (see Ref. [6, 71]) and that calculations by Towner [6] do not show such enhancement, attributed to the MEC being offset by the relativistic effect. The contribution to $\langle \sum \sigma_z \rangle$ from the tensor term $g_p^{sd\ \mathrm{fit}}$ is small as $\langle \sum \sigma_z \rangle$=0.94(0.87) is calculated with(without) the tensor term. The good agreement between the present result and the $\langle \sum \sigma_z \rangle$ calculated with $g_{\mathrm{eff}}^{sd\ \mathrm{fit}}$ in the *sd* shell implies that a universal operator can be applied to both the *sd* and *fp* shells. However, for more detailed discussion, effective M1 operators of the *fp* shell nuclei have to be determined from the mirror moments in the *fp* shell, for which more experimental data are required.

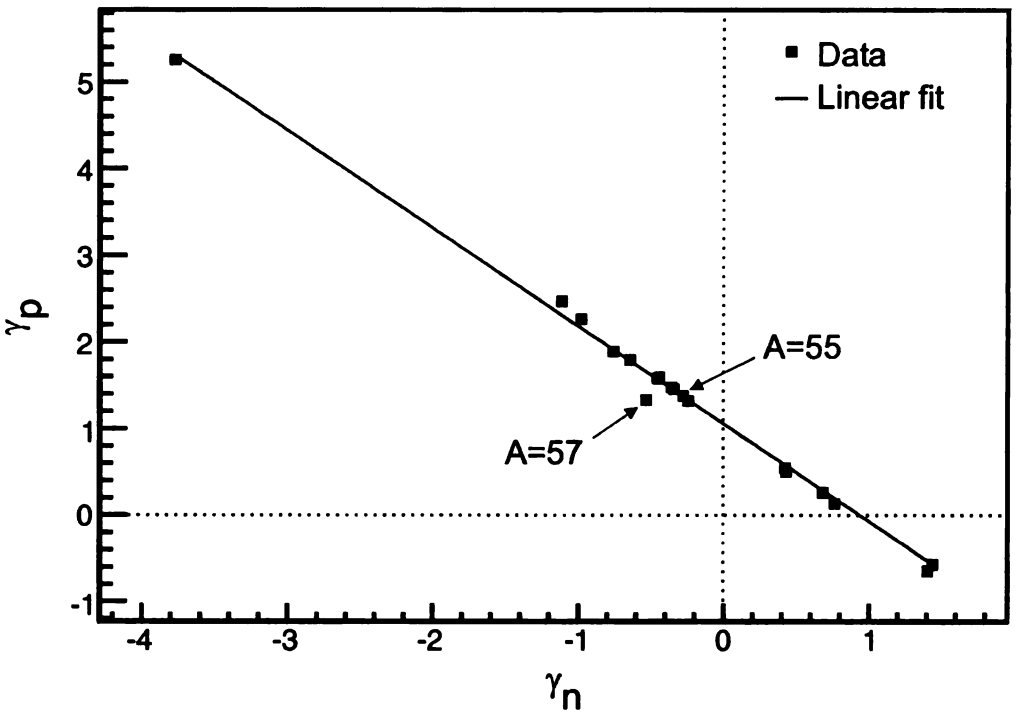

Figure 5.9: Nuclear g factors of mirror pairs plotted as the odd proton nucleus g factor γ_p versus the odd neutron nucleus g factor γ_n, also known as a Buck-Perez plot. The squares are the experimental data and the solid line is a linear fit to the data.

5.2.5 Buck-Perez analysis

The $\mu(^{55}\mathrm{Ni})$ result can also be compared to the predictions made by Buck and Perez *et al.* based on the systematic linear relationship between ground state g factors and the β-decay transition strengths of mirror nuclei [11–13], as introduced in section 1.3.2. The predicted values are $\mu(^{55}\mathrm{Ni})$=-0.872 $\pm$ 0.081 μ_N based on the dependence of ft values and $\mu(^{55}\mathrm{Ni})$=-0.945 $\pm$ 0.039 μ_N from the linear trend of experimental g factors. Both predictions agree with the observed $\mu(^{55}\mathrm{Ni})$=-0.976 $\pm$ 0.026 μ_N, although the predictions have large errors.

The experimental g factors of the $T = 1/2$ mirror nuclei, including the new $A = 55$ value, are shown in Fig. 5.9. A linear fit was performed and the new $A = 55$ value follows the linear trend well. The Buck-Perez extrapolation is a valid prediction for fp shell nuclei with unknown magnetic moments, an important tool for future measurements.

Chapter 6

Conclusions and Outlook

The magnetic moment of the $T = 1/2$ ^{55}Ni nucleus was measured for the first time with the β-NMR technique. The ^{55}Ni ions were produced at NSCL from a 160 MeV/nucleon ^{58}Ni beam impinging on a Be target. The resulting secondary beam was purified using both the A1900 and RF fragment separators. A three neutron removal reaction was employed, yielding a nuclear polarization of $|P| \sim 2\%$ at the peak of the momentum distribution. An NMR resonance was observed at 955 $\pm$ 25 kHz, with an external magnetic field of 0.4491 ± 0.0005 T. The deduced magnetic moment was $|\mu(^{55}\text{Ni})| = (0.976 \pm 0.026)\ \mu_N$. The experimental result agreed with shell model calculations with the GXPF1 interaction in the full *fp* shell. Results of the shell model calculation with free nucleon g factors showed reasonable agreement, while effective g factors obtained from an empirical fit to neighboring magnetic moments showed better agreement with experiment. The present μ supports the softness of the ^{56}Ni core.

The spin expectation value was extracted together with the known $\mu(^{55}\text{Co})$ as $\langle \sum \sigma_z \rangle = 0.91 \pm 0.07$. The shell model calculation with free g factors showed reasonable agreement with $\langle \sum \sigma_z \rangle$ while the effective g factors from the empirical fit did not. The effective g factors determined by isoscalar magnetic moments, isovector moments, and M1 decay matrix elements in the *sd* shell combined with $A = 55$ matrix

elements are able to explain the present $\langle \sum \sigma_z \rangle$. The agreement implies that a universal operator can be applied to both the *sd* and *fp* shells. However, for more detailed discussion, effective M1 operators of the *fp* shell nuclei have to be determined from the mirror moments in the *fp* shell, for which more experimental data are needed.

Continued studies of magnetic moments of nuclei immediately outside of presumed doubly-magic cores are important in the ongoing investigation of the resilience of the magic numbers away from stability. Moving further from stability comes at a cost of both spin polarization and yield, and for the β-NMR technique the figure of merit is P^2Y. The magnitude of spin polarization is expected to decrease as more nucleons are removed and/or picked up. In addition, the cross sections become lower for the most exotic nuclei. Greater magnitudes of spin polarization and greater yields are necessary to optimize the figure of merit P^2Y for β-NMR measurements on nuclei far from stability. A laser polarization beam line is currently being implemented at NSCL to provide polarized beams by optical pumping. Typically, the magnitude of spin polarization achieved via optical pumping is much greater than that obtained from fragmentation reactions.

With the new $\mu(^{55}\mathrm{Ni})$ result, $^{57}\mathrm{Cu}$ remains the only nucleus $\pm$ 1 nucleon away from $^{56}\mathrm{Ni}$ with a magnetic moment that does not agree with shell model. This leads to the question of whether the proton outside the $1f_{7/2}$ orbit is in some way affecting the core. The magnetic moments of the $T = 1/2$ nuclei $^{45}_{23}\mathrm{V}_{22}$, $^{47}_{24}\mathrm{Cr}_{23}$, $^{49}_{25}\mathrm{Mn}_{24}$, $^{51}_{26}\mathrm{Fe}_{25}$, and $^{53}_{27}\mathrm{Co}_{26}$ are important measurements that would provide insight on the $Z = 28$ shell closure. The magnetic moments of the mirror partners of $^{45}\mathrm{V}$, $^{49}\mathrm{Mn}$, and $^{51}\mathrm{Fe}$ are known ($^{45}\mathrm{Ti}$, $^{49}\mathrm{Cr}$, and $^{51}\mathrm{Mn}$, respectively). Completion of the mirror pair would allow the spin expectation value for the $A = 45, 49$ and 51 systems to be extracted, and would provide important information on shell evolution in the *fp* shell. These nuclei are difficult to produce at ISOL facilities, due to the chemistry involved in the extraction. Production of these polarized nuclei via optical pumping at NSCL may provide an avenue to access these difficult transition metals.

Finally, in this dissertation the systematics of only the isospin $T = 1/2$ mirror nuclei have been discussed. However, there have only been five $T = 3/2$ mirror pairs measured in the *sd* shell and none in the *fp* shell, and systematics have yet to be established. The magnetic moment of the heaviest bound $T_z = -3/2$ *fp* shell nucleus ^{55}Cu is another important measurement that not only would contribute to the $T = 3/2$ systematics, but would also provide important information on the $Z = 28$ shell closure, as ^{55}Cu is one proton above the $1f_{7/2}$ orbit. The magnetic moments of the Cu isotopes heavier than ^{57}Cu all agree with shell model. It is therefore necessary to go further from stability within the Cu isotopic chain and determine whether the $Z = 28$ shell closure is broken.

Appendix A

β-decay Asymmetry Parameter Calculation

The β-decay asymmetry parameter, A_β is given in Ref. [42] by:

$$A_\beta = \frac{\pm|C_A\langle\sigma\rangle|^2\lambda - 2C_A C_V\langle 1\rangle\langle\sigma\rangle\sqrt{J/(J+1)}\delta_{JJ'}}{|C_V\langle 1\rangle|^2 + |C_A\langle\sigma\rangle|^2} \tag{A.1}$$

where C_V and C_A are the vector and axial-vector coupling constants, $\langle 1\rangle$ is the Fermi matrix element, and $\langle\sigma\rangle$ is the Gamow-Teller matrix element. The $\pm$ refers to $\beta^\pm$ decay, $\delta_{JJ'}$ is the Kronecker delta, and λ is defined by

$$\lambda = \begin{cases} 1 & \text{for } J \to J' = J-1 \\ 1/(J+1) & \text{for } J \to J' = J \\ -J/(J+1) & \text{for } J \to J' = J+1. \end{cases} \tag{A.2}$$

To simplify the expression A.1, the mixing ratio is defined as:

$$\rho = \frac{C_A\langle\sigma\rangle}{C_V\langle 1\rangle}, \tag{A.3}$$

and A.1 simplifies to

$$A_\beta = \frac{\pm\rho^2\lambda - 2\rho\sqrt{J/(J+1)}\delta_{JJ'}}{1+\rho^2}. \tag{A.4}$$

^{55}Ni β^+ decays to ^{55}Co ($7/2^- \rightarrow 7/2^-$). Therefore, $\lambda = 1/(J+1) = 2/9$ and for $T = 1/2$ mirror β decays $\langle 1 \rangle$=1. The world average for the ratio of coupling constants C_A/C_V has been experimentally determined to be -1.2699 ± 0.0029 [73] from the β-asymmetry parameter of the free neutron. ρ then reduces to

$$\rho = -1.2699(29)\langle\sigma\rangle. \tag{A.5}$$

The absolute value of the Gamow-Teller matrix element, $|\langle\sigma\rangle|$ has been experimentally determined for ^{55}Ni as shown in Table A.1.

Table A.1: Experimentally determined values for the Gamow-Teller matrix element $|\langle\sigma\rangle|$.

	B(GT)	$\lvert\langle\sigma\rangle\rvert$
Reusen *et al.* [74]	0.466 ± 0.027	0.538 ± 0.031^a
Äystö *et al.* [58]		0.508 ± 0.008
Hornshøk *et al.* [75]		0.613 ± 0.017
Weighted mean		0.528 ± 0.007

[a]Extracted from $B(GT) = (C_A/C_V)^2\langle\sigma\rangle^2$.

From Eq. A.5,

$$\rho = \pm 0.671(9). \tag{A.6}$$

Note that the sign of ρ is determined by the sign of $\langle\sigma\rangle$, which is not known. The sign of ρ has been determined for *sd* shell $T = 1/2$ mirror β decays based on systematics in that shell. In the *fp* shell, only four mirror $T = 1/2$ β decays have been studied, including the $A = 55$ pair, and such systematics are not established.

Solving Eq. A.4 for both positive and negative ρ,

$$\begin{aligned} A_\beta &= \frac{(2/9)\rho^2 - 2\sqrt{7/9}\rho}{1+\rho^2} \\ &= \frac{(2/9)(\pm 0.671)^2 - 2\sqrt{7/9}(\pm 0.671)}{1+(\pm 0.671)^2} \\ &= -0.747 \pm 0.003 \text{ for } +\rho \qquad \text{(A.7)} \\ &= +0.885 \pm 0.005 \text{ for } -\rho. \qquad \text{(A.8)} \end{aligned}$$

Bibliography

[1] D.J. Griffiths. *Introduction to Electrodynamics (third edition)*, Prentice Hall, Inc., New Jersey, 1999.

[2] C.A. Baker, D.D. Doyle, P. Geltenbort, K. Green, M.G.D. van der Grinten, P.G. Harris, P. Iaydjiev, S.N. Ivanov, D.J.R. May, J.M. Pendlebury, J.D. Richardson, D. Shiers, and K.F. Smith. *Phys. Rev. Lett.*, **97**:131801, 2006.

[3] W. Loveland, D.J. Morrissey, and G.T. Seaborg. *Modern Nuclear Chemistry*, John Wiley & Sons, Inc., 2006.

[4] M. Honma, T. Otsuka, B.A. Brown, and T. Mizusaki. *Phys. Rev. C*, **69**:034335, 2004.

[5] B. Castel and I.S. Towner. *Modern Theories of Nuclear Moments*, Clarendon Press, Oxford, 1990.

[6] I.S. Towner. *Phys. Rep.*, **155**:263, 1987.

[7] V.V. Golovko, I. Kraev, T. Phalet, N. Severijns, B. Delauré, M. Beck, V. Kozlov, A. Lindroth, S. Versyck, D. Zákoucký, D. Vénos, D. Srnka, M. Honusek, P. Herzog, C. Tramm, U. Köster, and I.S. Towner. *Phys. Rev. C*, **70**:014312, 2004.

[8] B.A. Brown and B.H. Wildenthal. *Ann. Rev. Nucl. Part. Sci.*, **38**:29, 1988.

[9] K. Sugimoto. *Phys. Rev.*, **182**:1051, 1969.

[10] S.S. Hanna and J.W. Hugg. *Hyp. Int.*, **21**:59, 1985.

[11] B. Buck and S.M. Perez. *Phys. Rev. Lett.*, **50**:1975, 1983.

[12] B. Buck, A.C. Merchant, and S.M. Perez. *Phys. Rev. C*, **63**:037301, 2001.

[13] S.M. Perez, W.A. Richter, B.A. Brown, and M. Horoi. *Phys. Rev. C*, **77**:064311, 2008.

[14] H. Sakurai, S.M. Lukyanov, M. Notani, N. Aoi, D. Beaumel, N. Fukuda, M. Hirai, E. Ideguchi, N. Imai, M. Ishihara, H. Iwasaki, T. Kubo, K. Kusaka, H. Kumagai, T. Nakamura, H. Ogawa, Yu. E. Penionzhkevich, T. Teranishi, Y.X. Watanabe, K. Yoneda, and A. Yoshida. *Phys. Lett. B*, **448**:180, 1999.

[15] M. Tanigaki, M. Matsui, M. Mihara, M. Mori, M. Tanaka, T. Yanagisawa, T. Ohtsubo, T. Izumikawa, A. Kitagawa, M. Fukuda, K. Matsuta, Y. Nojiri, and T. Minamisono. *Hyp. Interact.*, **78**:105, 1993.

[16] J.D. Baldeschwieler. *J. Chem. Phys.*, **36**:152, 1962.

[17] F. Alder and F.C. Yu. *Phys. Rev.*, **81**:1067, 1951.

[18] T. Minamisono, T. Ohtsubo, S. Fukuda, Y. Nakayama, T. Araki, K. Masitani, K. Matsuda, E. Takahashi, M. Tanigaki, M. Tanaka, H. Shiohara, Y. Someda, Y. Aoki, A. Kitagawa, M. Fukuda, K. Matsuta, and Y. Nojiri. *Hyp. Interact.*, **78**:111, 1993.

[19] T. Minamisono, J.W. Hugg, D.G. Mavis, T.K. Saylor, H.F. Glavish, and S.S. Hanna. *Phys. Lett. B*, **61**:155, 1976.

[20] P. Kusch, S. Millman, and I.I. Rabi. *Phys. Rev.*, **55**:1176, 1939.

[21] E. Brun, J.J. Kraushaar, W.L. Pierce, and Wm.J. Veigele. *Phys. Rev. Lett.*, **9**:166, 1962.

[22] T. Minamisono, Y. Nojiri, K. Matsuta, K. Takeyama, A. Kitagawa, T. Ohtsubo, A. Ozawa, and M. Izumi. *Nucl. Phys. A*, **516**:365, 1990.

[23] K. Minamisono, P.F. Mantica, T.J. Mertzimekis, A.D. Davies, M. Hass, J. Pereira, J.S. Pinter, W.F. Rogers, J.B. Stoker, B.E. Tomlin, and R.R. Weerasiri. *Phys. Rev. Lett.*, **96**:102501, 2006.

[24] T. Ohtsubo, D.J. Cho, Y.Yanagihashi, S. Ohya, and S. Muto. *Phys. Rev. C*, **54**:554, 1996.

[25] P.T. Callaghan, M. Kaplan, and N.J. Stone. *Nucl. Phys. A*, **201**:561, 1973.

[26] N. Schulz, J. Chevallier, B. Haas, J. Richert, and M. Toulemonde. *Phys. Rev. C*, **8**:1779, 1975.

[27] G. Kraus, P. Egelhof, C. Fischer, H. Geissel, A. Himmler, F. Nickel, G. Münzenberg, W. Schwab, A. Weiss, J. Friese, A. Gillitzer, H.J. Körner, M. Peter, W.F. Henning, J.P. Schiffer, J.V. Kratz, L. Chulkov, M. Golovkov, A. Ogloblin, and B.A. Brown. *Phys. Rev. Lett.*, **73**:1773, 1994.

[28] Y. Yanagisawa, T. Motobayashi, S. Shimoura, Y. Ando, H. Fujiwara, I. Hisanaga, H. Iwasaki, Y. Iwata, H. Murakami, T. Minemura, T. Nakamura, T. Nishio, M. Notani, H. Sakurai, S. Takeuchi, T. Teranishi, Y.X. Watanabe, and M. Ishihara in *ENAM 98, Exotic Nuclei and Atomic Masses*, edited by Bradley M. Sherrill, David J. Morrissey, and Cary N. Davids, AIP Conf. Proc. No. 455 (AIP, Woodbury, NY, 1998), p. 610.

[29] K.L. Yurkewicz, D. Bazin, B.A. Brown, C.M. Campbell, J.A. Church, D.C. Dinca, A. Gade, T. Glasmacher, M. Honma, T. Mizusaki, W.F. Mueller, H. Olliver, T. Otsuka, L.A. Riley, and J.R. Terry. *Phys. Rev. C*, **70**:054319, 2004.

[30] S. Raman, C.W. Nestor, Jr., and P. Tikkanen. *At. Data Nucl. Data Tables*, **78**:1, 2001.

[31] T. Otsuka, M. Honma, and T. Mizusaki. *Phys. Rev. Lett.*, **81**:1588, 1998.

[32] N.J. Stone, U. Köster, J. Rikovska Stone, D.V. Fedorov, V.N. Fedoseyev, K.T. Flanagan, M. Hass, and S. Lakshmi. *Phys. Rev. C*, **77**:067302, 2008.

[33] E.M. Purcell, H. Torrey, and R.V. Pound. *Phys. Rev.*, **69**:37, 1946.

[34] K. Alder and A. Winther. *Electromagnetic excitation*, North-Holland, Amsterdam, 1975.

[35] G. Bollen, D. Davies, M. Facina, J. Huikari, E. Kwan, P.A. Lofy, D.J. Morrissey, A. Prinke, R. Ringle, J. Savory, P. Schury, S. Schwarz, C. Sumithrarachchi, T. Sun, and L. Weissman. *Phys. Rev. Lett.*, **96**:152501, 2006.

[36] K. Asahi, M. Ishihara, N. Inabe, T. Ichihara, T. Kubo, M. Adachi, H. Takanashi, M. Kouguchi, M. Fukuda, D. Mikolas, D.J. Morrissey, D. Beaumel, T. Shimoda, H. Miyatake, and N. Takahashi. *Phys. Lett. B*, **251**:488, 1990.

[37] H. Okuno, K. Asahi, H. Sato, H. Ueno, J. Kura, M. Adachi, T. Nakamura, T. Kubo, N. Inabe, A. Yoshida, T. Ichihara, Y. Kobayashi, Y. Ohkubo, M. Iwamoto, F. Ambe, T. Shimoda, H. Miyatake, N. Takahashi, J. Nakamura, D. Beaumel, D.J. Morrissey, W.D. Schmidt-Ott, and M. Ishihara. *Phys. Lett. B*, **335**:29, 1994.

[38] D.E. Groh, P.F. Mantica, A.E. Stuchbery, A. Stolz, T.J. Mertzimekis, W.F. Rogers, A.D. Davies, S.N. Liddick, and B.E. Tomlin. *Phys. Rev. Lett.*, **90**:202502, 2003.

[39] G.A. Souliotis, D.J. Morrissey, N.A. Orr, B.M. Sherrill, and J.A. Winger. *Phys. Rev. C*, **46**:1383, 1992.

[40] K. Turzó, P. Himpe, D.L. Balabanski, G. Bélier, D. Borremans, J.M. Daugas, G. Georgiev, F. de Oliveira Santos, S. Mallion, I. Matea, G. Neyens, Yu. E. Penionzhkevich, Ch. Stodel, N. Vermeulen, and D. Yordanov. *Phys. Rev. C*, **73**:044313, 2006.

[41] D.E. Groh, J.S. Pinter, P.F. Mantica, T.J. Mertzimekis, A.E. Stuchbery, and D.T. Khoa. *Phys. Rev. C*, **76**:054608, 2007.

[42] M. Morita. *Beta decay and muon capture*, Benjamin, Massachusetts, 1973.

[43] R.J. Blin-Stoyle. *Fundamental Interactions and the Nucleus*, North-Holland/American Elsevier, 1973.

[44] D.W. Anthony, P.F. Mantica, D.J. Morrissey, and G. Georgiev. *Hyperfine Interact.*, **127**:485, 2000.

[45] P.F. Mantica, R.W. Ibbotson, D.W. Anthony, M. Fauerbach, D.J. Morrissey, C.F. Powell, J. Rikovska, M. Steiner, N.J. Stone, and W.B. Walters. *Phys. Rev. C*, **55**:2501, 1997.

[46] J. Korringa. *Physica*, **16**:601, 1950.

[47] W.D. Knight. *Phys. Rev.*, **76**:1259, 1949.

[48] P. Herzog, U. Dämmrich, K. Freitag, B. Prillwitz, J. Prinz, and K. Schlösser. *Nucl. Instr. and Meth. B*, **26**:471, 1987.

[49] A. Abragam, *The Principles of Nuclear Magnetism*, part of *The International Series of Monographs on Physics*, Oxford University Press, 1961.

[50] D.J. Morrissey, B.M. Sherrill, M. Steiner, A. Stolz, and I. Wiedenhoever. *Nucl. Instr. and Meth. B*, **204**:90, 2003.

[51] D. Gorelov, V. Andreev, D. Bazin, M. Doleans, T. Grimm, F. Marti, J. Vincent, and X. Wu. In *Proceedings of 2005 Particle Accelerator Conference, Knoxville, Tennessee.* IEEE Publishing, 2005.

[52] P.F. Mantica, D.W. Anthony, M. Huhta, J.I. Prisciandaro, and M.A. Vance. *Nucl. Instr. and Meth. A*, **422**:498, 1999.

[53] D. Bazin, O. Tarasov, M. Lewitowicz, O. Sorlin. *Nucl. Instr. and Meth. A*, **482**:307, 2002.

[54] K. Minamisono, R.R. Weerasiri, H.L. Crawford, P.F. Mantica, K. Matsuta, T. Minamisono, J.S. Pinter, and J.B. Stoker. *Nucl. Instr. and Meth. A*, **589**:185, 2008.

[55] http://www.tcl.tk

[56] R. Fox. http://www.tcl.tk/community/tcl2006/abstracts/thu-am1-3.html

[57] Glenn F. Knoll, *Radiation Detection and Measurement, third edition*, John Wiley & Sons, 2000.

[58] J. Äystö, J. Ärje, V. Koponen, P. Taskinen, H. Hyvönen, A. Hautojärvi, and K. Vierinen. *Phys. Lett. B*, **138**:369, 1984.

[59] D.E. Groh. *Ph.D. Thesis*, Michigan State University, 2002.

[60] A.S. Goldhaber. *Phys. Lett. B*, **53**:306, 1974.

[61] R.K. Tripathi and L.W. Townsend. *Phys. Rev. C*, **49**:2237, 1994.

[62] H. DeVries, C.W. DeJager, and C. DeVries. *At. Data Nucl. Data Tables*, **36**:495, 1987.

[63] L.D. Landau and E.M. Lifshitz. *Mechanics, by L.D. Landau and E.M. Lifshitz. Translated from Russian by J.B. Sykes and J.S. Bell.* Oxford, New York, Pergamon Press, 3rd ed, 1976.

[64] K.S. Krane. *Introductory Nuclear Physics*, John Wiley & Sons, Inc., 1988.

[65] D.T. Khoa, G.R. Satchler, and W. von Oertzen. *Phys. Rev. C*, **56**:954, 1997.

[66] J. Gosset, H.H. Gutbrod, W.G. Meyer, A.M. Poskanzer, A. Sandoval, R. Stock, and G.D. Westfall. *Phys. Rev. C*, **16**:629, 1977.

[67] K. Van Bibber, D.L. Hendrie, D.K. Scott, H.H. Weiman, L.S. Schroeder, J.V. Geaga, S.A. Cessin, R. Treuhaft, Y.J. Grossiord, J.O. Rasmussen, and C.Y. Wong. *Phys. Rev. Lett.*, **43**:840, 1979.

[68] E.J. Moniz, I. Sick, R.R. Whitney, J.R. Ficenec, R.D. Kephart, and W.P. Trower. *Phys. Rev. Lett*, **26**:445, 1971.

[69] D.M. Brink. *Phys. Lett. B*, **40**:37, 1972.

[70] B.A. Brown and B.H. Wildenthal. *Phys. Rev. C*, **28**:2397, 1983.

[71] B.A. Brown and B.H. Wildenthal. *Nucl. Phys. A*, **474**:290, 1987.

[72] A. Arima, K. Shimizu, W. Bentz, and H. Hyuga, *Adv. Nucl. Phys.*, **18**:1, 1987.

[73] Hartmut Abele. *Nucl. Instr. and Meth. A*, **440**:499, 2000.

[74] I. Reusen, A. Andreyev, J. Andrzejewski, N. Bijnens, S. Franchoo, M. Huyse, Yu. Kudryavtsev, K. Kruglov, W.F. Mueller, A. Piechaczek, R. Raabe, K. Rykaczewski, J. Szerypo, P. Van Duppen, L. Vermeeren, J. Wauters, and A. Wöhr. *Phys. Rev. C*, **59**:2416, 1999.

[75] P. Hornshøj, L. Højsholt-Poulsen, and R. Rud. *Nucl. Phys. A*, **288**:429, 1977.